

**SYNTHESIS AND BIOMECHANICAL  
STUDIES OF NANO BIO CERAMIC  
REINFORCED HYDROGEL COMPOSITES  
FOR CARTILAGE TISSUE IMPLANTS**

Thesis

Submitted in partial fulfilment of the requirements for the degree of

**DOCTOR OF PHILOSOPHY**

by

**SANTOSH KUMAR B.Y.**



DEPARTMENT OF MECHANICAL ENGINEERING  
NATIONAL INSTITUTE OF TECHNOLOGY KARNATAKA,  
SURATHKAL, MANGALORE – 575025, INDIA.

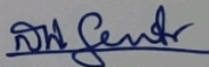
JULY, 2021

## DECLARATION

I hereby *declare* that the Research Thesis entitled “**Synthesis and Biomechanical Studies of Nano Bioceramic Reinforced Hydrogel Composites For Cartilage Tissue Implants**” is being submitted to the **National Institute of Technology Karnataka, Surathkal** in partial fulfilment of the requirements for the award of the Degree of **Doctor of Philosophy** in **Department of Mechanical Engineering** is a *bonafide report of the research work carried out by me*. The material contained in this Research Thesis has not been submitted to any University or Institution for the award of any degree.

Register Number : 165060ME16F17

Name of the Research Scholar : SANTOSH KUMAR B. Y

Signature of the Research Scholar : 

Department of Mechanical Engineering

Place: NITK-Surathkal

Date: 18-11-2021

## CERTIFICATE

This is to *certify* that the Research Thesis entitled “**SYNTHESIS AND BIOMECHANICAL STUDIES OF NANO BIOCERAMIC REINFORCED HYDROGEL COMPOSITES FOR CARTILAGE TISSUE IMPLANTS**” submitted by **Mr. SANTOSH KUMAR B.Y.** (Register Number: 165060ME16F17) as the record of the research work carried out by him, is *accepted as the Research Thesis submission* in partial fulfilment of the requirements for the award of the degree of **Doctor of Philosophy.**

### Research Guide

*Mohan Kumar*  
18.11.2021

**Dr. G. C. Mohan Kumar**

Professor

Department of Mechanical Engineering

NITK, Surathkal

*G. C. Mohan Kumar*

Chairman-DRPC

Date: 18 NOV 2021



## ACKNOWLEDGEMENTS

With a deep sense of gratitude, I wish to express my sincere thanks to my supervisors **Prof. G. C. Mohan Kumar**, Department of Mechanical Engineering, National Institute of Technology Karnataka (N.I.T.K.), Surathkal, for their excellent guidance and support throughout the work. I received very useful, encouraging and excellent academic feedback from them, which has stood in good stead while writing this thesis. Their constant encouragement, help and review of the entire work during the course of the investigation were invaluable. I profoundly thank them.

I am also grateful to my Research Progress Assessment Committee (RPAC) members **Dr. Mrityunjaya R. Doddamani**, Assistant Professor, Department of Mechanical Engineering, and **Dr. Raviraj H. M.**, Assistant Professor, Department of Civil Engineering, National Institute of Technology Karnataka, Surathkal for their insightful suggestions, advice and patience.

I take this opportunity to thank **Dr. S.M. Kulkarni**, Professor and Head, Department of Mechanical Engineering, NITK for his continuous and timely suggestions.

I sincerely thanks **Dr. Arun M. Isloor**, Professor and Head, Department of Chemistry, NITK, **Dr. Venkatesan Jayachandran**, Assistant Professor, Yenepoya Research Centre, Yenepoya University, Mangaluru and **Dr. Ananda Kulal**, Associate Professor, Poornaprajna Institute of Scientific Research, Bengaluru for their support and encouragement in carrying out research activities.

A special thanks to my family, friends and relatives who supported me and incited me to strive towards my goal.

I wish to express my sincere gratitude to all the faculty members of the Department of Mechanical Engineering, N.I.T.K Surathkal for their help, encouragement and support all through this research work.

**(Santosh Kumar B.Y)**

## ABSTRACT

Cartilage damage is persistent and disease, which is having a great shock on people's daily activity. Thus, repair or replacement has become an effective way to relieve pain. The technological advancement in biomaterials is not enough to overcome the challenges to develop a new material to replace defected Articular Cartilage (AC). The designed material is to fulfil the physical and mechanobiological properties of soft tissue. Hydrogels have drawn much attention as implant biomaterial due to their similarity with native articular cartilage. However, the discrepancy in mechanical properties, durability together with inadequacy to integrate with the surrounding tissue hinder the clinical application. Here, we reported the utilisation of bioceramics as a reinforcement to prepare a novel natural and synthetic polymer composite hydrogel by a physical crosslinking process. The reinforcement content was optimised and it was found that the introduction of bioceramic alters the physical, mechanical and biological properties by cumulative crosslinking in the hydrogel network. More significantly, the introduction of bioceramics in the hydrogel increases the compression strength and they exhibit time-dependent, rapid self-recoverable and fatigue resistant behaviour based on the cyclic loading-unloading compression test. The storage modulus is much higher than the loss modulus, demonstrates they are elastic dominant rather than fluid-like structure. Besides, the antimicrobial activity against *Escherichia coli*, *Staphylococcus aureus* and *Candida albicans* microbes and the cell viability towards MG-63 osteoblast and L929 fibroblast-like cells provide a positive lane for developing the substitute biomaterial for cartilage tissue implants.

**Keywords:** *Bioceramics, Chitosan, Polyvinyl alcohol, Hydrogel, Cartilage*

## TABLE OF CONTENTS

Declaration	i
Certificate	ii
Acknowledgements	iii
Abstract	iv
Table of contents	v
List of figures	ix
List of tables	xiii
Abbreviations	xiv
<b>1. CHAPTER 1 INTRODUCTION</b>	<b>1</b>
1.1 Overview of Biomaterials	1
1.2 Global biomaterial revolution	2
1.3 Hydrogels in Tissue engineering	5
1.4 Classification of hydrogels	7
1.5 Hydrogels for cartilage tissue engineering	8
1.5.1 Structure and function of human articular cartilage	8
1.5.2 Cartilage Damage and Traditional repair	10
1.5.3 Advances in Articular Cartilage Repair with Hydrogel	11
1.6 Hypothesis	12
1.7 Objectives of the research work	12
1.8 Thesis Structure	13
<b>2. CHAPTER 2 LITERATURE REVIEW</b>	<b>15</b>
2.1 The literature on Natural Polymers	21
2.1.1 Chitosan	21
2.1.2 Gelatin	23
2.1.3 Cellulose	24
2.1.4 Alginate	26
2.2 The literature on Synthetic hydrogels	28
2.2.1 Polyvinyl alcohol	28
2.2.2 Poly (ethylene glycol)	30
2.2.3 Poly (hydroxyethyl methacrylate)	31

2.2.4 Polyacrylamide	32
2.2.5 Poly (lactic acid) and poly (glycolic acid)	32
2.2.6 The literature on hydroxyapatite and calcium phosphate	33
2.2.7 Hydroxyapatite from biowaste cuttlefish bone	34
2.2.8 Hydroxyapatite synthesis from chemical method	35
<b>3. CHAPTER 3 MATERIALS AND METHODS</b>	<b>37</b>
3.1 Materials used for composites	37
3.2 Synthesis of hydroxyapatite and tricalcium phosphate	37
3.3 Characterization of hydroxyapatite	38
3.4 Characterization of Tricalcium phosphate	42
3.5 Developing of Titanium Dioxide Nanotube	44
<b>4. CHAPTER 4 INFLUENCE OF BIOCERAMICS ON CHITOSAN COMPOSITE HYDROGEL FOR CARTILAGE REGENERATION</b>	<b>47</b>
4.1 Materials used for composites	47
4.2 Preparation of CS/HANr, CS/BCP and CS/TNT composite Hydrogel	47
4.3 Characterization of composite hydrogel	48
4.3.1 Physical tests	49
4.3.2 Mechanical tests	49
4.3.3 Rheological Test	50
4.4 Biological Characterization	50
4.4.1 Degradation studies	50
4.4.2 Growth inhibition test	51
4.4.3 Measurement of cytotoxicity	51
4.4.4 Statistics	51
4.5 Results and Discussion	51
4.5.1 Compression & cyclic loading-unloading compression test	55
4.5.2 Rheological Studies	59
4.5.3 Biological studies	61
4.5.3.1 Antimicrobial properties	61

4.5.3.2 Cytotoxicity assay	65
<b>5. CHAPTER 5 EFFECT OF BIOCERAMICS ON POLYVINYL ALCOHOL HYDROGEL FOR CARTILAGE TISSUE IMPLANTS</b>	<b>71</b>
5.1 Materials used for composites	71
5.2 Development of PVA/HANr, PVA/BCP and PVA/TNT composite hydrogel	71
5.3 Characterization of PVA and its composite hydrogel	72
5.3.1 Physical characterisation	72
5.3.2 Mechanical test	73
5.3.3 Rheological Test	73
5.3.4 Measurement of coefficient of friction	74
5.3.5 Degradation studies	74
5.3.6 Growth inhibition test	74
5.3.7 Measurement of cytotoxicity	74
5.4 Statistics	74
5.5 Results and Discussion	75
5.5.1 Morphology and IR analysis	76
5.5.2 Swelling and contact angle measurements	78
5.5.3 Mechanical characterization	79
5.5.4 Rheological behavior of PVA and its composite hydrogel	83
5.5.5 Friction test	84
5.5.6 Measurement of antimicrobial properties	85
5.5.7 Measurement of cytotoxicity	86
<b>6. CHAPTER 6 DEVELOPMENT OF HYDROXYAPATITE SCAFFOLDS FOR BONE TISSUE ENGINEERING</b>	<b>89</b>
6.1 Scaffold preparation	90
6.2 Nanohydroxyapatite scaffold characterization	91
6.2.1 Morphological characterization	91
6.2.2 Physical and Mechanical characterization	91
6.2.3 Degradation studies	91



6.2.4 Microbial study	92
6.2.5 Growth inhibition test	92
6.2.6 Measurement of cytotoxicity	92
6.3 Results and Discussion	93
6.3.1 Biological characterization	97
<b>7. CONCLUSION AND SCOPE FOR THE FUTURE WORK</b>	<b>102</b>
7.1 Contribution to the research work	102
7.2 Conclusions	102
7.3 Scope for the future work	103
<b>REFERENCES</b>	<b>105</b>
<b>PUBLICATION DETAILS</b>	<b>114</b>

## LIST OF FIGURES

<b>Fig. No.</b>	<b>Description</b>	<b>Page no</b>
Fig. 1.1	(a) Wooden toe prosthetic designed from natural material and (b) The ancient Egyptian dentistry	2
Fig. 1.2	Evolution of biomaterial science and technology	3
Fig. 1.3	Schematic representation of the ionization process of the polymeric hydrogels	6
Fig. 1.4	Polymer chain with negative charge development	6
Fig. 1.5	Mechanism of hydrogen bond formation between the polymer and water molecule	7
Fig. 1.5	Zonal organisations of human articular cartilage from the superficial zone to the deep zone and the calcified cartilage	9
Fig. 1.7	Cartilage repair technics (a) Chondroplasty (b) Microfracture (c) Total knee replacement	11
Fig. 2.1	Chemical structure of chitosan	23
Fig. 2.2	Chemical structure of gelatin	24
Fig. 2.3	Chemical structure of cellulose	25
Fig. 2.4	Chemical structure of sodium alginate molecule	27
Fig. 2.5	The chemical reaction in the formation of PVA	28
Fig. 2.6	Chemical structure of PEG and its derivatives	30
Fig. 2.7	Chemical structure of Poly (hydroxyethyl methacrylate)	31
Fig. 2.8	Chemical structure of Hydroxyapatite	33
Fig. 2.9	Photograph of the cuttlefish bone	34
Fig. 3.1	Schematic representation hydroxyapatite synthesis	38
Fig. 3.2	X-ray Diffractogram of Synthesized Hydroxyapatite.	39
Fig. 3.3	FESEM images of hydroxyapatite with various magnification (a) 2 $\mu\text{m}$ , (b) 1 $\mu\text{m}$ , (c) 200 nm and (d) 100 nm.	41
Fig. 3.4	FT IR spectra of (a) Cuttlebone, (b) HAp and (c) $\beta$ -TCP	42
Fig. 3.5	XRD pattern of synthesized calcium phosphate	43
Fig. 3.6	SEM images of calcium phosphate	43

Fig. 3.7	Thermogravimetric analysis of (a) Cuttlebone, (b) Hydroxyapatite and (c) $\beta$ -Tricalcium phosphate	44
Fig. 3.8	TEM image of synthesised TNT	45
Fig. 4.1	Schematic representation of Chitosan composite hydrogel preparation	48
Fig. 4.2	Photographs of the hydrogel (a-b) Chitosan and (c) Chitosan composite hydrogel	52
Fig. 4.3	SEM images of hydrogel (a) CS (b) CS/1.5HANr (c) CS/3BCP and (d) CS/2TNT composite hydrogel	53
Fig. 4.4	Fourier Transform Infrared (ATR-FTIR) Spectroscopy of CS and its composite hydrogel	54
Fig. 4.5	Unconfined compression and cyclic loading-unloading compression test curves of (a-b) CS/1.5HANr (c-d) CS/3BCP and (e-f) CS/2TNT composite hydrogel	57
Fig. 4.6	The loading-unloading compression curves of (a) CS/1.5HANr, (b) CS/3BCP and (c) CS/2TNT composite hydrogel for 100 cycles	58
Fig. 4.7	Cyclic stress-strain curves of viscoelastic materials as a function of time	59
Fig. 4.8	Variation of storage and loss modulus of the composite hydrogel as a function of angular frequency	61
Fig. 4.9	Antibiogram of chitosan and its composite hydrogel	63
Fig. 4.10	Zone of inhibition of chitosan and chitosan hydrogel against <i>Escherichia coli</i> , <i>Staphylococcus aureus</i> and <i>Candida albicans</i> after 24 h of incubation.	64
Fig. 4.11	L929 and MG63 cell viability of on CS, CS/1.5HANr, CS/3BCP and CS/2TNT composite hydrogel after 72 h of incubation	67
Fig. 4.12	Inverted microscope images of L929 cell viability towards DMEM, PHA, CS, CS/1.5HANr, CS/3BCP and CS/2TNT after 72 h of incubation.	68

Fig. 4.13	Inverted microscope images of MG63 cell viability towards DMEM, PHA, CS, CS/1.5HANr, CS/3BCP and CS/2TNT after 72 h of incubation.	69
Fig. 5.1	Phenomenon of wettability of the solid surface	72
Fig. 5.2	Macroscopic images of (a) PVA and (b) PVA composite hydrogel	76
Fig. 5.3	Scanning electron microscope images of (a) PVA (b) PVA/2HANr (c) PVA/2.5BCP and (d) PVA/2TNT composite hydrogel	76
Fig. 5.4	FTIR of PVA, PVA/2HANr, PVA/2.5BCP and PVA/2TNT composite hydrogel	77
Fig. 5.5	Unconfined compression and cyclic loading-unloading compression test (a-b) PVA/HANr, (c-d) PVA/BCP and (e-f) PVA/TNT composite hydrogels	81
Fig. 5.6	The cyclic loading-unloading compression test of (100 cycles) (a) PVA/2HANr, (b) PVA/2.5BCP and (c) PVA/2TNT composite hydrogels	82
Fig. 5.7	The variation of storage and loss modulus of PVA and its composite hydrogel	83
Fig. 5.8	The friction coefficient of PVA and its composite hydrogel as a function of time	84
Fig. 5.9	Antibiogram of PVA and its composite hydrogel against Escherichia coli, Staphylococcus aureus and Candida albicans after 24 h of incubation	85
Fig. 5.10	L929 and MG63 cell viability of on PVA, PVA/2HANr, PVA/2.5BCP and PVA/2TNT composite hydrogel after 24, 48 and 72 h of incubation.	86
Fig. 5.11	Inverted microscope images of MG63 cell viability towards DMEM, PHA, PVA, PVA/2HANr, PVA/2.5BCP and PVA/2TNT after 72 h of incubation.	87

Fig. 5.12	Inverted microscope images of L929 cell viability towards DMEM, PHA, PVA, PVA/2HANr, PVA/2.5BCP and PVA/2TNT after 72 h of incubation.	88
Fig. 6.1	Flow chart for the preparation of hydroxyapatite scaffolds	90
Fig. 6.2	(a) Developed nHAp scaffolds (b) Fractured scaffold surface due to compression and (c) SEM image of the scaffolds shows the macro porous surface	93
Fig. 6.3	X-ray Diffractogram of nHAp scaffold	94
Fig. 6.4	FTIR spectrum of nHAp scaffold	95
Fig. 6.5	Molecular weight change (KDa) with in vitro degradation time of nHAp scaffold for 11-week observation at 37 °C	96
Fig. 6.6	Growth inhibition of gram-negative Escherichia coli, gram-positive Staphylococcus aureus and Candida albicans fungi after 6, 12 and 24 h of incubation	97
Fig. 6.7	L929 fibroblast and MG 63 osteoblast-like cell viability on nHAp scaffold after 72 h of incubation	98
Fig. 6.8	Inverted microscope images of L929 (left) and MG 63 (right) cell viability on DMEM, PHA and nHAp after 72 h of incubation	99

## LIST OF TABLES

<b>Table No</b>	<b>Description</b>	<b>Page no</b>
Table 1.1	Various biomaterials used in the human body	4
Table 1.2	Classification of hydrogels	7
Table 2.1	Natural and synthetic polymers, key benefits and their applications	16
Table 2.2	Nanoparticle reinforced composite hydrogels.	17
Table 3.1	Cell parameters of synthesised hydroxyapatite	40
Table 4.1	Physical properties of PVA/HANr hydrogel	55
Table 4.2	Compressive mechanical properties of CS composite hydrogel	56
Table 4.3	Inhibition area of microbial growth calculated around the samples through the disc diffusion test.	65
Table 5.1	Physical properties of PVA and its composite hydrogel	78
Table 5.2	Tensile mechanical properties of PVA nanocomposite hydrogel	80
Table 5.3	Compressive mechanical properties of PVA nanocomposite hydrogel	80
Table 6.1	Physico-mechanical properties of nHAp scaffolds	96

## ABBREVIATIONS

AC	Articular Cartilage
OA	Osteoarthritis
ACI	Autologous Chondrocyte Implantation
TKR	Total Knee Replacement
CS	Chitosan
PVA	Polyvinyl alcohol
HAp	Hydroxyapatite
BCP	Bi-phasic Calcium Phosphate
HANr	Hydroxyapatite Nanorod
TNT	Titanium Dioxide Nanotube
CAGR	compound annual growth rate
ASTM	American Society for Testing Materials
pHEMA	Polyhydroxyethylmethacrylate
PEG	Polyethylene glycol
FESEM	Field Emission Scanning Electron Microscope
ATR-	Attenuated Total Reflectance Fourier Transform Infrared
FTIR	Spectroscopy
JCPDS	Joint Committee on powder Diffraction Standards
XRD	X-ray Diffraction
TGA	Thermogravimetric Analysis
HCl	Hydrochloric acid
RPM	Revolution Per Minute
MPa	Mega Pascal
G'	Storage Modulus
G''	Loss Modulus
DMEM	Dulbecco's Modified Eagle Medium
CO <sub>2</sub>	Carbon Dioxide
OD	Optical Density
DMSO	Dimethylsulfoxide

# CHAPTER 1

## INTRODUCTION

---

### 1.1 Overview of Biomaterials

Biomaterials are used in medical devices since antiquity, but recently their degree of sophistication has increased significantly. Historically the selection of material was based on availability and ease of processing. In early days, a variety of natural material such as wood, nacre, ivory was used for the prosthesis (Huebsch and Mooney 2009). The first scaffolds have been reported in the Neolithic period i.e., 7000 B.C to 1000 B.C. As a teeth substitute, the antique dentist used different animal teeth, particularly dogs, calves, seals and narwhals. (Hildebrand 2013). In the early part of the twentieth century, these naturally derived materials were replaced by synthetic polymers, ceramics, metals and alloys, which provides better performance, functionality and reliability than their naturally derived counterparts.

The increase in demand for biomaterials over the past decades can be estimated in various ways including academic research. It was found that there has been a drastic rise in scientific publications in the field of biomaterials over the past 70 years. In India, there are more than 100 departments of biomedical engineering (less than ten existed before 1990) with more than 250,000 students enrolled for different courses. Among these courses, biomaterial engineering is a major field of study since it is directly linked with the other engineering departments. Besides, biomaterials are a critical component in various industries including medical devices, dental restoratives, drug delivery, and increasingly used technological applications such as *in vitro* diagnostics. Together, these applications generate a market of about \$228 billion per year with a registered growth rate of 10% from the last couple of years and it is expected to reach \$332 billion by 2022.

The medical device industry in India is currently valued at \$5.2 billion. It has about 780-800 medical device manufacturers in the country, with an average investment of 170-200 million and an average turnover of 450-500 million. The industry has steadily grown witnessed a surge from \$2.02 billion in 2009 to \$3.9 billion in 2015 at a compound annual growth rate (CAGR) of 15.8%. As per industry estimates, the Indian medical market will grow to \$50 billion by 2025. Currently, India is counted



among the top 20 global medical device markets and is the 4<sup>th</sup> largest medical device market in Asia after Japan, China, and South Korea (Pal et al. 2017b).

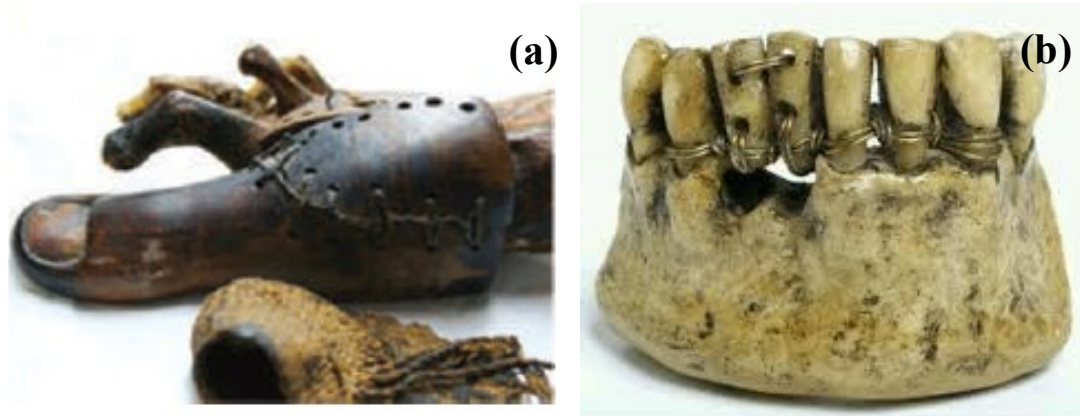


**Fig. 1.1** (a) Wooden toe prosthetic designed from natural material and (b) Ancient Egyptian Dentistry (Image courtesy of J. Finch, Center for Biomedical Egyptology, University of Manchester UK and The Egyptian Museum, Cairo).

## 1.2 Global biomaterial revolution

The biomaterial revolution initiates in the early part of the twentieth century considerably pretentious how biomaterials are designed and used. The first generation biomaterials were recognised more prominently during 1960-70. To achieve the required mechanical stiffness of biomaterial and match those with the replaced tissue with a minimal toxic response in the host, various metals such as stainless steel, cobalt and titanium were introduced. The success of these metallic biomaterials is due to their resistance to corrosion, passive oxide layer. However, the higher biocompatibility that makes the material inert within the body might not be enough to elicit growth and regeneration. Also, a mismatch in the stiffness of bone to the high stiffness of metals may lead to stress shielding or aseptic loosening (Tone et al. 2017).

To overcome those above issues, researchers started to develop second-generation materials which were more “biologically active” or “bioactive”. The mechanism of bonding of bioactive glasses (composed of  $\text{Na}_2\text{O}-\text{CaO}-\text{P}_2\text{O}_5-\text{SiO}_2$ ) to living tissue was established in 1971 (Hench et al. 1971). In 1980, there was a progression towards the development of bioactivity by varying surface roughness and porosity. The results revealed that surface roughness plays a crucial role in cell adhesion and proliferation whereas, porosity supports the diffusion of essential nutrients and removal of excretions in the biological environment. Another category is resorbable

biomaterials in which the scaffold-tissue interface was controlled by chemical breakdown i.e. resorption of the material. Resorption of biomaterial is the perfect solution to the interfacial problem because the foreign implant material is ultimately replaced by regenerating tissue so that there is no discrimination between implant site and host tissue. However, in many cases, the survivability analysis provides a bleak outcome largely on load-bearing scaffolds materials.

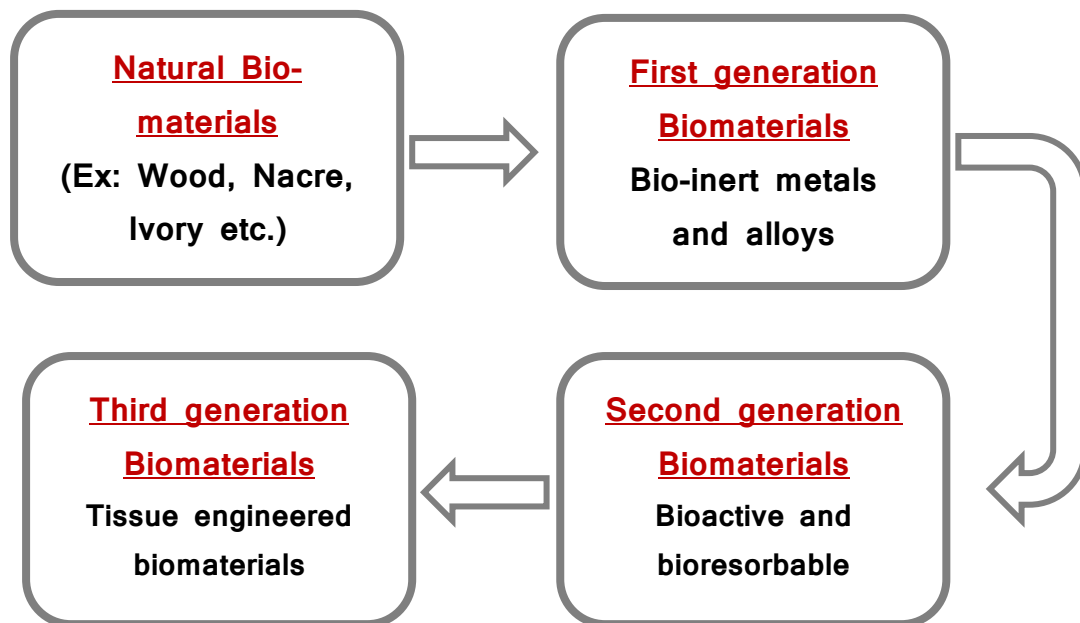


**Fig. 1.2** Evolution of biomaterial science and technology

The molecular biology revolution of the 1980s and advances in genomics and proteomics carries the usage of biomaterials to the next level. The specific biomolecules have been implicated with the clinical process (for example, bone morphogenetic protein in osteogenesis) and incorporated into specific biomaterial components. This combination interfaces directly with cells and tissues through a well-defined molecular pathway to biological responses as already represent the state of the art of commercial products such as drug-delivery, drug-eluting vascular stents, etc. Tissue engineering is concerned with the development of biological substitutes capable of replacing or regenerating diseased or damaged tissues. It was introduced in 1980 and early 1990 and the concept was applied to repair the biological tissue resulted in the rapid growth of tissue engineering. This is an interdisciplinary field with the potential to revolutionise important areas of biomedical engineering. This helps to minimise the critical gap between growing numbers of patients on the waiting list for organ transplantation.

**Table 1.1:** Various biomaterials used in the human body

<b>Skeletal system</b>	<b>Biomaterial used</b>
<b>Cranial repair</b>	Titanium, Poly-methyl-methacrylate, Acrylic and Calcium phosphate cement scaffold. (Kihlstrom Burenstam Linder et al. 2019; Lee et al. 2014; Unterhofer et al. 2017; Vaandrager et al. 1983)
<b>Ophthalmologic</b> Contact lens Intraocular lens Corneal bandage lens Glaucoma drain	Acrylate/methacrylate/Silicone polymers Acrylate/methacrylate Hydrogel Silicone/Polypropylene (Efron and Maldonado-Codina 2011)
<b>Maxillofacial reconstructions</b>	Acrylics/Silicone/Latex (Prasadh and Wong 2018)
<b>Dental implants</b>	Titanium and its alloys/Zirconium/Hydroxyapatite coatings (Koizumi et al. 2019)
<b>Alveolar (jaw) ridge augmentation</b>	Hydroxyapatite and Bioactive glasses (Frame 1987)
<b>Skeletal system</b> Joint replacement (hip, knee, shoulder)  Bone fixation plates and screws  Bone defect repair Artificial tendon and ligaments	Titanium, stainless steel, high-density polyethylene Magnesium alloys and Poly (lactic acid) (Li et al. 2019)  Calcium phosphate cement (Lin et al. 2019)  Silk and polyester fibers (Ma et al. 2018)
<b>Cardiovascular System</b> Heart Valve  Stent material	Polycaprolactone (Ibrahim et al. 2017)  Stainless steel, PLA (McMahon et al. 2018)
<b>Organs</b> Artificial breast Cartilage Artificial skin Artificial bone	Silicone Polyvinyl alcohol Silk fibroin Hydroxyapatite, Calcium phosphate (Li et al. 2019)

Tissue engineering integrates biological components such as cells, biomaterials and growth factors with engineering principles. It involves the seeding of cells on the scaffolds and then incubated in a medium containing growth factors which stimulate the cells to grow and divide. As cells spread across the scaffold, the substitute is formed and is implanted into the defected site, with the implanted scaffold eventually being either absorbed or dissolved.

With this, the term biomaterial is defined as *a substance that has been engineered to interact with the biological systems for a medical purpose- either a therapeutic (treat, augment, repair or replace a tissue function of a body) or diagnostic use*. Currently, they are classified as;

- Medical implants including heart valves, stents, artificial tendons, ligaments and dental fixtures.
- Methods to promote healing of human tissues- including sutures, clips, staples for wound closure and dissolvable dressing.
- Regenerated human tissues including the combination of scaffolds, cells and bioactive molecules.
- Molecular probes and nanoparticles that breakthrough biological barriers and aid in cancer imaging and therapy at the molecular level.
- Biosensors to detect the presence and amount of specific substances in the host and drug delivery systems that carry and/or apply drugs to a targeted cell/tissue.

### **1.3 Hydrogels in Tissue engineering**

Hydrogels are the class of hydrated polymeric materials that can absorb more than 90 wt. % of water similar to mammalian tissues. They exhibit moderate-to-high physical, chemical and mechanical properties in their swelling state depend on the base material, reinforcement and processing approach. Hydrogels are generally defined by their equilibrium degree of swelling since it regulates the elasticity and water holding potency. Another important property that determines the hydrogel strength is water-polymer interactive forces. Generally, the higher the hydrophilicity, the stronger will be the water polymer interactive forces.

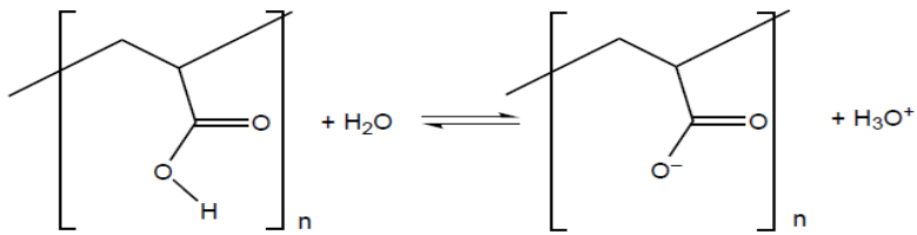


**Fig. 1.3** Schematic representation of the ionisation process of the polymeric hydrogels

The mechanism of water absorption in the hydrogel is due to the presence of ionic groups; osmosis is developed by the counter ions due to the difference in the ion concentration within the polymer and the solution. The higher the difference in the ion concentration is the larger the osmotic pressure. Based on the pendant ionic groups (negative or positive charge) in the polymer backbone hydrogels are defined as anionic or cationic respectively. These ionic charges in the polymer backbone start to repel each other and the polymer is forced to expand. Meanwhile, the polar water molecules are attracted towards the ionic charges and develop an electrostatic bonding between pendant groups and polar water molecules. Overall, three forces; polymer water interaction, electrostatic and osmotic expansion, decide the hydrogel's equilibrium swelling.

The hydrophilicity in polymeric hydrogels is influenced by many factors such as type of polymer network, nature of the solvent, processing technique and morphology. The crosslinking density determines the distance (molecular weight) between the two crosslinks on the same polymer chain. The shorter the distance, the higher the crosslinking.

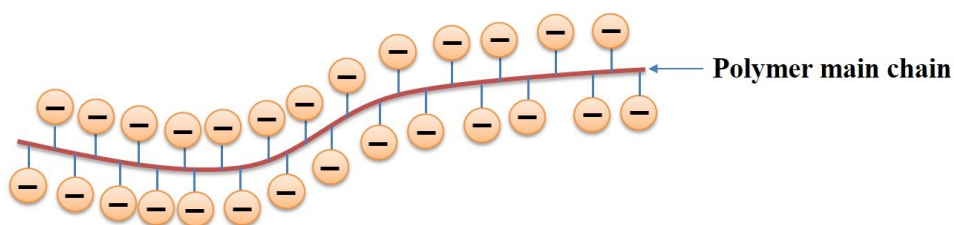


**Fig. 1.4** Polymer chain with negative charge development.

Hydrogels have been used since the 1960s for contact lens due to their hydrophilicity and oxygen permeability. However, the inflammatory response issues with some individuals curbs their application. With the continued research, now they

are employed in various fields such as biomaterial tissue scaffolds, agriculture and horticulture for water storage and water desalination.

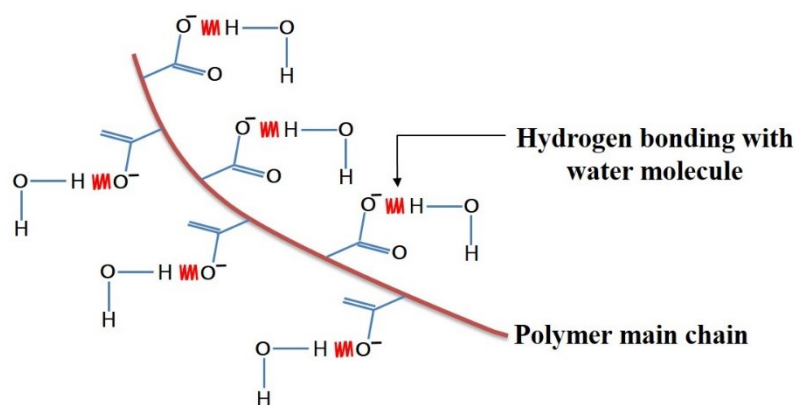


**Fig. 1.5** Mechanism of hydrogen bond formation between the polymer and water molecule

Due to structural and compositional similarity with the natural extracellular matrix, these materials can be easily engineered to control protein adsorption, cellular attachment, biodegradability and biocompatibility. The ideal implant/scaffold material will mimic the properties of the native extracellular matrix, will retain the adsorbed cells and biochemical factors, enable diffusion of nutrients and helps to remove the excretions in the biological environment. To develop such scaffolds, various types of polymers and processing technics, cross-linkers were used.

#### 1.4 Classification of hydrogels

Based on structure, presence of ions and synthesis method hydrogels are classified in various ways. Table 1.2 shows the classification of hydrogels based on various parameters.

**Table 1.2** Classification of hydrogels

Structure	Synthesis	Bonding	Size	Ionic charge
Amorphous	Homopolymer	Physical	Macro gel	Anionic
Semi-crystalline	Copolymer	Chemical	Micro gel	Cationic
Hydrocolloid	Multipolymer		Nanogel	Neutral
Hydrogen bond				Ampholitic

Based on the nature of blending, hydrogels are classified into homopolymer, copolymer and multipolymer. Homopolymeric hydrogels are synthesised from one hydrophilic monomer; copolymer hydrogels are comprised of two kinds of monomeric

units, and multipolymer hydrogels are prepared from three or more polymers. Based on the internal network structure, the hydrogels are classified as amorphous, semi-crystalline hydrogels with hydrogen bond structure, supermolecular and hydrocolloid aggregates.

Based on the ionic charges in a polymer chain, hydrogels are classified into anionic, cationic, neutral and ampholytic hydrogels. In anionic hydrogels typically contains negative ions attached to the polymer chain whereas, cationic hydrogels have fixed positive charges. However, in neutral hydrogels it is assumed that the solution contains an equal number of positive and negative charges.

Another type of classification of hydrogels is based on the type of bonding between the polymer chains. In physical hydrogels, the neighbouring polymer chains are entangled by weak Vander Wall force of attraction. Whereas in chemical gels, there is a permanent chemical bond that exists between the polymer chains through a covalent bond. The mesh size in the polymer network determines the mechanism of drug penetration in the hydrogel network. Based on the pore size of the hydrogel, they are classified as Macro, Micro and Nanogels. Microgels typically size in the range of a few millimetres to a centimetre. These hydrogels are usually used as a scaffold material. The nano and microgels have advantages over microgels. Their size is much smaller, and they have a higher surface area to volume ratio that provides more space for bioconjugation.

## **1.5 Hydrogels for cartilage tissue engineering**

### *1.5.1 Structure and function of human articular cartilage*

Cartilage is a resilient, smooth, poro-viscoelastic connective tissue covering and protecting the ends of long bones in the diarthrodial joint. Also, it is the structural component of the rib cage, the ear, the nose, the bronchial tubes, the intervertebral discs, and many other body components. It is not as hard and rigid as bone, but it is stiffer and less flexible than muscle. Examples include the rings of the trachea and the auricle/pinna of the ear.

Fig. 1.6 shows the structure of articular cartilage. It is composed of specialised cells called chondrocytes that produce a large amount of collagenous extracellular matrix (ECM), an abundant ground substance rich in proteoglycan and elastin fibres.

The cartilage is classified as elastic cartilage, hyaline cartilage and fibrocartilage, and those differ in the relative amount of collagen and proteoglycan. It does not contain blood vessels (avascular) or nerves (aneural). The nutrition is supplied to the chondrocytes by diffusion. The compression and flexion of the elastic cartilage generate fluid flow, which assists the diffusion of nutrients to the chondrocytes. Compare to other connective tissues, cartilage has a very slow turnover of its extracellular matrix.

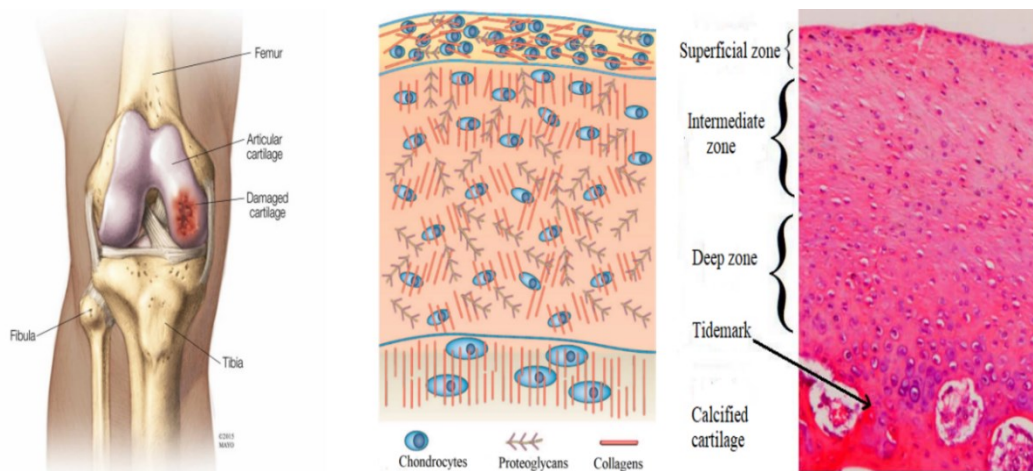


**Fig. 1.6** Zonal organisations of human articular cartilage from the superficial zone to the deep zone and the calcified cartilage (Hardin, J.A et al. 2015).

As a load-bearing material, articular cartilage has a unique composition and morphology as well as good biomechanical properties (Gonzalez and Alvarez 2014, Liu et al. 2017). It comprises an interstitial fluid phase (including 68% ~ 85% water and dissolved electrolytes) and a porous solid matrix phase (including 10% ~ 20% of collagen, 5% ~10% of proteoglycans, Chondrocytes, and other Proteins). The compressive stiffness of cartilage is positively related to the PGs concentration and negatively related to the water content. In contrast, the collagen content is predominantly responsible for the tensile and shear properties. The cartilage deformation under compression mainly depends on the interstitial fluid flow through the porous solid phase. Under low-rate dynamic loading conditions, interstitial fluid carries the major responsibility on load-bearing since it cannot be squeezed out immediately from the tissue due to the low permeability of cartilage, which depends on the PGs concentration (Song et al. 2011).



Based on the shape of the chondrocytes and the orientation of collagen fibres, cartilage is categorised into four zones: The first zone or superficial zone is characterised by the chondrocytes which appear as a flat ellipsoid in shape and having dense thin collagen fibrils parallel to the articular surface. This possesses greater tensile stiffness and strength than the deeper zones, and it may resist shear forces generated during severe stretching of cartilage. Nearly 20% of the total thickness of human articular cartilage is occupied by this zone (Doulabi et al. 2014). Enhancement of the mechanical properties of the tissue surface results from cross-linking of Proteoglycans and Collagens. The main role of this zone is to facilitate the wear and provide low frictional surfaces of the tissue. The second zone is the middle zone in which cells are a spheroidal shape and appear randomly distributed in less parallel thick collagen fibrils, as shown in Fig. 1.6. Proteoglycan content is at maximum level and the cell density is much lower than the superficial zone. This zone comprises 40 to 60% of total thickness and several times the volume of the superficial zone (Doulabi et al. 2014). The third zone is a deep zone where the cells appear to line up vertically in short, oriented irregular columns in the direction of the thick collagen fibrils perpendicular to the articular surface. The water content in this zone is low compared to the other zones. Its collagen structure is characterised by large fibers that form bundles oriented perpendicular to the articular surface. The collagen fibers in the deep zone penetrate through the tide mark into the calcified cartilage to provide structural stability for articular cartilage on the subchondral bone (Matsiko et al. 2013). Proteoglycan content is much lower than in the middle zone, and the cell density is the lowest of all cartilaginous zones. The final zone is a calcified zone separated from the deep zone by the tidemark. The stiffness values vary between the more flexible cartilage and rigid bone. In this zone, the cells are small and are distributed randomly in a matrix filled with hydroxyapatite crystals.

### *1.5.2 Cartilage Damage and Traditional repair*

Traditional cartilage repair techniques attempt to reduce pain as well as restore functionality to tissue. The success of these techniques depends on their long-term performance as well as the similarity of the repair tissue to native articular cartilage in terms of composition and mechanical properties (Mahmood et al., 2008). Regeneration

will not occur without access to cells such as progenitor cells or chondrocytes that can undergo chondrogenesis and synthesize *de novo* tissue. With this in mind, several repair strategies have been developed. Current clinical treatment techniques include Chondroplasty, Microfracture, Osteoarticular allograft, Mosaicplasty and Autologous Chondrocyte Implantation (ACI) (Sridhar et al. 2015). Chondroplasty refers to removing and reshaping collagen fibers from the rubbing surfaces of a knee joint and make the surface smooth and frictionless. Micro-fracture involves drilling holes of approximately 0.5–1 mm diameter in the damaged portion followed by the deposition of stem cells. These cells dedifferentiate and heal the defected region. The allograft process involves the transfer of cartilage from the donor site to the acceptor site. However, these technics are suitable for a lesion size is in micro-scale.

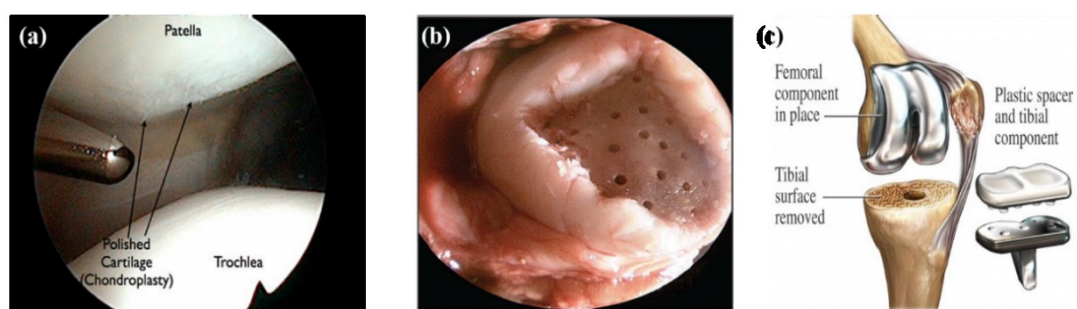


**Fig. 1.7** Cartilage repair techniques (a) Chondroplasty (b) Microfracture (c) Total knee replacement Source: (Ding. S et al., 2003).

### 1.5.3 Advances in Articular Cartilage Repair with Hydrogel

Hydrogels have drawn much attention and interest in developing cartilage scaffolds due to their unique biophysical and chemical properties. However, they are soft by nature and strength is not enough to withstand in a load-bearing environment for the orthopaedic application. Also, the biocompatibility which hinders the application *in vivo*. Blending is the scientific means to tailor the properties of the hydrogel. Silica, Alumina, Graphene oxide, Silver nanoparticles are the commonly used bio-reinforcements. The properties such as particle size, microstructure, morphology and dimensional anisotropy are the critical parameters for optimization and application.

## 1.6 Hypothesis

To address the above-mentioned issue, the present study is based on the following hypothesis:

The hydroxyapatite/calcium phosphate/titanium dioxide bioceramic reinforced Chitosan/Polyvinyl alcohol composite hydrogels will show higher mechanical stiffness with required biodegradability without compromising the physical properties for cartilage tissue regeneration application.

## 1.7 Objectives of the research work

The objectives of the present investigation are:

- To synthesise the bioceramic Hydroxyapatite and Bi-phasic calcium phosphate nanorod through mechanochemical method followed by the heat treatment process. Also, to develop Titanium Dioxide Nanotubes.
- To characterise the bioceramics using Field Emission Scanning Electron Microscope (FESEM), X-ray diffraction (XRD) and Fourier Transmission Infrared Spectroscopy (FTIR).
- To process the Chitosan/Hydroxyapatite (CS/HANr), Chitosan/Biphasic Calcium Phosphate (CS/BCP), Chitosan/Titanium Dioxide Nanotube (CS/TNT), Polyvinyl alcohol/Hydroxyapatite (PVA/HANr), Polyvinyl alcohol/Biphasic Calcium Phosphate (PVA/BCP) and Polyvinyl alcohol/Titanium Dioxide Nanotube (PVA/TNT) composite hydrogel through freeze-thaw technique.
- To assess the physical properties like swelling, pore size and porosity and contact angle measurements and compare the results with the properties of the human natural articular cartilage.
- To evaluate the mechanical and rheological properties of the hydrogels, compare the results with the properties of the natural articular cartilage.
- To analyse the antimicrobial activity of the hydrogel against the microbes *Escherichia coli*, *Staphylococcus aureus* bacteria's and *Candida albicans* fungi and cell viability towards L929 and MG 63 fibroblast and osteoblast-like cells.

## **1.8 Thesis Structure**

The present dissertation is organized into seven chapters as follows.

**Chapter 1** discusses evaluating the biomaterials from the Neolithic period to date, scope and objective of the present research work.

**Chapter 2** reviews the literature related to various natural and synthetic polymers used to develop the hydrogels and to the study of the effect of the various reinforcement on physical and mechanobiological properties of hydrogels used for soft tissue regeneration application.

**Chapter 3** describes the “materials and methods” used for bioceramic nanomaterial synthesis such as nanohydroxyapatite, biphasic calcium phosphate and titanium dioxide nanotube. The processing and characterization of various hydrogels have been discussed.

**Chapter 4** presents the influence of bio-ceramic reinforcements on the physical and mechanobiological properties of chitosan composite hydrogel has been discussed. Also the viability of human fibroblast and osteoblast cells after 72 h of culture was studied.

**Chapter 5** describes the influence of bio-ceramic reinforcements on polyvinyl alcohol (PVA) hydrogel was investigated. The physico-mechanical, bio-tribological properties biochemical properties of the implant material was investigated.

**Chapter 6** investigates the processing of nanohydroxyapatite porous scaffolds for bone tissue engineering and the required mechanical and biochemical characterization for the proposed application was evaluated.

**Chapter 7** recaps the result and discussion, highlights the accomplishments for the future study.



## CHAPTER 2

### LITERATURE REVIEW

---

Polymeric biomaterials give desirable properties to use as a scaffold material for a load-bearing application. However, few literatures are reported that plastic polymers start to leach out when it comes in contact with body fluids that may lead to chronic infection. Besides, the hard polymeric surface causes the friction effect that leads to an inflammatory reaction in the surrounding cells. Therefore, scientists focused on soft polymers that show low surface friction and wear against rubbing surfaces. The scientific literature about the first soft polymer appeared in the year 1960. Wichterle and Lim were the first to report on 'hydrogel' using poly (2-hydroxyethyl methacrylate) (pHEMA) gels for use as soft contact lenses. Later, the research was focused on simple, non-toxic crosslinked polymers for ophthalmic and drug delivery applications. In 1986, Roorda and his co-workers developed polyethylene glycol (PEG) hydrogels for drug delivery application and the reports confirm that drug-loaded hydrogels provide a matrix-type delivery profile, in which the drug release rate is directly proportional to the square root of time (Roorda et al. 1986).

Protein-based natural polymers are advantageous because they contain ligands that can be confessed by cell-surface receptors. Chitosan ( $C_6H_{11}NO_4$ )<sub>n</sub>, Gelatin, Alginate ( $C_6H_8O_6$ )<sub>n</sub> are the commonly used natural polymers for hydrogel preparation. However, the low mechanical strength and higher degradability impede the use as scaffold material, especially for load-bearing applications. Synthetic polymers such as Poly (2-hydroxyethyl methacrylate) (pHEMA) ( $C_6H_{10}O_3$ )<sub>n</sub>, Polyvinyl alcohol (PVA) ( $CH_2CHOH$ )<sub>n</sub>, Poly(N-isopropyl acrylamide) (PNIPAM) ( $C_6H_{11}NO$ )<sub>n</sub>, Polyethylene glycol (PEG) ( $C_{2n}H_{4n+2n}O_{n+1}$ ), Polyglycolide (PGA) ( $C_2H_2O_2$ )<sub>n</sub> and Polycaprolactone (PCL) ( $C_6H_{10}O_2$ )<sub>n</sub> were used to develop hydrogels as implant material. However, they have a few drawbacks, like non-adhesive with the neighbouring tissues. Table 2.1 summarises a few commonly used natural and synthetic polymers and their key application as biomaterial hydrogel.

**Table 2.1** Natural and synthetic polymers, key benefits and their applications

(Buwalda et al. 2014; Roorda et al. 1986; Zaman et al. 2015).

Polymer	Class	Advantage	Disadvantage	Application
<b>Natural polymers</b>				
Collagen	Proteinaceous	Adhesive, bioactive, biodegradable and mimics extracellular matrix	Low mechanical stability	Wound dressing
Gelatin	Proteinaceous	Adhesive and bioactive	Mechanically weak	Skin regeneration
Silk	Proteinaceous	High mechanical strength and low immunogenicity	Long gelation time	Cartilage regeneration
Alginate	Proteinaceous	Abundant, rapid gelation with divalent cations. Ease of use for 3D printing	Non-biodegradable and poorly adhesive	Wound healing
Chitosan	Proteinaceous	Antimicrobial, abundant and low immunogenicity	Low immunogenicity	Cartilage regeneration
<b>Synthetic polymers</b>				
pHEMA	Polyvinyl	High mechanical strength biocompatible	High monomer toxicity	Nerve regeneration
PVA	Polyvinyl	High elasticity, high biocompatibility and hydrophilicity	Non-adhesive	Skin regeneration
PMMA	Polyvinyl	Temperature responsive	Monomer cyto- and neuro-toxic	Drug delivery
PEG	-	Versatile architecture and functionality	Non-adhesive	Controlled drug delivery
PLA and PGA	Polyester	Degradable by hydrolysis	Low mechanical strength	Drug delivery
PCL	Polyester	Degradable by hydrolysis and crystallinity provides mechanical strength	Cost	Cell printing

Over the past four decades, significant research has been done in the field of hydrogels for a load-bearing application like a cartilage implant or scaffold material. Polyvinyl alcohol, Silk fibroin hydrogels are commonly used for cartilage scaffolds.

However, it has been recognised that they are bio-inert and it does not encourage cell attachment, proliferation and inefficacy in protein adsorbability. Thus it suppresses the biological bond formation between living tissue scaffolds. Also, poor mechanical and water retention ability hamper their wide range of applications *in vivo*. The logical way to enhance the mechanobiological properties of the hydrogel is by modifying the processing mechanism and adding reinforcements. The detailed study of nanoparticle reinforced hydrogel by the various researchers was listed in Table 2.2 according to physical, mechanical and biological property evaluation.

**Table 2.2** Nanoparticle reinforced composite hydrogels.

<b>Polymer</b>	<b>Reinforcement</b>	<b>Results</b>	<b>Author/s and year</b>
PVA	Silver nanoparticle	The AgNp reinforced PVA hydrogel can release the nanoparticle at the targeted area in a controlled manner for at least 96 h.	(Bhowmick and Koul 2016)
PVA	Graphene oxide (GO)	The incorporation of GO dramatically enhances the tensile mechanical properties (17 %) of composites compared to neat PVA hydrogel.	(Peng et al. 2016)
PVA	Calcium Phosphate	The physical freeze-thaw process develops micro and nano porosity (78 %) which is essentially needed for subchondral bone tissue formation	(Timofejeva et al. 2017)
Chitosan  <b>Contd.,</b>	Carbon nanotube	Chitosan-CNT hydrogel exhibited a well-defined pore structure with water uptake and retention ability. Besides, Chitosan-CNT hydrogel showed strong antimicrobial	(Venkatesan et al. 2014)



		activity against <i>S. aureus</i> , <i>E. coli</i> and <i>C. tropicalis</i>	
Chitosan	Silver nanoparticles	Chitosan-silver nanoparticle reinforced hydrogel was developed by freeze-lyophilization technique. Composites having 3 wt. % of nanosilver exhibit good antimicrobial property and does not shows any toxicity even after 24 h if culture.	(Tyliszczak et al. 2017)
Chitosan and collagen	Silica nanoparticle	The hydrogels prepared from collagen with silica nanoparticles promote mineralization and are potentially useful candidates for bioactive injectable systems for bone tissue repair.	Acucka et al. 2015
Alginate-polyvinyl alcohol-	hydroxyapatite	Composite hydrogel with optimal rheological properties for 3D bioprinting of mouse calvaria 3T3-E1 (MC3T3) cells into scaffolds of high shape fidelity has been developed.	(Bendtsen et al. 2017)
N,N'-methylene bisacrylamide (MBA) <b>Contd.,</b>	cellulose	High water retention potency of the double network hydrogel was found and it can reach up to 330 g/1 g of the dry hydrogel. The addition of MBA provides higher transparency with increased pore size.	(Geng 2018)

Polyvinyl alcohol	Chitosan nanoparticles	Nanocomposite PVA hydrogel with 5, 10 and 15 wt% of chitosan nanoparticles was reinforced through the freeze-thawing process. The developed nanocomposite hydrogel shows favourable fluid absorption with good mechanical strength and excellent barrier against microbial penetration.	(Farzinfar and Paydayesh 2019)
Silk fibroin	poly-ethylene glycol diglycidyl ether (PEGDE)	Silk fibroin hydrogels were prepared by cryo-gelation technique. The developed hydrogels have a compressive strength of 50 MPa which is four times higher than the compression strength of human articular cartilage.	(Parkes et al. 2015)
Cellulose	Polyacrylamide	The behaviour of the hydrogel material and the shape of the cyclic curve obtained with various deformation speed was studied. The time-dependent, rapid self-recoverable, fatigue-resistant mechanism of hydrogel under loading-unloading compression test was also performed.	(Gofman and Buyanov 2017)
Poly(lactic-co-glycolic acid) (PLGA) <b>Contd.,</b>	gelatin	A combination of superior swelling and mechanical, especially compression strength,	(Jung et al. 2018)

		was observed compared to pure gelatin hydrogel.	
PVA	Sodium alginate	Composite hydrogels were prepared by the electrospinning method. The morphology of the 3T3 cells on the electrospun fibers after 1 day of incubation confirms that fibers support the cell attachment. Further cell to cell communication was noticed after 3 days of incubation confirms that cells start to proliferate. The ECM production and cell ECM communication were observed after 7 days of incubation.	(Ming et al. 2016)
Chitosan	nano-silica	The introduction of 25% of nano-silica viscosity and shear stress markedly decreases. The storage modulus values increase markedly indicating abundant entanglement network formation.	(Liu et al. 2019)
PVA  <b>Contd.,</b>	hydroxyapatite	The torsional friction behaviour of composite hydrogel was evaluated against Co-Cr-Mo femoral head. The results confirm that as applied load increases, the friction coefficient and adhesion zone increases gradually, similarly, as the torsion angle increases, the friction coefficient and contact interface zone increases. This	(Chen et al. 2016)

		causes a decrease in fluid load support.	
Chitosan	Silver nanoparticles	The antimicrobial activity of chitosan and silver nanoparticles was assessed against <i>Staphylococcus aureus</i> and <i>Enterococcus faecalis</i> through the disc-diffusion method. The results reported that chitosan has good antimicrobial activity and the addition of 3 mL of silver nanoparticles enhances the mechanical stiffness and superior antimicrobial properties.	(Tyliczszak et al. 2017)
PVA-Chitosan	Nanocellulose	The cytocompatibility of the composite hydrogel towards L929 mouse fibroblasts was evaluated using an MTT assay. The analysis exposed that the composite samples did not have any toxicity and cells can adhere, proliferate and dedifferentiate on the scaffold surface after 72 h of incubation.	(Kanimozhi et al. 2018)

## 2.1 The literature on Natural Polymers

### 2.1.1 Chitosan

Chitin is a natural polysaccharide, identified in 1811 by French chemist Henri Braconnot. It was found in the extracellular matrix of a certain organism as a proteoglycan. Chitosan, which was discovered and named in 1859 by Roget obtained by partial deacetylation of chitin under alkaline conditions. Chitosan is the most abundant natural mucopolysaccharide next to cellulose. It is a linear polysaccharide composed of randomly distributed  $\beta$ -(1-4 D-glucosamine) and N-acetyl-D-glucosamine

derived from the exoskeleton of insects and the shells of crustaceans such as Shrimps, Clams and Lobster. The diverse biological activities of its derivatives invite researchers from various fields, especially in biomaterials and biomedical science. The biological characteristics of chitosan are mainly dependent on its ability to dissolve in water and other solvents (Kim 2018). Deacetylation and molecular weight are the crucial parameters that decide the bioactivity since the primary amino groups are the key functional groups that permit interaction with the neighbouring molecule. When deacetylation increases, the solubility of chitosan increases and more possible interactions are permitted between the available sites of chitosan and the other molecules. Higher deacetylation and low molecular weight significantly influence the better antioxidant, anticoagulant, antibacterial, antifungal, anti-tumour, and hemostatic properties.

The functional groups of chitosan can easily modify the physical and chemical properties by interacting with the neighbourhood. In acid hydrolysis, the temperature and acidic concentrations are the critical parameters that decide the physical, mechanical and biological properties of the chitosan scaffolds. Based on the crosslinking mechanism chitosan hydrogels are classified as physical, chemical and metal-coordinate hydrogels. In physical hydrogels, the physical forces such as hydrogen bonding, electrostatic interaction and hydrophobic interaction make crosslinking while chemical bonding involves crosslinking of two or more polymers by covalent bonds. In metal-coordinate hydrogels, the bonding involves metal-ligand coordination between the polymers.

The advantage of the physical crosslinking approach is that it does not require crosslinking agents, which sometimes causes toxic effects and hinders biocompatibility. Besides, the physical hydrogels are the self-healing property by reverse bonding or hydrophobic association mechanism. The general method for developing chitosan hydrogel without chemical crosslinkers is the freeze-thaw method. In this approach, the developed gels were frozen for a certain temperature and thawing at room temperature which promotes physical interaction between the polymer chains.

Chitosan is having one amine and two hydroxyl reactive functional groups as shown in Fig 2.1. They are ready to crosslink with neighbouring chains to form the

hydrogel. Likewise, the lone pair of electrons of the amine and hydroxyl groups allows the formation of coordinate bonds across the chitosan chain. The various cross-linkers used for chemical crosslinking include aldehydes, diisocyanates and genpin.

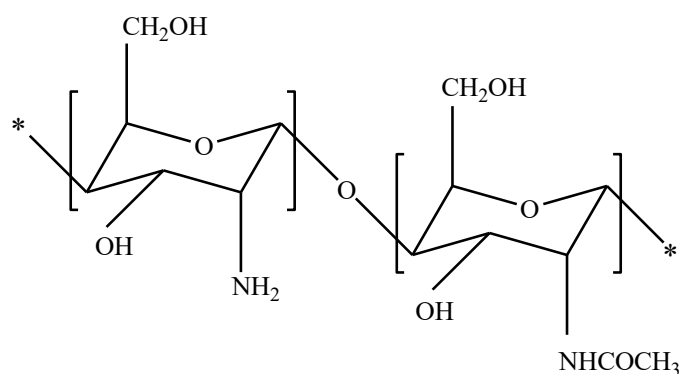


**Fig. 2.1** Chemical structure of chitosan

Due to their superior antimicrobial potency, chitosan hydrogels are a well-known material for wound dressing application. This antimicrobial property is ascribed to the positive charge of the amino groups of chitosan which actively interacts with the negatively charged microbial cell membrane making cytoplasmic leakage leading to the death of microbes. The other application of chitosan hydrogel includes drug delivery, bone and cartilage regeneration and adsorbents. Also, chitosan hydrogels are widely used in agriculture applications for efficient delivery of agrochemicals and pesticides. Besides, they are also used in wastewater treatment, removal of metal ions, dyes and phenols.

### 2.1.2 Gelatin

Gelatin is a natural origin water-soluble derived from hydrolysis of collagen have been extensively used in pharma industries and biomedical field due to its superior biocompatibility and biodegradability. It is a mixture of amino acid moieties joined by a peptide bond with a molecular weight between 10,000 to 400,000 Da. These molecules are made of a repeated sequence of glycine-X-Y-triplets where proline for X and hydroxyproline for Y positions are the most common amino acids. During the hydrolysis process, tertiary collagen structure was broken down into single  $\alpha$ -chain, covalently crosslinked  $\beta$ -chain and triple  $\alpha$ -chain species ( $\gamma$ -chain). Gelatin based hydrogels are finding their application in drug delivery and tissue engineering since

they can promote cell adhesion and proliferation. Additionally, it has a superior adsorption potency, and therefore it is widely employed for wound dressing.

The mechanical stiffness of the gelation hydrogel is determined by the processing parameters such as temperature, pH and bloom strength. Bloom strength is the intrinsic force formed in the hydrogel when it is cooled. Crosslinking of the hydrogel plays a crucial role in the final stiffness value of the hydrogel. Similar to the chitosan hydrogel as discussed above, both physical and chemical methods were employed. Physical crosslinking was achieved by Microwave energy, hydrothermal and ultraviolet radiations were employed without the use of toxic chemicals. However, control over crosslinking density and process efficiency is often low. In the chemical crosslinking process the use of chemical agents which activates the functional groups of gelation molecule. Commonly used chemical crosslinking agents are aldehydes, polyepoxides and isocyanates.

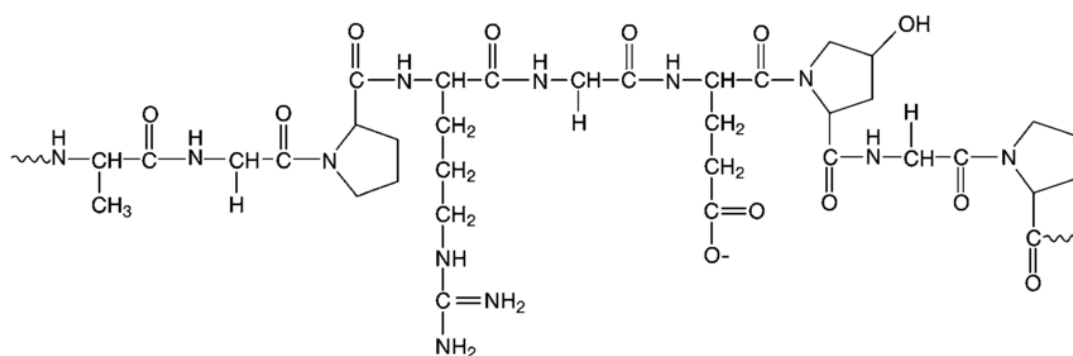


**Fig. 2.2** Chemical structure of gelatin (Kommareddy et al. 2007)

Over a decade, many efforts have been made to develop gelatin hydrogel scaffolds for various applications such as skin regeneration, wound healing, nerve and cardiac tissue regeneration. Various processing techniques have been employed to achieve the required physical, mechanical and biological property for the intended application. Freeze drying, foam templating, particle leaching, electrospinning and bioprinting are the few common fabrication techniques for scaffold preparation.

The main drawback of gelation hydrogel scaffolds is insufficient mechanical stiffness for bone tissue engineering. This can be overcome by incorporating suitable reinforcements such as silver nanoparticles, zirconia and calcium phosphates. This induces additional hydrogen bonds between matrix and reinforcement, thereby

increases the mechanical stiffness. The calcium phosphate reinforcements impact on alkaline phosphate activity and bone mineralisation which supports new bone formation.

### 2.1.3 Cellulose

Cellulose is an organic natural polysaccharide material consisting of several units of D-glucose units. It is the primary component of the cell wall of all trees, few algae and some species of bacteria secrete it in the form of biofilms. It was first discovered by Anselme Payen in the year 1838 from a plant source and determined the chemical formula  $(C_6H_{10}O_5)_n$ . Cellulose is a straight-chain polymer in which hydroxyl groups of one side chain form a hydrogen bond with the oxygen atoms of the neighbouring chain. The properties of cellulose depend on the polymer chain length. The cellulose derived from wood pulp has a typical chain length of 300 units. Similarly, cotton and bacterial cellulose have a chain length of 800-10000 units. Molecules with higher chain length are having mechanically stable. However, they are typically insoluble in water and other organic solvents.

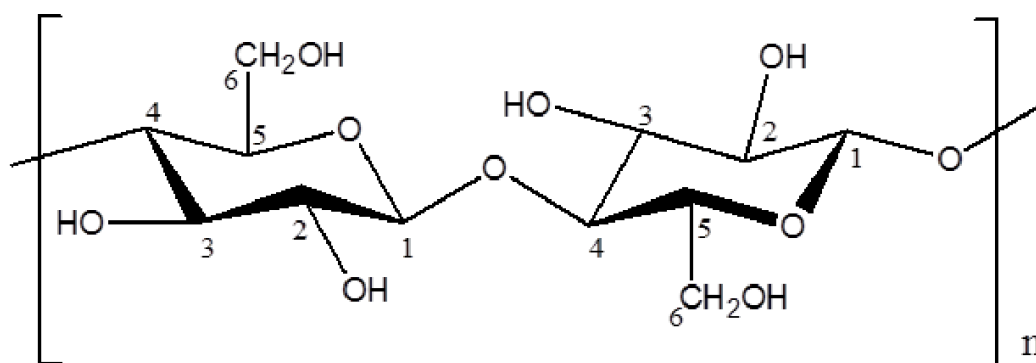


**Fig. 2.3** chemical structure of cellulose (Hussin et al. 2018)

Cellulose hydrogels can be prepared by both physical and chemical cross-linking methods. It has plenty of hydroxyl groups that can form hydrogen bonding with the neighbouring polymer chain, as shown in Fig 2.3. However, the stability of the main chain makes the polymer insoluble under normal conditions. Few solvents such as *N*-methyl morpholine-*N*-oxide (NMMO), ionic liquids (ILs), and alkali/urea (or thiourea) can dissolve the polymer main chain which provides an opportunity for developing cellulose hydrogels.



The hydrogel network requires a minimum rigidity and strength to sustain in an *in vivo* environment. Blending is an effective way to obtain the desired properties. Cellulose is generally blended with starch, chitosan, alginates to remove heavy metal ions and tissue engineering application. Also, cellulose was blended with synthetic polymer polyvinyl alcohol to enhance the biocompatibility of the synthetic hydrogel. Cellulose hydrogels are mainly used as water reservoirs in agriculture. This is mainly to reduce the use of excess water. Cultivation in the desert region where water is scarce, these hydrogels in the form of powder or granules were mixed with the soil in the area close to the roots. These hydrogels are loaded with the nutrients and essential antibiotics needed for the plant. When the soil is watered, the hydrogels absorb large excess water and release it when the soil needed it by a diffusion-driven mechanism. This makes soil humid for a long time with a little amount of water. The advantage of these hydrogels is, once these polymers are dried make soil porous providing oxygenation to the plant root (Sannino et al. 2009).

Several hydrogels are available to absorb water and release it in a controlled way. However, most of the products are not suitable for agricultural applications. The water retention potency and toxicity hinder the application. It is worth noting that synthetic hydrogels are not biodegradable and are not eco-friendly. The cellulose hydrogels are perfectly suits for the application to develop eco-friendly friendly alternative superabsorbent hydrogels.

#### 2.1.4 Alginate

Alginate is a naturally occurring anionic polymer obtained from brown seaweed that has been widely used in the biomedical field. The structural similarity of the alginate hydrogel is similar to the mammalian tissue and the biocompatibility, nontoxic properties attract these hydrogels to use as a tissue scaffold biomaterial. Also, alginate has higher antimicrobial characteristics which prevent infection and support would healing process. The hydrogels developed from the alginate polymer are porous which supports cell proliferation in removing excretion in the biological environment.

The properties of alginate such as molecular weight in the range 32000-400,000 g/mol. The average viscosity of the hydrogel increases with decreasing pH and reaches a maximum value at a pH of 3-3.5. The molecular weight of the alginate improves the

physical properties of the hydrogel. However, the higher molecular weight makes the gel thicker which is very difficult to process. For example, cells are infused into the thicker polymer may cause damage while shear force generated while mixing. The elastic modulus of the polymer can be tuned by mixing the high and low molecular weight polymer with a different proportion.

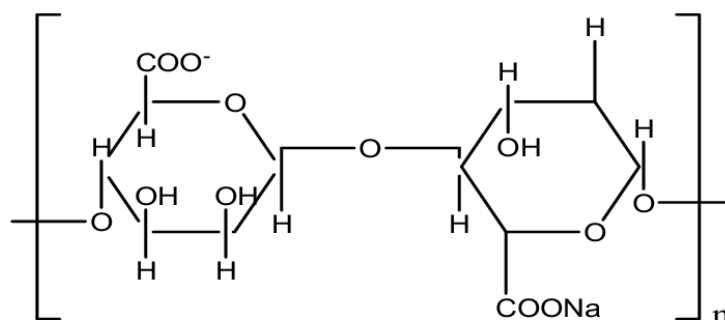


**Fig. 2.4** Chemical structure of sodium alginate molecule (Homayouni et al. 2007)

Various methods were used to develop alginate hydrogels includes ionic crosslinking, covalent crosslinking, cell crosslinking and thermal gelation. In ionic crosslinking, the alginate solutions were mixed with the ionic crosslinking agents such as divalent cations which bind the guluronate blocks of the alginate chain. These blocks of the polymer chain make a junction with the blocks of the adjacent polymer resulting in a long chain structure. The important parameters which affect the properties of alginate hydrogel are gelation rate, temperature and guluronate concentration. Slower gelation produces a uniform network and superior mechanical strength of the hydrogel. Similarly, at a lower temperature, the reactivity of the cations is lower provides a stable network structure. Additionally, the mechanical stiffness of the hydrogel essentially depends on the concentration of the guluronate in the chemical structure.

In covalent crosslinking hydrogels, the additional chemical bonds increase the mechanical stiffness while physical properties such as swelling and water retention potency decrease dramatically. Also, the toxic chemical reagents hinder cell adhesion *in vivo*. In thermosensitive hydrogels, the physicochemical properties of the hydrogel can be adjusted by varying the processing temperature. Alginate hydrogels for drug delivery applications are made of thermal treatment that shows controlled drug delivery without any toxic effect.

## 2.2 The literature on Synthetic hydrogels

### 2.2.1 Polyvinyl alcohol (PVA)

Polyvinyl alcohol is a water-soluble synthetic polymer with a chemical formula  $[\text{CH}_2\text{CH}(\text{OH})]_n$ . PVA was first developed by Baum in 1924 by using a vinyl acetate and since started to use this as a biomaterial due to its biodegradability, water-absorbing potency, low toxicity and adhesive properties. It consists of a repeated unit of vinyl alcohol and is derived from monomer vinyl acetate which is polymerised to form polyvinyl acetate. This undergoes saponification to form polyvinyl alcohol.

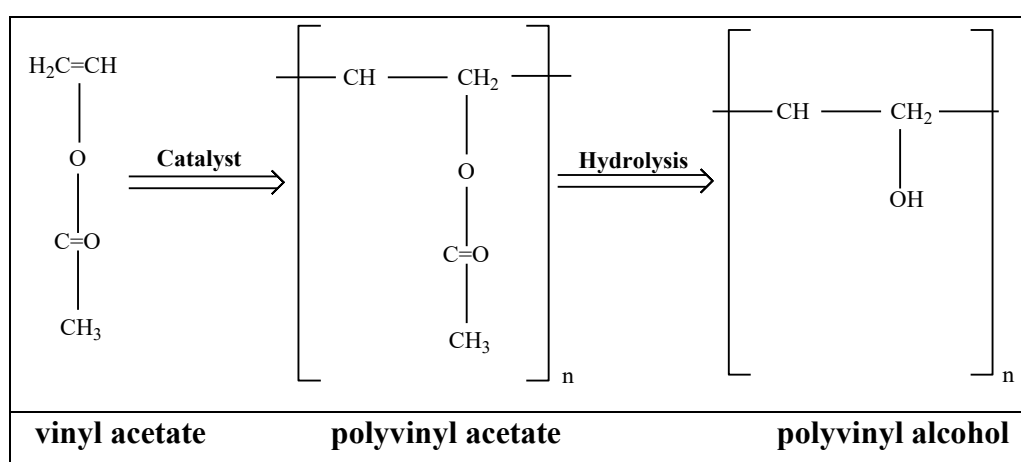


**Fig. 2.5** Chemical reaction in the formation of PVA

Most of the physical properties of the polyvinyl alcohol hydrogels closely mimic the properties of mammalian tissue. Their pH-sensitive property with the host indicating that they are stimuli-responsive hydrogels for controlled drug delivery. There are two methods for gelation of PVA hydrogel; physical and chemical crosslinking. Covalent crosslinking is the permanent gelation method that provides superior mechanical strength. However, the use of surfactants may hinder biodegradability and toxicity was taken into account. Physical crosslinking was formed when physical entanglement by the secondary forces such as hydrogen bonds are electrostatic forces between the hydroxyl groups of a polymer chain with the neighbouring polymer chain. However, this crosslinking is highly sensitive to the physical variations such as ionic strength, temperature and pH of the system. Several factors determine the properties of the polyvinyl alcohol hydrogel. A few of them are the degree of deacetylation, molecular weight, and polymer concentration and freeze-thaw cycles.

Previous researchers have been reported that PVA solutions with a lower degree of deacetylation produce weak bonds irrespective of the degree of freeze-thawing. The O-acetyl groups reduce the formation of intermolecular bonds. The molecular mass of the polymer is another important parameter for PVA hydrogels. The polymer with a higher molecular mass is preferred for the development of strong and elastic hydrogel. The increasing polymer chain length, the degree of overlapping, topological entanglements and intermolecular interaction affect the hydrogel stability. Also, a denser polymer network was developed with increasing crystallite size. Polymer concentration, tacticity can also play a vital role in the final physicochemical and biological properties of the PVA hydrogel.

The mechanism of intermolecular bonding in PVA hydrogel is still under debate. Few researchers have reported that when the PVA solution freezes, the solvent part of the mixture freezes and the solute will remain in the liquid phase. When the solution is kept at atmospheric temperature, the solute part will be separated from the liquid phase and hydrogen bonds will exist between the PVA chains. The degree of crosslinking is mainly related to the number of freezing and thawing cycles. The major parameter influencing the crosslinking density is the freezing rate. It was found that, with a slow thawing rate ( $0.01-0.05 \text{ K min}^{-1}$ ), elastic hydrogels were formed. While fast thawing, freezing makes hydrogel hard that causes cracks on its surface.

The gelation phenomenon of PVA hydrogels undergoes three stages. In the first stage, as the temperature of the PVA solution decreases, the molecular movement of the polymer chain decreases. As a result, intermolecular integration raises and forms crystalline nuclei. The formed nuclei initiate the crosslinking and form the 3D PVA network. When the system thaws, due to incomplete crystallisation, the ice crystals melt leaving pores behind. These pores are stabilised due to the formation of PVA crystallites which act as junction knots in the PVA 3D network.

Blends of PVA with other natural or synthetic polymers were used and explored for developing composite hydrogels. PVA is blended with chitosan to make PVA-chitosan composite hydrogel for tissue-engineered scaffolds for artificial cartilages. Similarly, cellulose, cotton fibers, silk fibers, xanthan, sorbitol are the common blends for tissue-engineered scaffold preparation. Also, a few bioceramics and metallic reinforcements

such as calcium phosphate, alumina and silver were commonly used reinforcements for polyvinyl alcohol hydrogel.

### 2.2.2 Poly (ethylene glycol) (PEG)

Poly (ethylene glycol) is one of the most widely used synthetic polymers for hydrogel preparation. They are characterised by low toxicity with the surrounding tissue, superior biocompatibility, low surface tension and solubility in water makes them a good candidate for drug delivery and hemocompatible scaffolds.

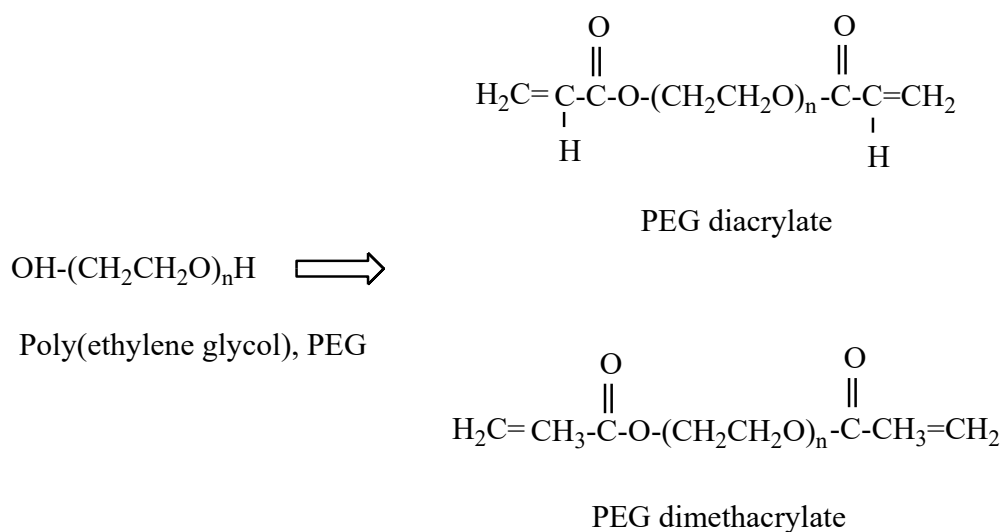


**Fig. 2.6** chemical structure of PEG and its derivatives

The derivatives of PEG such as polyethylene glycol methacrylate (PEGMA), polyethylene glycol dimethacrylate (PEGDMA) and polyethylene glycol diacrylate (PEGDA) are used for protein recombination and functional tissue production. They are stimuli sensitive and they readily react in the presence of physical and chemical agents and therefore, these hydrogels are known as *smart* or *intelligent* hydrogels. The chemical structure of PEG and its derivatives are as shown in Fig. 2.6.

Wang et al. developed the composite hydrogel by mixing methacrylic acid (MAA) with PEG through free-radical photopolymerisation using tetra (ethylene glycol) dimethacrylate crosslinker. The author has claimed that the swelling and drug release efficacy depending on the molecular weight and these hydrogels are mainly used for the insulin release systems (Wang et al. 2017). Another researcher modified PEG with  $\beta$ -chitosan by using UV radiation as a cross-linker. The composite structure

shows an increased water absorption by 13% in compression to pure neat PEG hydrogel (Sridhar et al. 2015).

### 2.2.3 Poly (hydroxyethyl methacrylate) hydrogels (PHEMA)

It was developed by polymerizing 2-hydroxyethyl methacrylate monomers using an ethylene glycol cross-linker. The hydrophilic characteristics of this are due to the presence of the hydroxyl groups at the end of the monomer as shown in Fig. 2.7. These end groups try to develop hydrogen bonds with the water molecule and make the polymer matrix.

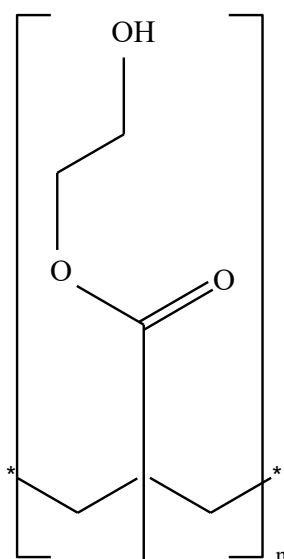


**Fig. 2.7** Chemical structure of Poly (hydroxyethyl methacrylate)

These hydrogels were first developed in 1962 by the Western European Association. Later in 1965, the National Patent Development Corporation (NPDC) took the license and sold it to Bausch & Lomb who worked on ophthalmic equipment. They have modified the processing technic and in 1971, these lenses were launched into the market. During that time, these lenses were very popular. However, very soon, it was clear that these lenses are not problem-free.

To increase the oxygen transmissibility and high water content in the lenses, Methyl methacrylate (MMA) was blended with PHEMA. When MMA was mixed during polymer formulation, the ionized groups within the matrix allow the lenses to absorb more amount of water thereby increases the oxygen permittivity.

#### 2.2.4 Polyacrylamide

Polyacrylamide ( $-\text{CH}_2\text{CHCONH}_2-$ ) is a straight-chain readily crosslinked acrylamide. They are suitable candidates for biomaterial application due to their biocompatibility, chelation and attractive physical and mechanical properties. Polyacrylamide hydrogels are used as a carrier for drugs, genes and carry physiologically important substitutes in a controlled manner. Synthesis of polyacrylamide hydrogels was carried out using radiation method, crosslinking and free radical polymerization method.

These hydrogels are widely used to remove toxic metal ions since they contain one or more electron donor atoms such as N, S, O and P that can form a coordinate bond with the heavy metal ions. Another major application of polyacrylamide hydrogels are targeted and control release of 5 FU drug for cancer treatment. In agricultural application, the powders of polyacrylamide were used for long time water storage for plant growth in gardening in the name of water-gel crystals. However, the toxicity of the monomer units (acrylamide) hinders the benefits of water storage and controlled release.

#### 2.2.5 Poly (lactic acid) and poly (glycolic acid)

In thermoplastic biopolymers, Poly (lactic acid) and poly (glycolic acid) are the most studied polymeric materials due to their biocompatibility and they have been approved by the US Food and Drug Administration for clinical application. Since 1990, these polymers were extensively studied for tissue engineering applications especially for hard tissue such as bone and cartilage scaffolds. However, the intermediate degradation of the low molecular weight polymer causes the intermediate degradation makes the decrease of local pH induces the inflammatory reaction and damages the bone cells at their implant site. This results in the loss of mechanical strength before new bone formation.

This issue can be resolved by controlling the concentration of poly (glycolic acid) in the blend. The increased concentration of Poly (lactic acid) takes the degradation time which would provide sufficient time for cell proliferation and support the tissue regeneration during wound healing. The electrospinning, room temperature

ionic liquid and solvent-free extraction are the general methods for developing the Poly (lactic acid) and poly (glycolic acid) blends.

The other application of these scaffolds includes temporary management of pathologically altered tissue including tendons, ligaments, skin, vascular tissues and muscle. These implanted materials provide structural supports and they can degrade completely in the body in a controlled manner.

### 2.2.6 The literature on hydroxyapatite and calcium phosphate bioceramics

Hydroxyapatite, HAp ( $\text{Ca}_{10}(\text{PO}_4)_6\text{OH}_2$ ), is a naturally occurring mineral form of calcium apatite. It is the commonly used material for bone tissue repair or regeneration due to its excellent biocompatibility, non-toxicity, superior mechanical strength and osteoconductivity, forming a biological and chemical bond with the surrounding tissue *in vivo*. Hydroxyapatite is the major constituent of mammalian bone, 55-70 wt% of human adult healthy bone consisting of calcium phosphate. It has a hexagonal crystal structure with a specific gravity of 3.08. The chemical structure of hydroxyapatite is as shown in Fig. 2.8.

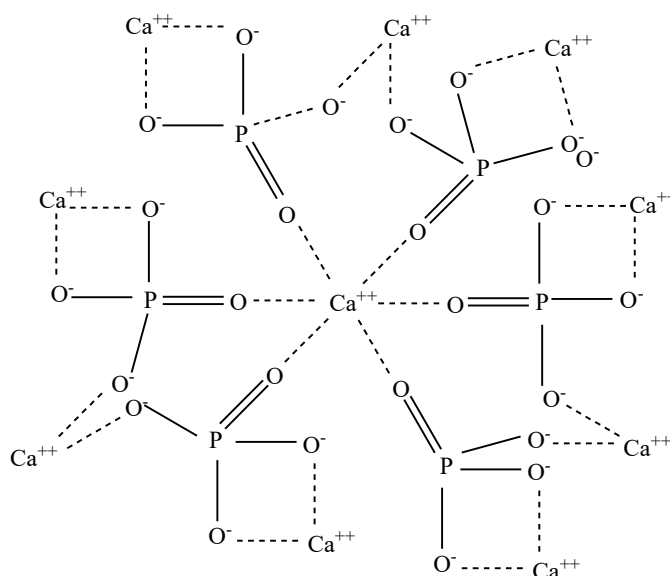


**Fig. 2.8** Chemical structure of Hydroxyapatite

The hydroxyapatite crystal structure consists of quasi-compact packing of phosphate groups, which forms two types of tunnels parallel to the c-axis. Hydroxyapatite can be obtained by natural and synthetic means. For synthesizing hydroxyapatite in bulk, chemical methods like sol-gel, hydrothermal, microemulsion,



polymer assisted and electrodeposition technics are employed (Venkatesan et al. 2018). However, the use of chemicals during synthesizing may affect cytocompatibility *in vivo*. On the other hand, natural resources such as bio-waste fish and animal bones were used for hydroxyapatite synthesis. Thermal calcination is the generally employed technique for hydroxyapatite synthesis since the method is very simple and inexpensive. Besides, large quantities can be produced in a short period. Hydroxyapatite can be used for various applications such as artificial hard tissue scaffolds, bioactive coatings, drug delivery, biosensors and wastewater treatment.

### 2.2.7 Hydroxyapatite from biowaste cuttlefish bone

Cuttlefish are found in the Mediterranean, Baltic Seas and the Indian Ocean. Its bone primarily consists of an aragonite porous internal structure that facilitates buoyancy. It consists of two parts: a dorsal shield (external region) and an internal lamellar region. Adult cuttlefish bones have 100 parallel chambers with a height of around 600  $\mu\text{m}$ . Generally, the dorsal shield is covered by the internal lamellar region. A digital photograph of the cuttlefish bone is shown in Fig. 2.9. It is a highly complicated structure consisting of peptides, polypeptides, proteins, polysaccharides and lipids (Venkatesan et al. 2018).



**Fig. 2.9** Photograph of the cuttlefish bone

The hydroxyapatite synthesis from the chemical sol-gel method involves the use of toxic chemical precursors such as calcium nitrate and di-ammonium phosphate. However, for natural synthesis, calcium nitrate was replaced by marine waste cuttlefish

bone-derived calcium carbonate and orthophosphoric acid ( $\text{H}_3\text{PO}_4$ ) was used to achieve a stoichiometric molar ratio of 1.667 (Ca/P).

Several researchers used different methods for developing hydroxyapatite. Pal et al. 2017 reported the synthesis of hydroxyapatite from calcarifer fishbone by using a simple treatment in the temperature range  $200^\circ$ - $1200^\circ$ . When the calcination temperature reaches  $800^\circ\text{C}$ , the powder was converted into hydroxyapatite with a small trace of CaO. As the temperature rises further, the hydroxyapatite phase was disappeared and changed to calcium phosphate. (Pal et al. 2017a). Sabu et al. 2019 developed nanohydroxyapatite using bio-waste eggshells in assistance with microwave heating. The scanning electron images show the interwoven hierarchical structure with remarkable variations in the morphological features compared to the conventionally proceed technique. The potential chicken eggshell calcium source was utilized for developing hydroxyapatite was investigated by Ferro et al. 2019. The slightly varied mechanochemical method provides a new window for developing simple, reliable and cost-effective hydroxyapatite production on a large scale (Ferro and Guedes 2019).

#### *2.2.8 Hydroxyapatite synthesis from chemical method*

The morphology of the nanomaterials plays a crucial role in specific drug delivery applications. Xia et al. 2018 reported the development of nanohydroxyapatite with different morphology such as rods, balls blocks using a hydrothermal method (Xia et al. 2018). The di-ammonium phosphate was used as a calcium source. The high-resolution transmission electron microscopy (HRTEM) images confirm that calcium carbonate could be converted into hollow nanohydroxyapatite with a higher surface area and mesoporous structure. Similar work was done by Bensalah et al. 2018 for synthesizing hydroxyapatite nanorod using phosphogypsum waste and potassium dihydrogen phosphate under the hydrothermal method. The influence of temperature, synthesis time and pH was investigated. Also, the effect of Brij-93 surfactant on the morphology of the developed hydroxyapatite was evaluated. The phase pure hydroxyapatite nanorod with a diameter of 18 nm and length of 63 nm was obtained at an optimal temperature of  $200^\circ\text{C}$  with a pH of 11 and the surfactant concentration was maintained to 0.01 mol (Bensalah et al. 2018). Amirthalingam et al. 2019 prepared hydroxyapatite using dolomite as a calcium source by the mechanochemical method.

The results reported that the pure hydroxyapatite phase was obtained at 950 °C and as temperature increases above the value calcium phosphate phase overcome the hydroxyapatite phase (Amirthalingam et al. 2019).

Some researchers have reported that a trace of fluoride in hydroxyapatite decreases solubility and makes it more antimicrobial for specific microbes. Also, it stimulates MG 63 osteoblast-like-cell proliferation and alkaline phosphate activity. Ge et al. 2019 investigated surfactant-free one-dimensional fluoridated hydroxyapatite nanorod. The rods are having a diameter of 28-211 nm and 124-2012 nm in length were developed using an electrochemical method (Ge et al. 2019). The *in vivo* results confirms that these fluoridated hydroxyapatite nanorods are the promised biomaterial for the next generation biomedical application. Dab et al. 2018 investigated the method for synthesizing hydroxyapatite from *Labeo rohita* fish for bone tissue scaffold. The thermogravimetric analysis confirms the developed hydroxyapatite is highly stable up to 800 °C. The developed scaffolds show porous morphology with interconnected porosity which is essentially needed for the bone tissue scaffold (Deb et al. 2019).

Few authors have reported that, due to the highly stable phase, the antimicrobial property of hydroxyapatite is very weak. Therefore, doping of a few nanomaterials is the way to alter the antimicrobial characteristics of the scaffold material. Silver nanomaterials are being a good record of their antimicrobial property. Doping of silver nanomaterial is the best way to tailor the antimicrobial property of hydroxyapatite scaffold. The silver doped hydroxyapatite synthesized by precipitation method sintered at 900 °C shows a well-crystallized structure with superior antimicrobial activity against *staphylococcus aureus* bacteria (Riaz et al. 2018). Similar work was carried out by Wang et al. 2018. The incorporation of silver nanoparticles effectively enhances the antimicrobial property similar to the previous report. The silver ions have a broad spectrum of antimicrobial activity against gram-positive bacteria. However, it is still a controversial issue since the increased concentration may be toxic to mammalian cells (Wang et al. 2018).

## CHAPTER 3

### MATERIALS AND METHODS

---

#### 3.1 Materials used for composites

Cuttlefish bones were collected from the National Institute of Technology Surathkal, Beach (13.0060° N, 74.7897° E), Mangalore, India. Analytical grade orthophosphoric acid (H<sub>3</sub>PO<sub>4</sub>) was procured from Merck, India. Low molecular weight Chitosan (CS, the degree of deacetylation  $\geq 75\%$ ) and TiO<sub>2</sub> nanoparticles were procured from Sigma-Aldrich, India. Polyvinyl alcohol with an average molecular weight of 160,000 Da (86.5-89 % degree of hydrolysis) was purchased from Himedia Laboratories Mumbai, India. Glutaraldehyde (~25% aqueous solution) was procured from Spectrochem, India. Bacterial strains *Escherichia coli* (*E. Coli*), *Staphylococcus aureus* (*S. aureus*) pathogen and *Candida albicans* (*C. albicans*) fungi were procured from the Institute of Microbial Technology, Chandigarh, India and Vallabhbhai Patel Chest Institute, Delhi, India respectively. Mammalian L929 and MG63 normal mouse fibroblast and osteoblast like-cell lines were supplied by National Centre for Cell Science (NCCS) Pune, India. Dulbecco's Modified Eagle's Medium (DMEM), Fetal Bovine Serum (FBS), Phytohaemagglutinin (PHA) and MTT reagents were procured from Himedia Laboratories Mumbai, India. Cell freezer Dimethyl sulfoxide (DMSO) was supplied by Sigma Aldrich, India. All other chemicals and solvents were of analytical or pharmaceutical grade and used as received.

#### 3.2 Synthesis of hydroxyapatite and tricalcium phosphate from cuttlefish bone

For hydroxyapatite (HAp) synthesis, cuttlefish bones (CB) were boiled in water for 2 h to remove the fleshy material and then dried in an incubator (Rotek, India) at 70 °C for 24 h. The sterile bones were then pulverized and sieved in a sieve shaker. 2 g of CB powder was suspended in 100 mL of demineralized water under intense magnetic stirring (10 min, 450 rpm) at 70 °C followed by adding 550  $\mu$ L Orthophosphoric acid (H<sub>3</sub>PO<sub>4</sub>) to maintain a stoichiometric molar ratio of 1.667 (Ca/P). Stirring was continued for another 10 h and the slurry thus obtained was dried and calcined in a muffle furnace at 800 °C with a heating rate of 5 °C/min for 4 h.

Similarly, for tricalcium phosphate (TCP) synthesis, 2 g of cuttlebone powder was calcined at 800 °C for 2 h. Then, the powder was suspended in 100 mL of

demineralized water under intense magnetic stirring (10 min, 450 rpm) at 70 °C. Hydrating agent Orthophosphoric acid was added (1.2 mL) slowly dropwise manner to maintain a stoichiometric molar ratio of 1.5 (Ca/P) and stirring was continued for another 8 h. The obtained slurry was dried and calcined in a muffle furnace at 1100 °C with a heating rate of 5 °C/min for 1 h.

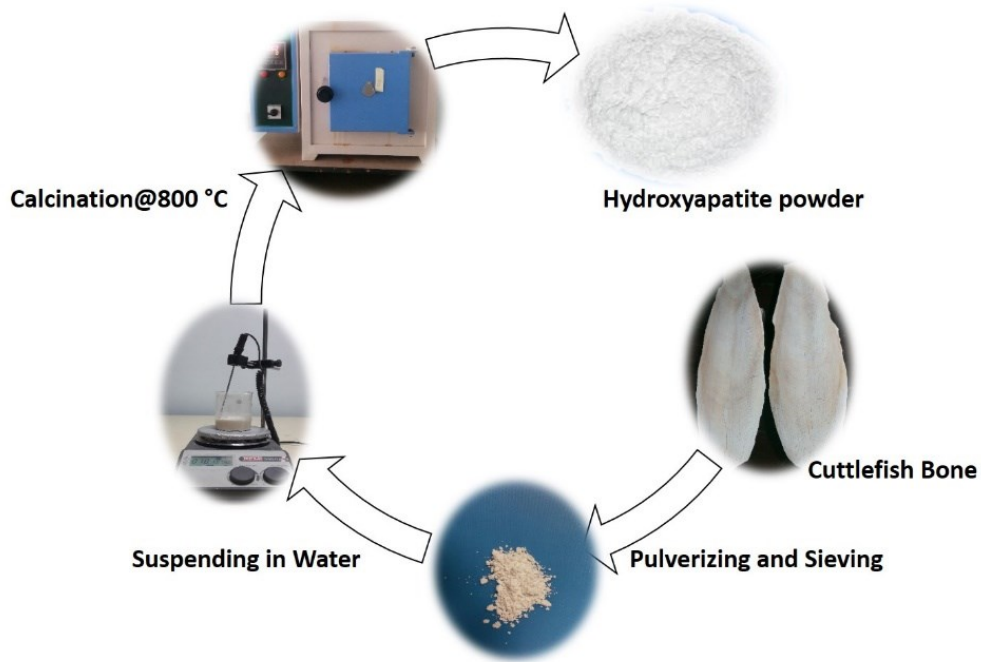


**Fig. 3.1** Schematic representation hydroxyapatite synthesis

### 3.3 Characterization of hydroxyapatite

Crystallinity and phase composition of the synthesized material was determined by an X-ray diffractometer (Rigaku, MiniFlex 600) in the range 20-60 ° at a rate of 2 %/min. The crystallinity of the HAp was calculated by using equation

$$X_c = 1 - \left[ \frac{V_{112/300}}{I_{300}} \right] \dots\dots\dots(3.1)$$

Where  $I_{300}$  is the intensity of the (300) reflection and  $V_{112/300}$  is the intensity of the valley between (112) and (300) diffraction peaks. Meanwhile, the mean crystallite size of the sample was evaluated by using the Scherrer equation as follows:

$$D_{hkl} = \frac{k \lambda}{\beta \cos\theta - 2 \varepsilon \sin\theta} \dots\dots\dots(3.2)$$

Where D is the crystallite size, hkl is the miller indices, k is the shape factor or broadening constant taken as 0.94,  $\lambda$  is the wavelength of the Cu K $\alpha$  radiation ( $\lambda=0.15418$  nm), and  $\beta$  is the full width at half maximum for the diffraction peak (radians),  $\theta$  is the diffraction angle,  $\epsilon$  is the microstrain (Chen et al. 2019). The structural parameters of the hydroxyapatite were calculated is as follows:

$$\frac{1}{d^2} = \frac{4}{3} \left[ \frac{h^2 + hk + k^2}{a^2} \right] + \frac{l^2}{c^2} \dots\dots\dots(3.3)$$

$$\epsilon = \frac{\lambda}{D_{hkl} \sin\theta} - \frac{\beta}{\tan\theta} \dots\dots\dots(3.4)$$

$$v = a^2 c \sin 60^\circ \dots\dots\dots(3.5)$$

Where ‘d’ is the d-spacing, ‘a’ and ‘c’ are the lattice constants,  $\delta$  is the dislocation density and v is the volume of the unit cell. Field Emission Scanning electron microscopy, FESEM (ZEISS SIGMA, German), was used to analyze the morphology of the developed HAp. Before the test, samples were sputter-coated with a gold layer of about 100 Å to avoid the charging effect.

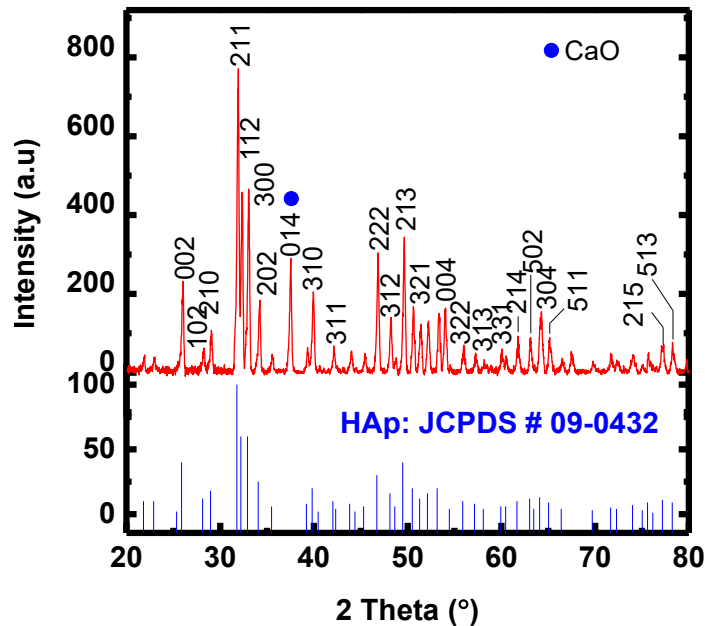


**Fig. 3.2** X-ray Diffractogram of Synthesised Hydroxyapatite.

The average diameter and length of HAp nanorod were determined by the JAVA based image processing program ImageJ. The functional groups of the developed nanomaterial were identified by Attenuated Total Reflectance Fourier

Transform Infrared (ATR-FTIR) spectroscopy from the Bruker alpha instrument at an operating wavelength range of 4000-500  $\text{cm}^{-1}$  with a resolution of 8  $\text{cm}^{-1}$ .

**Table 3.1** Cell parameters of synthesized hydroxyapatite

Sample	2 $\theta$	(hkl)	FWHM ( $\text{A}^\circ$ )	d-spacing ( $\text{A}^\circ$ )	Crystallinity (%)	Crystallite size (nm)
HAp	25.92	002	0.42612	3.44	82.72	19.13
	31.94	211	0.73204	2.814		11.29
	32.38	112	0.43818	2.778		18.80
	33.1	300	0.43818	2.72		19.89
	34.24	202	0.41781	2.631		20.12
	39.96	310	0.47388	2.262		17.21
	46.84	222	0.41778	1.943		20.72
	48.18	312	0.43999	1.89		21.75
	49.48	213	0.41169	1.841		19.78
	50.62	321	0.38526	1.806		22.80
	51.32	410	0.37419	1.78		23.55
	52.22	402	0.37455	1.754		21.83
	53.32	004	0.4072	1.722		20.83
	61.78	214	0.37039	1.503		22.19
	63.12	502	0.40549	1.474		23.51
64.16	304	0.45903	1.452	22.10		

The thermal stability of the developed nanorod was studied by differential thermal analysis (DTA), Derivative Thermogravimetry (DTG) and Thermogravimetric analysis (TGA) using EXSTAR 6000 TG/DTA 6300-Japan in the range 25-900  $^\circ\text{C}$  at a rate of 10  $^\circ\text{C}/\text{min}$  in nitrogen environment with a flow rate of 50 mL/min. The X-ray diffraction pattern of the synthesized hydroxyapatite [ $\text{Ca}_5(\text{PO}_4)_3(\text{OH})$ ] is as shown in Fig. 3.2 with crystal plane miller indices. The characteristic peaks of hydroxyapatite are confirmed with JCPDS card no: 09-432 (space group: P63/m, crystal system: hexagonal, Z: 2,  $a=b=9.418 \text{ \AA}$ ,  $c=6.884 \text{ \AA}$ ,  $\alpha=\beta=90^\circ$ ,  $\gamma=120^\circ$ ). The unit cell volume of HAp is 52.88 nm and exhibits a lower micro-strain of 0.00245. The peaks are markedly broader and well separated confirms that the particles are in nanosize. The presence of

major intensity and well-resolved distinct peaks in the range  $2\theta=20-35^\circ$  confirms good crystallinity with the fine grain size of hydroxyapatite. Besides, there could be a retained certain amount of CaO confirmed with JCPDS card no: 37-1497. Table 3.1 summarizes the crystallinity, crystallite size, cell parameters of synthesized hydroxyapatite. The FESEM images of HAp (Fig. 3.3) confirm the rod-shaped morphology appeared as numerous arrangements of uniform bundles of one-dimensional nanorod structure with an average size of  $186\pm 12$  nm in diameter and 1-1.2  $\mu\text{m}$  in length.

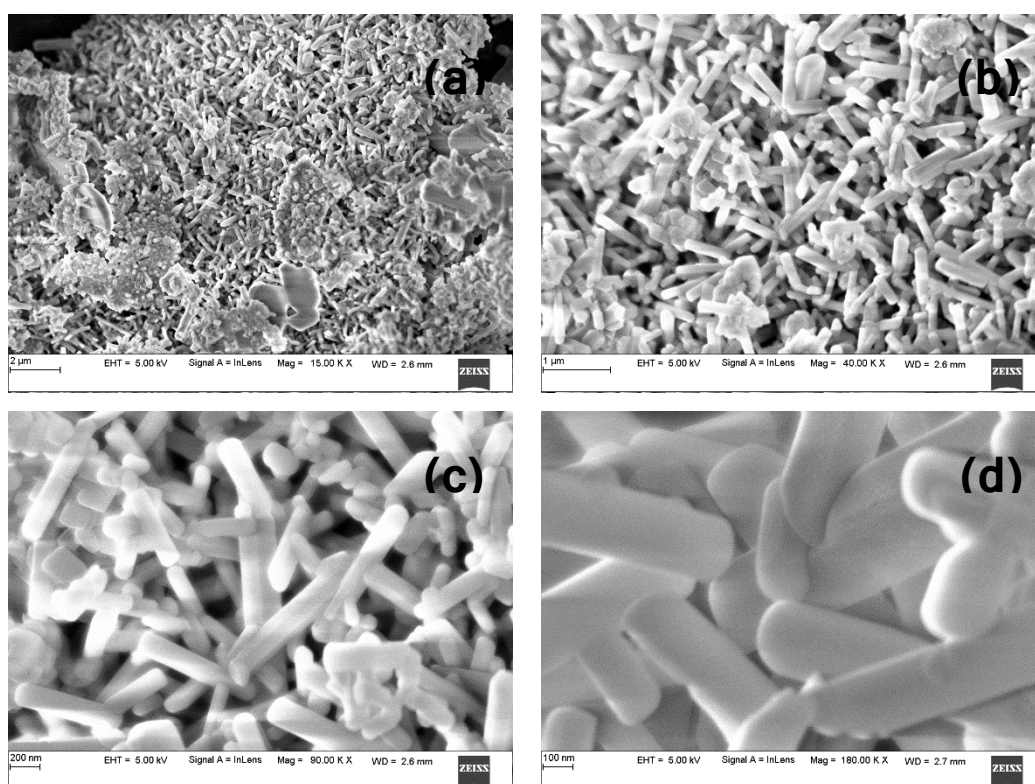


**Fig. 3.3** FESEM images of hydroxyapatite with various magnification (a) 2  $\mu\text{m}$ , (b) 1  $\mu\text{m}$ , (c) 200 nm and (d) 100 nm.

The FT IR spectrum of cuttlebone, hydroxyapatite and  $\beta$ -tricalcium phosphate were recorded in the range  $4000-500\text{ cm}^{-1}$  (Fig. 3.4). For cuttlebone, intense aragonite peaks at  $1081\text{ cm}^{-1}$ ,  $572\text{ cm}^{-1}$  and  $721\text{ cm}^{-1}$  were recorded due to the vibration mode of  $\text{CO}_3^{2-}$ . Besides, the presence of organic compounds like chitin and protein were confirmed by band characteristics in the region  $1470\text{ cm}^{-1}$  (amide band for protein),  $1649\text{ cm}^{-1}$  and  $1786\text{ cm}^{-1}$  (amide II) (Nasker et al. 2018). For hydroxyapatite, the absorption bands in the range  $700\text{ cm}^{-1}$  and  $568\text{ cm}^{-1}$  are attributed to the stretching of P-O bonds. An intense band at  $962\text{ cm}^{-1}$  is due to symmetric stretching and the bands at



1095  $\text{cm}^{-1}$  and 1027  $\text{cm}^{-1}$  are the asymmetric stretching modes of  $\text{PO}_4^{3-}$  ions of HAp lattice. The peak at 876  $\text{cm}^{-1}$  and band in the range 1500-1400  $\text{cm}^{-1}$  corresponding to vibration mode and stretching vibration of a carbonated group ( $\text{CO}_3^{2-}$ ) (Sabu et al. 2019).

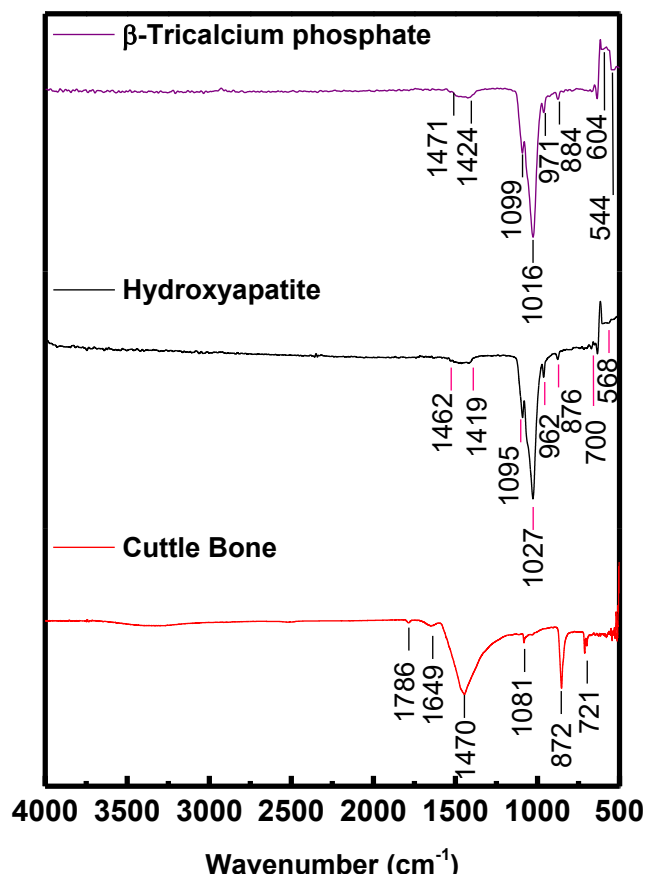


**Fig. 3.4** FT IR spectra of (a) Cuttlebone, (b) HAp and (c)  $\beta$ -TCP

### 3.4 Characterization of Tricalcium phosphate

The quantitative XRD pattern of synthesized TCP ( $\text{Ca}_3(\text{PO}_4)_2$ ) is presented in Fig. 3.5. By comparison with the JCPDS card no: 09-0169, standard data of TCP, no other significant peaks were found, indicating that the synthesized TCP has a pure phase. The synthesized TCP has a rhombohedral crystal structure with an R-3c space group ( $a=b=10.429 \text{ \AA}$ ,  $c=37.38 \text{ \AA}$ ,  $\alpha=\beta=90^\circ$ ,  $\gamma=120^\circ$ ). The three main peaks at  $2\theta$  angle 27.81, 31.15 and 34.35 are in good agreement with the predicted main peaks of TCP. The diffraction peaks corresponding to (214) (0210) and (220) are intense and narrow confirms that the sample is well crystallized with fine grain structure. The developed sample shows 78.2 % crystallinity with an average crystallite size of 26.2 nm.

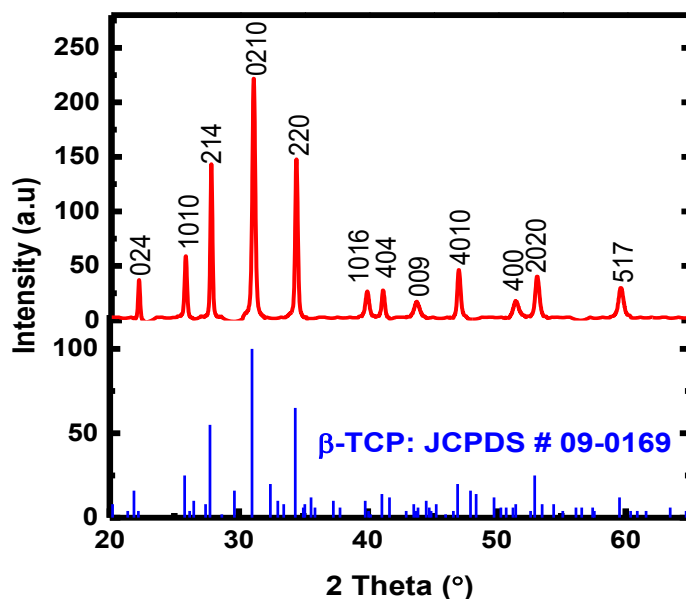


**Fig. 3.5** XRD pattern of synthesized calcium phosphate

The morphology of the TCP sample is as shown in Fig. 3.6. The calcined TCP shows a rod-shaped morphology with a one-dimensional nanorod structure with an average size of  $117 \pm 12$  nm in diameter and 700-850 nm in length.

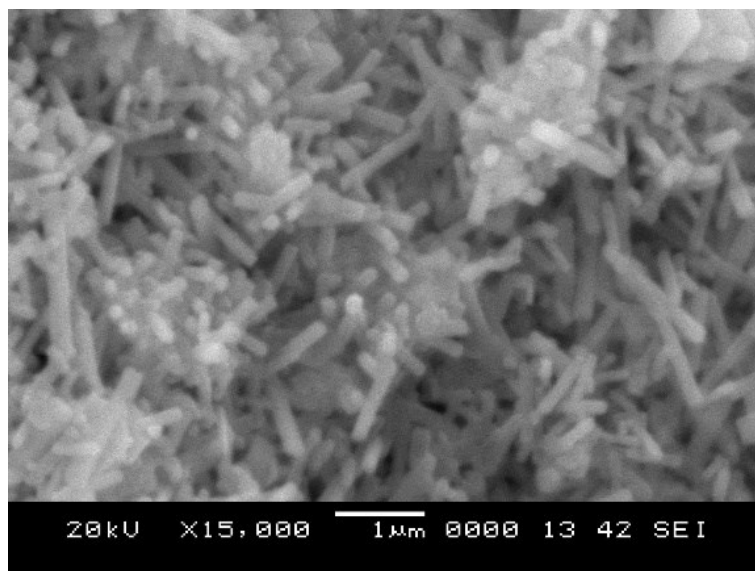


**Fig. 3.6** SEM images of calcium phosphate

The IR analysis of  $\beta$ -TCP is as shown in Fig. 3.4. The peaks at  $1016 \text{ cm}^{-1}$  and  $1099 \text{ cm}^{-1}$  corresponded to the asymmetric stretching vibration of  $\text{PO}_4^{3-}$  and  $971 \text{ cm}^{-1}$  was assigned to the symmetric stretching vibration of  $\text{PO}_4^{3-}$ . The absorption bands in the range of  $600\text{-}550 \text{ cm}^{-1}$  are attributed to the stretching of P-O bonds. The peak at  $884$

$\text{cm}^{-1}$  and band in the range  $1480\text{-}1410\text{ cm}^{-1}$  corresponding to vibration mode and stretching vibration of the carbonated group ( $\text{CO}_3^{2-}$ ) (Liu et al. 2018).

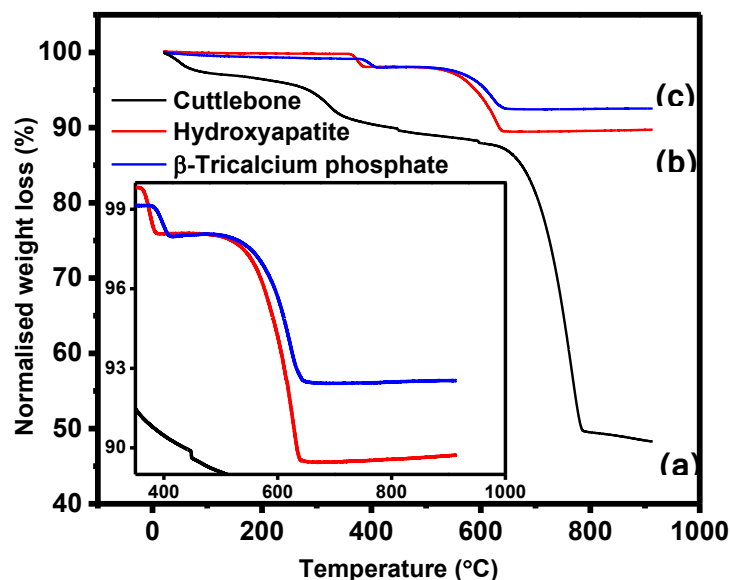


**Fig. 3.7** Thermogravimetric analysis of (a) Cuttlebone, (b) Hydroxyapatite and (c)  $\beta$ -Tricalcium phosphate

The thermal degradation behavior of the cuttlebone, hydroxyapatite and  $\beta$ -Tricalcium phosphate are as shown in Fig. 3.7. The TGA of cuttlebone exhibit 3 stages of degradation; first, 2% of degradation occurred at  $30\text{-}75^\circ\text{C}$  due to the moisture content in the sample. The second major degradation occurred in the range of  $300\text{-}380^\circ\text{C}$  confirms the decomposition of the organic compounds of the bone constituents. During this stage around 7.5% of weight loss was observed. The third stage of degradation started at  $640^\circ\text{C}$  and is continued up to  $780^\circ\text{C}$ . The TGA curves showed a maximum degradation of 38% in the region. It could be due to the decomposition of calcium carbonate ( $\text{CaCO}_3$ ) into calcium oxide ( $\text{CaO}$ ) and carbon dioxide ( $\text{CO}_2$ ) (Periasamy and Mohankumar 2015). However, for HAp and  $\beta$ -TCP degradation was observed only in two stages. The first minor weight loss was observed at  $380\text{-}410^\circ\text{C}$  (degradation of tightly attached organic matter) and major degradation was found in the range  $550\text{-}640^\circ\text{C}$ .

### 3.5 Synthesis of Titanium Dioxide Nanotube (TNT)

TNT's from  $\text{TiO}_2$  nanoparticles were prepared as explained in the article (Kumar et al. 2013). In brief, 50 mL of 10M NaOH solution was prepared in a round bottom flask and is coupled to a condenser with the chilling unit. The blend was heated

to 120 °C, followed by the addition of 2 g of TiO<sub>2</sub> nanoparticles. The solution was then refluxed for 48 h at 120 °C with constant stirring. Then, the mortar was cooled to room temperature and slowly poured into a 500 mL beaker containing de-ionized water. In the end, whitish nanotubes are settled at the bottom of the beaker. The topwater was decanted, and cleaning was repeated five times. Thereafter, 150 mL of 0.1M HCl was added to the slurry and stirring was continued for another 10 h at 60 °C. The developed nanotubes were again flushed several times with demineralized water until the neutral pH was obtained. Finally, the solution was centrifuged and obtained nanotubes were calcined at 450° C for 4 h. The transmission electron microscope images of synthesized titanium dioxide nanotubes are as shown in Fig. 3.8. The Synthesized TNT's had one-dimensional nanotube morphology with an average of 7.2±0.9 nm in diameter and 76±6.6 nm in length.

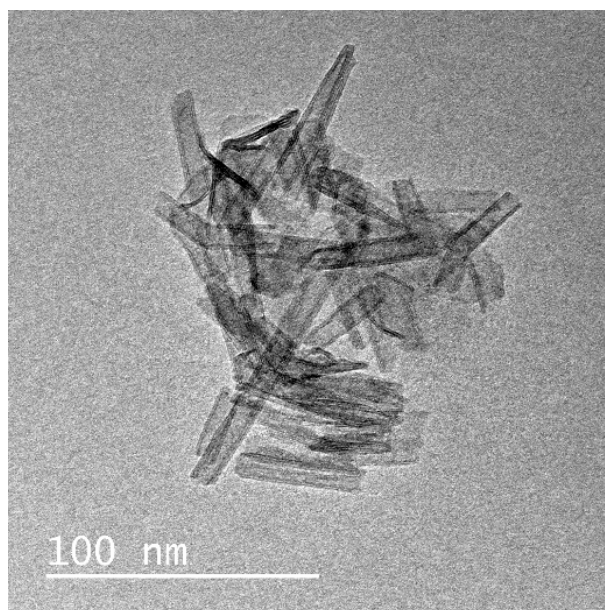


**Fig. 3.8** TEM image of synthesized TNT



## CHAPTER 4

### INFLUENCE OF BIO CERAMICS ON CHITOSAN COMPOSITE HYDROGEL FOR CARTILAGE REGENERATION

---

This chapter describes the influence of bioceramic reinforcements such as hydroxyapatite nanorod (HANr), biphasic calcium phosphate (BCP) and Titanium Dioxide Nanotube (TNT) on the physical and mechanobiological properties of chitosan hydrogel for cartilage regeneration application. The HANr and BCP were synthesized from biowaste cuttlefish bone as explained in the previous chapter. The TNT's were developed using titanium dioxide nanoparticles. The chitosan composite hydrogels were developed through the freeze-gelation method. Then the samples were characterized by Scanning Electron Microscope (SEM) and Fourier Transform Infrared Spectroscopy (FTIR). The physical, mechanical, rheological and biological properties were analyzed. The bioceramic reinforced chitosan composite hydrogels show favourable material properties for cartilage tissue regeneration application.

#### 4.1 Materials used for composites

Low molecular weight Chitosan (CS, the degree of deacetylation  $\geq 75\%$ ) was purchased from Sigma-Aldrich, India. Glutaraldehyde (~25% aqueous solution) was procured from Spectrochem, India. Bacterial strains *Escherichia coli*, *Staphylococcus aureus* and *Candida albicans* fungi were procured from the Institute of Microbial Technology (IMTECH), Chandigarh, India. L929 and MG 63 cell lines were procured from National Centre for Cell Science (NCCS) Pune, India. Dulbecco's Modified Eagle's Medium (DMEM), Fetal Bovine Serum (FBS), Phytohaemagglutinin (PHA) and MTT reagents were procured from Himedia Laboratories Mumbai, India. Cell freezer Dimethyl sulfoxide (DMSO) was supplied by Sigma Aldrich, India. All other chemicals and solvents were of analytical or pharmaceutical grade and used as received.

#### 4.2 Preparation of CS/HANr, CS/BCP and CS/TNT composite hydrogel

The chitosan (CS) composite hydrogel was prepared by dissolving 1g of CS in a 0.1 M aqueous acetic acid solution. Meanwhile, different concentrations of reinforcements were suspended in 50 mL demineralized water for 1 h using a probe sonicator. The suspension was then slowly added to the CS solution and is diluted with

demineralized water to a final volume of 100 mL under intense magnetic stirring (10 h, 400 rpm). The crosslinking agent glutaraldehyde (0.5 % v/v) was added in a dropwise manner with constant stirring and the solution mixture was poured into a silicone mould. After 10 h, samples were removed from the mould and washed several times with 70% ethanol until neutral pH was obtained. Finally, samples were washed with sterile water and stored at 20 °C in the demineralized for further characterization. Fig. 4.1 shows a schematic representation of chitosan composite hydrogel preparation.

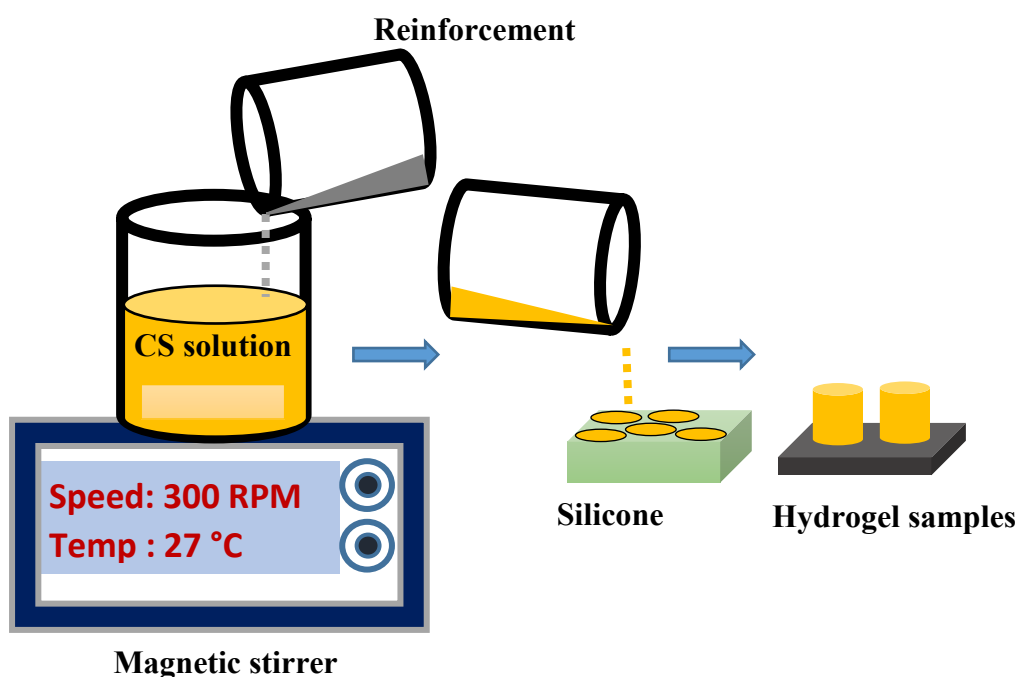


**Fig. 4.1** Schematic representation of Chitosan composite hydrogel preparation

### 4.3 Characterization of composite hydrogel

For morphological analysis and pore size scanning electron micrographs, SEM (JSM-6380LA, JOEL, Japan) is used. The average pore size was determined by the JAVA based image processing program ImageJ for scaffold imaging. The structural modification of composite hydrogel due to the introduction of bioceramic reinforcement was identified by attenuated total reflectance Fourier Transform Infrared Spectroscopy (ATR-FTIR) from the Bruker alpha instrument at an operating wavelength range of 4000-500  $\text{cm}^{-1}$ .

#### 4.3.1 Physical tests

For swelling studies, cylindrical CS and composite hydrogels (10 mm diameter and 5 mm height) were lyophilized and initial weight was measured ( $W_i$ ). Then the samples were incubated in distilled water at 37 °C until no change in mass was observed. Now the samples were removed from the medium and wiped with the tissue paper and measure the final weight ( $W_f$ ). The swelling ratio is defined as the ratio of swollen weight to initial weight was measured from Equation (4.1).

$$\text{Swelling ratio} = \frac{W_f}{W_i} \times 100 \dots\dots\dots (4.1)$$

The wettability of the scaffold was measured by assessing the angle formed between a drop of fluid (Phosphate Buffer Saline, PBS at 7.2 pH) and the sample surface. The hydrogel films of 0.5 mm thick were cast on the glass substrate and the contact angle was determined using the Drop shape analyzer (Kruss, Germany). The porosity of the hydrogel was determined by the liquid displacement method. The fully crosslinked cylindrical samples (10 mm diameter and 10 mm height) were immersed in 100 mL ethanol until no change in mass was observed. Then the samples were removed from the medium and measured the final weight ( $W_2$ ). Finally, samples were lyophilized and measured the dry weight ( $W_1$ ). The porosity was calculated as;

$$\text{Porosity} = \frac{(W_2 - W_1 - W_3)}{(W_2 - W_3)} \times 100 \dots\dots\dots (4.2)$$

Where  $W_3$  is the weight of the ethanol after removal of the hydrogel sample.

#### 4.3.2 Mechanical tests

The unconfined compression and cyclic loading-unloading compression test was performed in the universal testing machine (Mecmesin MultiTest 10-i micro UTM, London) with a 1000 N load cell. The cylindrical samples of 10 mm diameter and 7 mm height were used with a crosshead speed of 5 mm/min for unconfined compression tests and 20 mm/min cyclic loading-unloading compression tests. Before the test, a preload of 0.01 N was applied to confirm the clear contact between the compression plates and the hydrogel. The force and deformation data were used and the Stress vs Strain graph was plotted. The Elastic modulus ( $E$ ), Stress-at-break ( $\sigma_{\max}$ ) and Strain-at-break ( $\epsilon_{\max}$ ) were determined from the curves.



### 4.3.3 Rheological Test

The rheological behaviour of composite samples was performed at 37 °C in an MCR 302 Anton Paar Rheometer. The tests were carried out in a parallel plate mode with a disc-shaped sample of 25 mm diameter and 2 mm thickness. An oscillatory frequency sweep test was carried out in the frequency range of 0.1-100 Hz with 1% constant strain. The components of complex modulus such as storage modulus (G') and loss modulus (G'') were investigated.

## 4.4 Biological Characterization

### 4.4.1 Degradation studies

*In vitro* biodegradation of hydrogel composites was investigated using 0.1 M phosphate buffer saline (pH 7.2) with lysozyme enzyme (0.5 mg/mL). The hydrogel discs (5 mm diameter and 2 mm height) were immersed in 50 mL centrifuge tubes and kept oscillating at 37.0±0.5 °C. After 30 days of incubation, samples were removed and wiped with absorbent paper and measured weight (Pallela et al., 2012). The weight loss of the hydrogel sample was calculated as;

$$W_L = \frac{(W_i - W_f)}{W_i} \times 100 \dots\dots\dots(4.3)$$

Where  $W_i$  and  $W_f$  are the weight of the hydrogel before and after soaking respectively.

### 4.4.2 Growth inhibition test

The antimicrobial activity of the composite hydrogel was evaluated according to the growth inhibition assay using the modified method explained elsewhere (Wei et al. 2016). In brief, 150 µL of nutrient broth and 50 µL of diluted bacterial or fungal culture were taken in a 96 well culture plate. The initial absorbance at 600 nm was measured in a Thermo scientific Multiscan® plate reader and considered as initial bacterial/fungal concentration. Then, 10 mg of triplicate hydrogel samples were added to the respective well and incubated overnight at 37 °C. The inoculum was then monitored for changes in the absorbance at 600 nm (OD<sub>600</sub>). The well without any sample was considered as a control. The percentage growth compared to the control was calculated for each of the samples.

#### 4.4.3 Measurement of cytotoxicity

The cytocompatibility of the hydrogel was assessed by determining the viability of the L929 mouse fibroblast and MG 63 osteoblast-like cells in response to the conditioned media using MTT assay. Briefly, hydrogel discs (10 mm diameter, 2 mm thick) were sterilized in 70% ethanol followed by washing in a sterile PBS. Cells were seeded on the hydrogel surface (50,000 cells/well) in a 24-well plate with DMEM supplemented with 10% FBS and incubated at 37 °C for 72 h in 5% CO<sub>2</sub>. Then, the media was replaced with MTT to a final concentration of 5 mg/mL and incubated for another 3 h. Finally, 100 µL of DMSO was added with gentle stirring in a gyratory shaker. The medium without any treatment was considered as control (100%) and cell activator Phytohaemagglutinin (PHA) treated hydrogel was considered as standard (Le et al. 2018) (Jaiswal 2010). The optical density (OD) of the media was measured at 570 nm to determine the cell viability, according to the equation:

$$\text{Cell viability (\%)} = \frac{\text{OD}_{\text{test}} - \text{OD}_{\text{blank}}}{\text{OD}_{\text{control}} - \text{OD}_{\text{blank}}} \dots\dots\dots(4.4)$$

Where, OD<sub>test</sub>, OD<sub>control</sub> and OD<sub>blank</sub> are the optical densities of cells incubated with hydrogel, DMEM with cells and DMEM without cells respectively.

#### 4.4.4 Statistics

All quantitative results were obtained from triplicate samples and data were shown as a mean ± standard deviation. Statistical significance is calculated using the one-way ANOVA test. A value of p < 0.05 was considered statistically significant.

### 4.5 Results and Discussion

The photograph of the developed hydrogel is as shown in Fig. 4.2. It has been observed that a pure CS hydrogel is a yellowish, glowing and semi-transparent nature. Whereas the addition of the bioceramic reinforcement relatively turns the gel into pale yellow and opaque.

The internal morphology of the lyophilized transversely sectioned hydrogels is as shown in Fig. 4.3. All the hydrogels show the porous microstructure with interconnected porosity which is significantly important for the cartilage scaffolds to transfer nutrients and metabolic wastes in the biological environment. The average pore

size and porosity of the chitosan and its composite hydrogels are summarised in Table 4.1. The introduction of bioceramic reinforcement reduces the porosity without affecting the organised porous network.

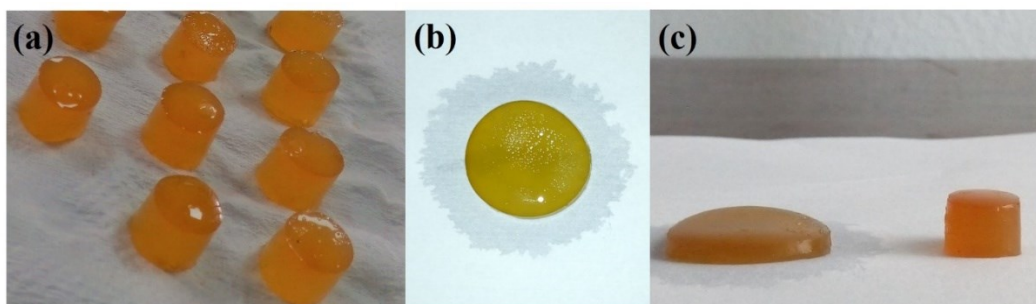


**Fig. 4.2** Photographs of the hydrogel (a-b) Chitosan and (c) Chitosan composite hydrogel

The tiny micro and nanopores do not affect the mechanical properties instead, they disburse load more evenly and act as a barrier for crack propagation, which increases the fatigue strength. Further, it lowers the permeability and hence more barrier to fluid flow and thus increases the fluid load support (Han et al. 2017).

The structural modification in the composite hydrogel due to the admittance of the reinforcement was identified by the FTIR spectrum (Fig. 4.4). The broad spectral band in the region  $3016\text{-}3629\text{ cm}^{-1}$  corresponds to the characteristic peak of CS due to O-H stretch overlaid with N-H stretch, Aliphatic C-H stretch at  $2927\text{ cm}^{-1}$  consisting with existing literature. A spectrum at  $1636\text{ cm}^{-1}$  region is owing to the C=N bond of Schiff base due to the interaction of free amine groups of CS and aldehyde functionality. In CS/1.5 HANr and CS/3BCP composite hydrogel a small peak at  $1026\text{ cm}^{-1}$  and  $1023\text{ cm}^{-1}$  respectively corresponds to the asymmetric stretched phosphate band of nanohydroxyapatite and tricalcium phosphate. In composites, a slight shift of the C=N bond and hydroxyl group towards the lower wavenumber signifies the formation of hydrogen bonding between CS and bioceramic reinforcement. For CS/2TNT composites, the peak at  $1511\text{ cm}^{-1}$  corresponds to the N-H bend,  $1648\text{ cm}^{-1}$  related to the C-O stretch. The peaks in the region  $1020\text{ cm}^{-1}$  to  $1056\text{ cm}^{-1}$  signifies the bending vibrations of Ti-O-C and stretching vibration of C-O-C respectively. The stretching vibration in the region  $770\text{-}700\text{ cm}^{-1}$  is ascribed to the signal of the Ti-O-Ti bond.

Swelling and water holding potency is the ability of cartilage scaffold significantly influence the lubrication and diffusion of nutrients into the perichondrium

and core of the cartilage since it does have blood vessels and a neural system. In hydrogels, the swelling is mainly related to the amorphous region and free hydroxyl (OH) groups of the polymer network. The equilibrium swelling strength of all the hydrogels is summarised in Table 4.1. As expected, neat CS hydrogel has the highest swelling strength of  $612\pm 18\%$  and decreases with the addition of reinforcement. It could be due to the reinforcement develops additional hydrogen bonds as confirmed by the FTIR spectrum, which arrests the free movement of the polymer chain. On the other hand, the introduction of bioceramic reinforcement increases the crystalline region that causes a reduction in the free hydroxyl group that essentially causes swelling.

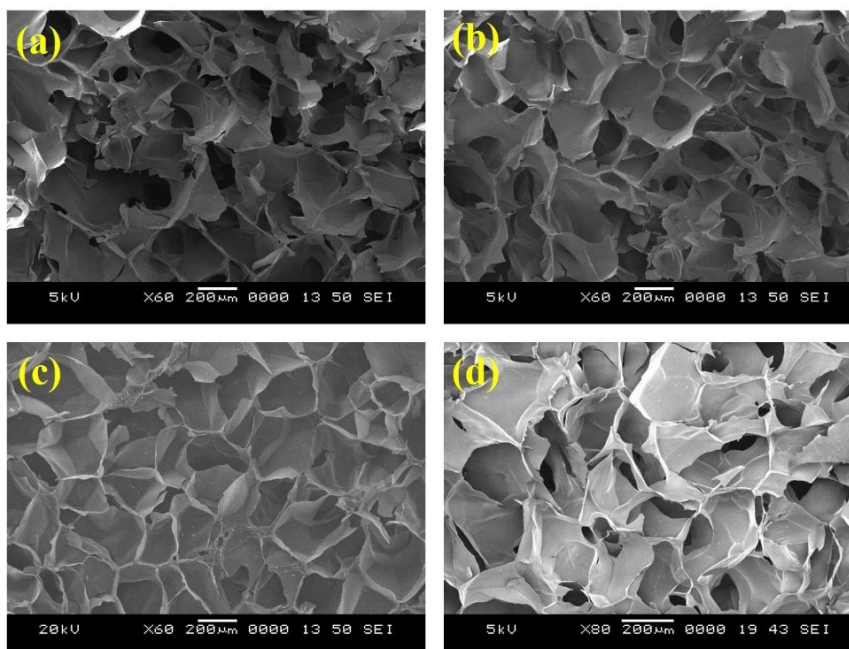


**Fig. 4.3** SEM images of hydrogel (a) CS (b) CS/1.5HANr (c) CS/3BCP and (d) CS/2TNT composite hydrogel

The swelling mechanism in hydrogels depends on many parameters such as reinforcement, processing technique, pH, etc. Delmar et al., performed swelling studies on genipin crosslinked chitosan hydrogels by varying solution pH from 3 to 14. (Delmar and Bianco-Peled 2015). From the result, it is concluded that the swelling is lowest in the neutral pH (7.4). This is because the swelling behaviour in extreme pH conditions (less than 3 and more than 10) affects the hydrolysis of amide linkage of the chitosan by acid or alkaline leads to the formation of carboxylic acid and amine groups. These reformed groups can be ionized hence enhances the swelling strength

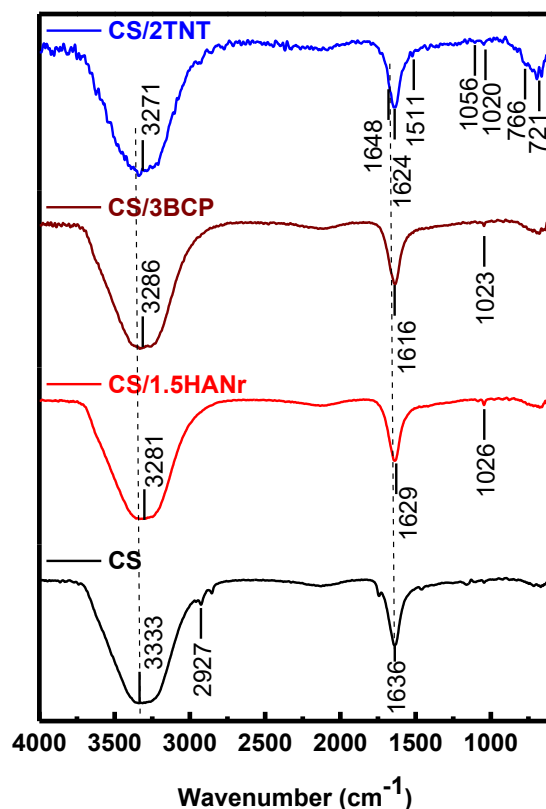


**Fig. 4.4** Fourier Transform Infrared (ATR-FTIR) Spectroscopy of CS and its composite hydrogel

. The surface wettability of the scaffold is the primary component of the biomaterial that comes in contact with the tissue, cells and body fluids. Thus, the biocompatibility of the material is primarily influenced by surface characteristics particularly surface topography, surface energy and wettability. The wettability or adsorption potency reflects the cell adhesive serum protein such as fibronectin, fibrinogen, and vitronectin adsorption and cell proliferation ability of the biomaterial scaffold. Many of the reports have revealed that the osteoblast adhesion to moderately wettable surfaces showed a linear growth of cells, whereas on the extremely hydrophobic or hydrophilic surfaces the growth of osteoblast was greatly reduced, probably due to the absence of adhesion proteins.

Oliveira et al, investigated the bacterial adhesion on wettability and the results confirm that adhesion of both gram-positive and gram-negative bacterial strains was greater for the hydrophilic surface than hydrophobic (Oliveira et al. 2018). These conflicting results on the influence of surface wettability on bacterial strain indicate that

there may be other underlying factors, such as surface roughness, that are more relevant in promoting or preventing the adhesion and colonization of microbes. For tissue-engineered cartilage, it was found that the optimum contact angle for maximum cell adhesion is in the range of 55-70°. The contact angle of all the hydrogels are summarized in Table 4.1 are lying within this range which assists the protein adhesion and cell attachment and proliferation.

**Table 4.1.** Physical properties of PVA/HANr hydrogel

Sample	Swelling Ratio (%)	Average pore size ( $\mu\text{m}$ )	Porosity (%)	Contact angle ( $^{\circ}$ )
CS	612 $\pm$ 18	156 $\pm$ 8	92.15 $\pm$ 1.73	65.5 $\pm$ 0.32
CS/1.5HANr	475 $\pm$ 17	132 $\pm$ 5	78.01 $\pm$ 0.11	63.2 $\pm$ 0.10
CS /3BCP	455 $\pm$ 11	125 $\pm$ 7	83.12 $\pm$ 1.02	62.5 $\pm$ 0.24
CS/2TNT	500 $\pm$ 13	242 $\pm$ 3	85.26 $\pm$ 0.65	62.8 $\pm$ 0.66

#### 4.5.1 Compression and cyclic loading-unloading compression test.

The mechanical characterization of nanocomposite hydrogel was clinically important to avoid the strain mismatch at the implant-tissue interface. During normal working conditions, cartilage continuously undergoes compression load rather than tensile and shear. Therefore, a compression test was performed and the unconfined compression stress-strain curves of chitosan and its composite hydrogels were plotted as shown (Fig. 4.5). The curves correspond to the behavior of non-linear and viscoelastic solids. As the chitosan hydrogel is stressed, the entangled polymer chains absorb the load and get reoriented and the interstitial fluid begins to drain out. During this, a small load is enough for significant deformation (i.e. there is no significant stress up to 15% strain). As loading continues, the reorientation tends to be uniform and friction due to interstitial fluid causes the hardening effect of the polymer, which needs an additional effort to increase the strain.

In composite hydrogels, an early rise of compressive stress in comparison with chitosan hydrogel is attributed to the reinforcement, which can develop the secondary crosslinking points which try to arrest the free movement of polymer chains and causes an increase in the compressive modulus that makes hydrogel stiff. The compressive mechanical properties of the hydrogels are summarized in Table 4.2. Chitosan hydrogel shows the least compression strength of 0.4 $\pm$ 0.07 MPa with a significant deformation

of 31.8%. However, for composites, it shows a bimodal trend i.e. the compression strength was increased up to  $1.62 \pm 0.02$  MPa for hydrogel having 1.5 wt% of HANr and as it increases above, a downturn in the compression strength was found due to the agglomeration of nanohydroxyapatite reinforcement. Similarly, the maximum compression strength of BCP (3 wt %) and TNT (2 wt %) reinforced chitosan composite hydrogel corresponds to  $1.41 \pm 0.05$  MPa and  $1.8 \pm 0.08$  MPa with a significant deformation of 38.9 % and 34.5 % of strain respectively.

The compression modulus of the samples increases with increasing concentration of reinforcement confirms the additional entanglements make hydrogel stiffer. The compression modulus of neat CS, CS/1.5HANr, CS/3BCP and CS/2TNT are  $0.2 \pm 0.01$  MPa,  $2.28 \pm 0.02$  MPa,  $2.21 \pm 0.02$  MPa and  $2.45 \pm 0.01$  MPa respectively. In all the cases, the compression modulus of the composite hydrogels was higher than those of healthy cartilage, which varies between 0.1 to 2 MPa (Gonzalez and Alvarez 2014).

**Table 4.2** Compressive mechanical properties of CS composite hydrogel

Composition	Compression strength, $\sigma$ (MPa)	Compressive Strain, $\varepsilon$ (%)	Compression Modulus, E (MPa)
CS	$0.4 \pm 0.07$	31.8	$0.2 \pm 0.01$
CS/1.5HANr	$1.62 \pm 0.02$	36.2	$2.28 \pm 0.02$
CS /3BCP	$1.41 \pm 0.05$	38.9	$2.21 \pm 0.02$
CS/2TNT	$1.84 \pm 0.08$	34.5	$2.45 \pm 0.01$

To explore the mechanism of the synergistic effect of strain rate on the viscoelastic characteristics of the hydrogel in the loading condition close to the working condition of joint cartilage, the cyclic loading-unloading compression tests were performed at a crosshead speed of 20 mm/min with a fixed strain of 25% (maximum strain induced in the joint is 20 % (Briant et al. 2015)). The basic facts about these materials are the decompression path of the curve is not following its compression path. It may be above or below depending on the strain rate. The variation in the stiffness of the hydrogels was provoked by the variation in the strain rate. This mechanism reflects the non-linearity and viscoelastic nature of the hydrogel. The cyclic loading-unloading compression curves of the HANr, BCP and TNT reinforced chitosan composite

hydrogel are as shown in Fig. 4.5 (b, d and f). The steady-state cyclic stress-strain curve obtained was characterized by the well-defined hysteresis.

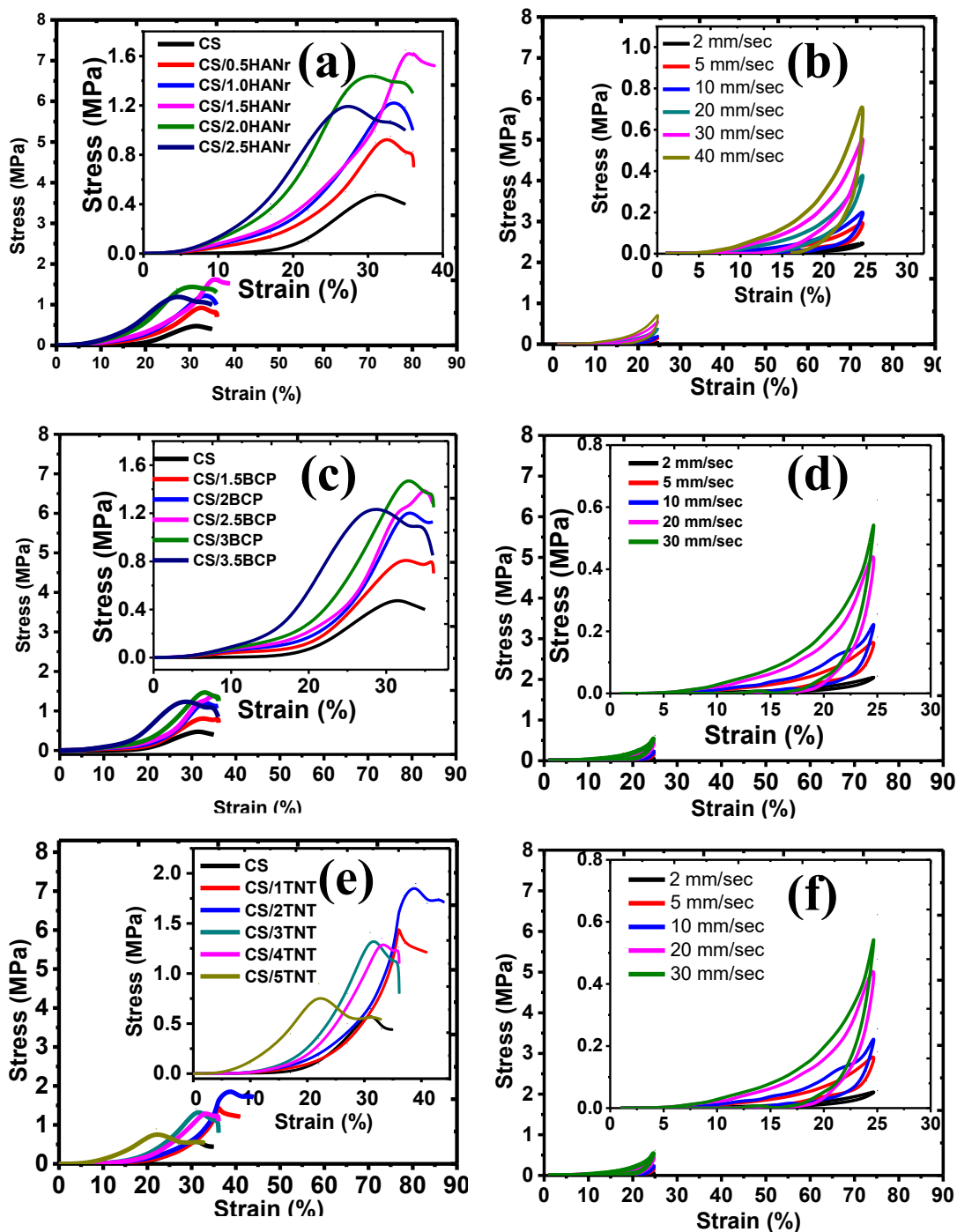


**Fig. 4.5.** Unconfined compression and cyclic loading-unloading compression test curves of (a-b) CS/1.5HANr (c-d) CS/3BCP and (e-f) CS/2TNT composite hydrogel

In all the hydrogels, for low strain rate, the narrow hysteresis loop was obtained and the loop size increases with increasing strain rate. The stress at the compression



parts of the cycle was higher than those at the decompression parts at the same strain rates. The maximum compression stress value increases from  $0.056 \pm 0.002$  MPa to  $0.72 \pm 0.002$  MPa for CS/1.5HANr composites as the strain rate increases from 2 mm/sec to 40 mm/sec.

Similarly, for CS/3BCP and CS/2TNT hydrogels, the compression strength raises from  $0.025 \pm 0.001$  MPa to  $0.512 \pm 0.01$  MPa and  $0.08 \pm 0.02$  MPa to  $0.43 \pm 0.02$  MPa as the deformation speed increases from 2 mm/sec to 30 mm/sec and 2 mm/sec to 40 mm/sec respectively. Meanwhile, the elastic modulus of the composite hydrogel also increases with strain rate. This result confirms that the developed hydrogels have sufficient stiffness and can dissipate energy by showing a larger hysteresis loop.

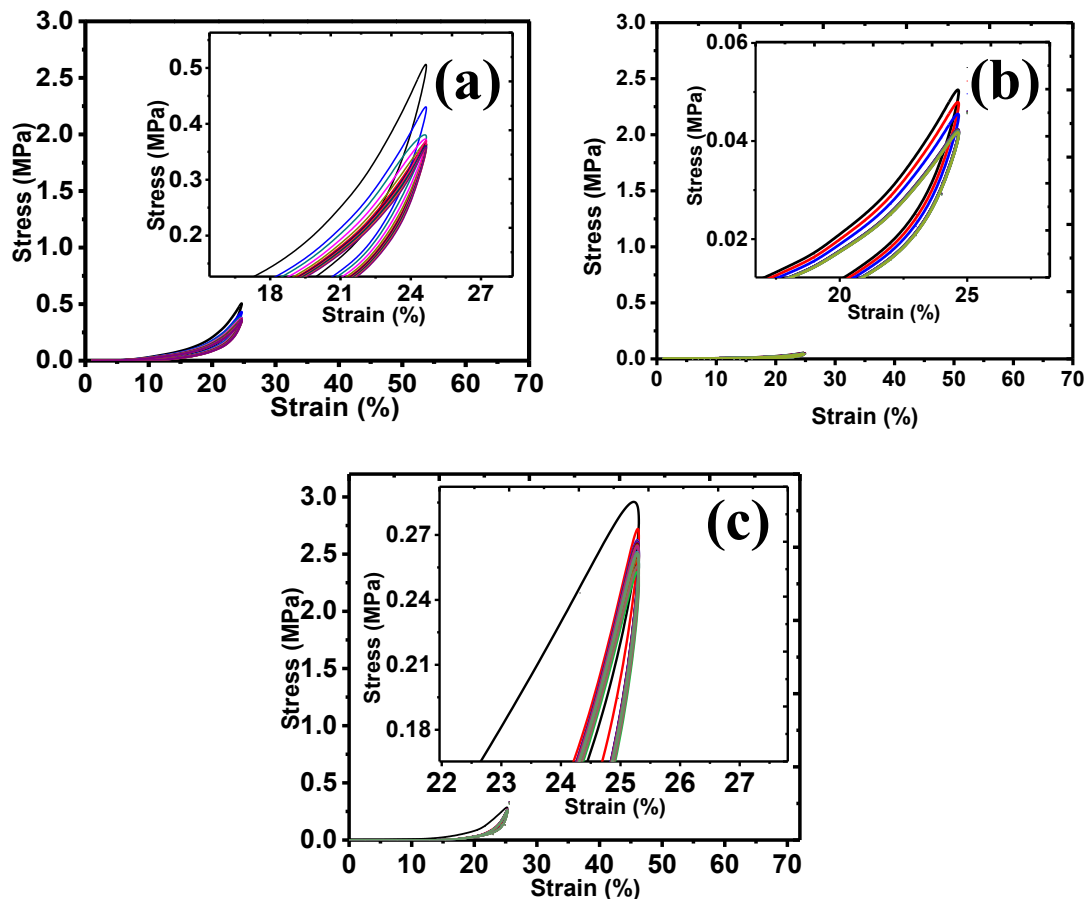


**Fig. 4.6.** The loading-unloading compression curves of (a) CS/1.5HANr, (b) CS/3BCP and (c) CS/2TNT composite hydrogel for 100 cycles

Further, to study the fatigue strength of the hydrogel, a hundred cycles of loading-unloading compression tests were performed at a rate of 20 mm/min with a constant strain of 25 %. As far as one can analyze the cyclic curves presented in Fig

4.6, in the first four-five cycles, the compression strength decreases slightly due to the damage of some chemical and hydrogen bonds that makes larger hysteresis loops. As the cycles continued, some of the hydrogen bonds were re-established, which were able to bear load in the succeeding cycles. This confirms the composite hydrogel is a better self-recoverable and fatigue resistance property.

#### 4.5.2 Rheological Studies

The Articular cartilage exhibits a time-dependent mechanical behavior under different loading conditions. These time-dependent properties such as frequency-dependent stiffening, fluid refilling and damping characteristics are essential for proper tissue functioning. The reason for this time-dependent behavior is due to the phase difference between stress input and the strain response in the viscoelastic material. For pure elastic material, the phase difference is zero. i.e., the stress and strain are in phase as shown in Fig. 4.7. For pure elastic materials, there exists a 90-degree phase difference. i.e., when stress reaches its peak, the strain just begins to respond and when stress after unloading reaches zero, the strain will reach its peak. For viscoelastic material, there is something the value is in between those two extremes.

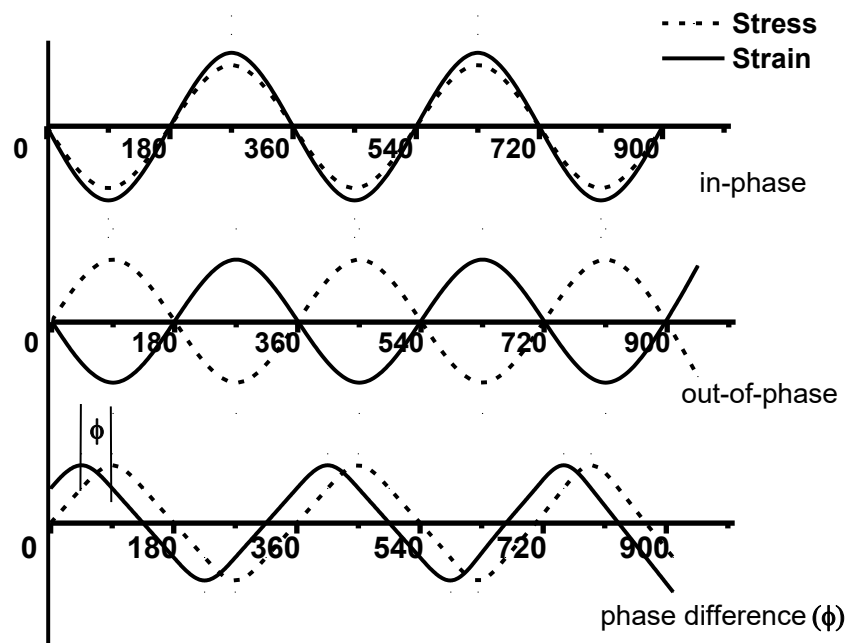


**Fig. 4.7** Cyclic stress-strain curves of viscoelastic materials as a function of time

The response of the viscoelastic material is partly viscous and partly elastic. The response of the sinusoidal output strain will be the combination of the viscous and

elastic phases of the material. The viscoelasticity of the material is determined by measuring the modulus i.e., storage and loss modulus. The storage modulus ( $G'$ ) measures the elastic characteristics of the hydrogel, it is also a measure of the deformation of energy stored while shearing and is used as a driving force for the reformation of the structure when the shear load is released. It can be calculated from Equation (4.5). Where  $\sigma_o$  is the stress,  $\gamma_o$  is the strain and  $\delta$  is the phase angle between stress input and strain output. Similarly, the loss modulus ( $G''$ ) represents the viscous behavior (structural change) and is a measure of energy dissipation during deformation. It can be calculated from Equation (4.6).

The complex modulus characterizes the complete viscoelastic behavior containing both elastic and viscous portions and can be calculated using Equation (4.7). The loss factor ( $\tan \delta$ ) signifies the overall viscosity of the hydrogel and is the measure of the ratio of the loss modulus to the storage modulus (Equation 4.8).

$$G' = \frac{\sigma_o}{\gamma_o} \cos(\delta) \dots\dots\dots (4.5)$$

$$G'' = \frac{\sigma_o}{\gamma_o} \sin(\delta) \dots\dots\dots (4.6)$$

$$G^* = G' + iG'' \dots\dots\dots (4.7)$$

$$\tan(\delta) = \frac{G''}{G'} \dots\dots\dots (4.8)$$

The variation in the viscoelastic property of the hydrogels as the function of angular frequency was characterized by rheological experiments. The correlation between storage ( $G'$ ) and loss modulus ( $G''$ ) of the composites as a function of angular frequency is depicted in Fig. 4.8. These material properties mainly depend on the coordinate bonds between the amino groups of chitosan and aldehyde functionality, electrostatic and hydrogen bonding between matrix and the reinforcement in the network. Initially, the  $G''$  values of all composites are less than the  $G'$  values for an angular frequency less than 350 rad/sec signifies all hydrogels are predominantly elastic behaviour rather than the fluid-like state. The storage modulus of the nanocomposite hydrogel increases in comparison to chitosan hydrogel and it reaches the highest value of 10 kPa for nanohydroxyapatite/chitosan composites. Similarly, CS/3BCP and

CS/2TNT composites exhibit the elastic modulus of 6.5 kPa and 7.2 kPa. These values are around 5-7 times higher than the storage modulus of pure chitosan hydrogel which is around 1.6 kPa indicates the good interfacial compatibility between chitosan matrix and reinforcements. The storage modulus of hydrogel slightly increases with increasing frequency, which is similar to the changing rule with the frequency of natural cartilage. This signifies that physically cross-linked hydrogels have superior mechanical strength and could withstand shear stress caused by synovial fluid in the di-artrodial joint. As an angular frequency increases above 350 rad/sec,  $G''$  values raised above  $G'$  shows that the entanglements developed by generated hydrogen bonding between deprotonated  $-NH_2$  and  $-OH$  groups; and interaction of N-acetyl and main polysaccharide backbone of CS were broken and signified the end of the viscoelastic region at the critical stress.

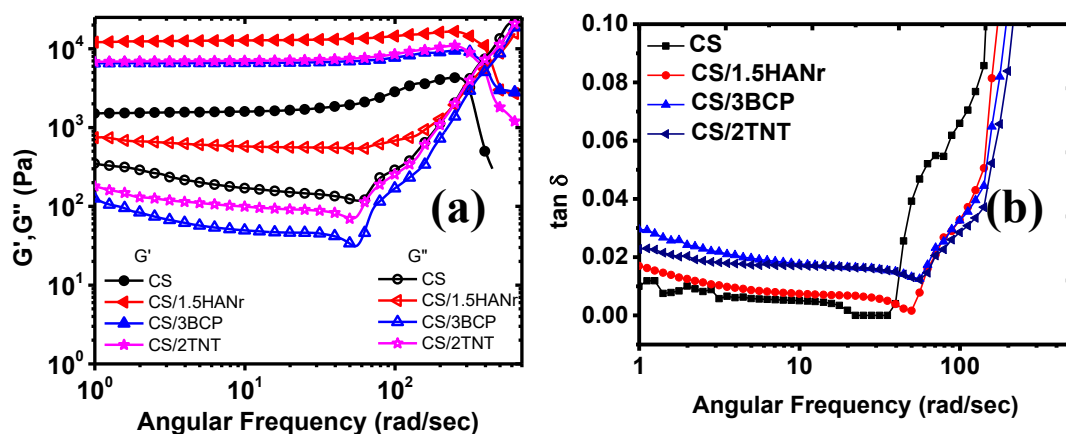


**Fig. 4.8** Variation of (a) storage and loss modulus and (b)  $\tan \delta$  of the composite hydrogel as a function of angular frequency

### 4.5.3 Biological studies

#### 4.5.3.1 Antimicrobial properties

The antimicrobial activities are the critical parameters to avoid bacterial infections and biofilm formation. In this study, two bacterias namely gram-negative *Escherichia coli* and gram-positive *Staphylococcus aureus* and the fungus *Candida albicans* were used.

The *Escherichia coli* (*E. coli*) is a Gram-negative, facultative anaerobic, coliform bacterium of the genus *Escherichia* that is commonly found in the lower intestine and gut of a human. These cells are typically rod-shaped structures with 2  $\mu\text{m}$  long, 0.25-1.25  $\mu\text{m}$  in diameter with a cell volume of 0.6-0.7  $\mu\text{m}$ . Usually, these are harmless that produce vitamin  $K_2$ , which helps in blood clotting during an injury and

also helps to keep the digestive tract healthy. However, some virulent strains can cause urinary tract infections, gastroenteritis disease, neonatal meningitis (blood infection), hemorrhagic colitis (infection in the large intestine) and Crohn's disease (infection in the digestive tract).

The gram-positive *Staphylococcus aureus* (*S.aureus*) round-shaped bacteria are usually found in the upper respiratory tract and on the dermal surface. The cells are typically in the range of 0.1-0.25  $\mu\text{m}$  in diameter and 1-1.5  $\mu\text{m}$  in length. Some of the *S.aureus* species play a prominent role in blood coagulation. However, the mechanism is still under debate. While, as the concentration of this species increases, it acts as a commensal bacterium, which sometimes can cause diseases. The most common diseases from this species include bacteremia (blood infection), infective endocarditis (infection in the inner surface of the heart valve), infection at the mucosal membranes of the intestines, urogenital tract and the respiratory system, various kinds of dermal infection, soft tissue infections and chronic biofilm formation on the implant materials especially joint replacement implants causes pus formation leading to chronic septic arthritis.

*Candida albicans* (*C. albicans*) is the oval-shaped pathogenic yeast commonly found in the human gut, gastrointestinal tract and mouth saliva. It is a human-friendly fungus that helps in the breakdown of fibers present in the food. These are usually commensal organisms; however, overgrowth of this species causes candidiasis (causes a red, itchy rash, most commonly in the folds of the skin). It was considered to be the fourth most commonly isolated organism that causes severe infection on the tongue for AIDS and cancer patients. It is the most common fungal species that cause biofilm formation on implants or scaffolds. This biofilm formation involved four steps: First, the yeast-form cells adhere to the substrate. The next step is the intermediate step, where the cells dedifferentiate to form microcolonies. In the maturation step, the cells increase their immunity by accumulating the extracellular matrix in it. Finally, the matured cells are released from the colonies and develop the biofilm on the implant/scaffold surface that has the characteristic properties of virulence and drug tolerance.

In this study, the microbes were cultured and the antimicrobial activity of the hydrogels against these microbial species was evaluated. As explained above, these three microbes are commonly found in the human body and they are commensal

organisms (organisms that are beneficial for daily activity, however, overgrowth leads to an adverse effect on health). Therefore it is essential to study the effect of these microbes on the composite hydrogel implant.

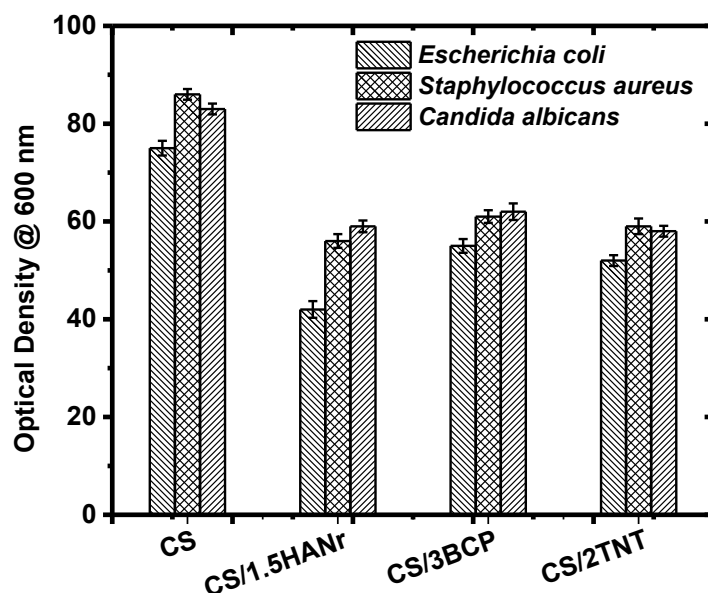
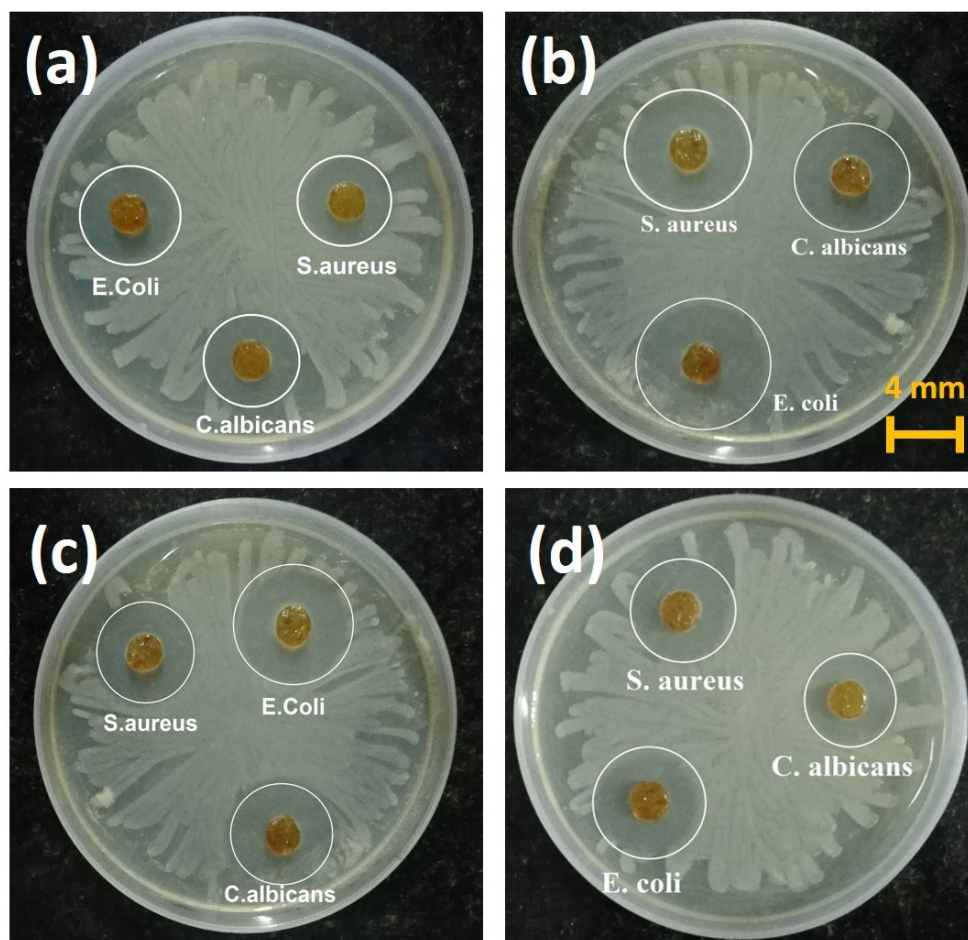


Fig. 4.9 Antibiogram of chitosan and its composite hydrogel

The antibiogram of hydrogels are as shown (Fig. 4.9). Composite hydrogel showed superior inhibition against *Escherichia coli* and *Staphylococcus aureus* bacteria compared to the pristine CS hydrogel. The reinforcement was more effective for *Escherichia coli* since 20%, 8% and 9% more inhibition was found for CS/1.5HANr, CS/3BCP and CS/2TNT compared to *Staphylococcus aureus*. One reason for this weak antibacterial activity against *Staphylococcus aureus* is that the drug-resistant outer multi-layered membrane, which consists of lipid and polysaccharide composed of O-antigen, outer and inner core formed by covalent bonds that is usually impermeable and blocks antibiotics. However, *Escherichia coli* has a few layered cell walls composed of murein, teichoic acids and wall-associated surface proteins, which dissolves quickly in the presence of a hydroxyl group of hydroxyapatite. Besides, few studies have reported that HANr causes increased Reactive Oxygen Species (ROS) production and activation of the inflammasome causes DNA damage, cell cycle delays, and apoptosis in mesothelial cells.

In CS/2TNT composites, the higher surface area of the nanotubes allows greater interaction with the proteins of the cellular membranes by producing reactive oxygen

species (ROS). This produces hydroxyl radicals (-OH-) and superoxide anion radicals generated by the reduction of oxygen species which dissolves microbial cells such as liquid peroxidation of the cell membrane, damaging DNA and causes leakage of amino acids leads to the death of microbes.



**Fig. 4.10** Zone of inhibition of chitosan and chitosan hydrogel against *Escherichia coli*, *Staphylococcus aureus* and *Candida albicans* after 24 h of incubation.

When *C. albicans* biofilms were exposed to nanohydroxyapatite and  $\beta$ -tricalcium phosphate reinforced nanocomposite hydrogels, a significant reduction in the growth of the fungus was observed. Although, the mechanism of biofilm dissolution was not fully understood. The calcium ions of nanohydroxyapatite and  $\beta$ -tricalcium phosphate dissolves the outer membranes by oxidizing phospholipids of the outer cell membrane of *Candida albicans* cause changes in the cellular morphology and cytoplasmic leakage leading to the death of the pathogen. Besides, the phosphate ions dissolve the outer layer of the fibroblast thus affects the extracellular matrix production

controls the growth of biofilm. The antimicrobial activity of titanium nanotubes has been explained in many ways. It was reported that the introduction of titanium nanoparticulates could damage the outer cell membranes of the prokaryotic yeast causes cell death. Others have reported that the oxides of titanium depolarize the membrane, release the intracellular glucose and trehalose, a decrease plasma membrane fluorescence with increasing concentrations of the nanotube. Kim et al. carried out similar studies on titanium nanoparticle-treated chitosan against *C.albicans* biofilm. The presence of pits in the cell wall and pores in the plasma membrane demonstrates that the titanium nanoparticles destruct the fungal membrane integrity and inhibit the normal budding process (Kim 2018).

Further, the zone of inhibition obtained from disc diffusion values are in good agreement with the results of the growth inhibition assay. Fig 4.10 shows the agar plates with a zone of inhibition (ZOI) against tested microbes. It concedes the susceptibility of the microbe towards the antibiotic. The width of the inhibition zone around the samples is summarized in Table 4.3. All the samples had a zone of inhibition greater than 3 mm demonstrates antimicrobial activity was a good level according to the standard SNV 195920-1992.

**Table 4.3** Inhibition area of microbial growth calculated around the samples through the disc diffusion test.

Pathogen	annular radius			
	CS	CS/1.5HANr	CS/3BCP	CS/2TNT
<i>E. coli</i>	7.9±0.2	9.8±0.1	7.8±0.2	6.1±0.2
<i>S.aureus</i>	6.6±0.1	7.6±0.2	6.6±0.1	5.9±0.2
<i>C. albicans</i>	6.5±0.2	6.3±0.2	6.1±0.2	5.8±0.2

#### 4.5.3.2 Cytotoxicity assay

Cytotoxicity is the primary evaluation of the biological properties of biomaterials *in vitro*. The viability of cells or proliferation is a good indicator of cell health. During material preparation, samples were treated with physical and chemical agents that may be toxic to cells which destroy the cell membrane and have adverse effects on protein adsorption. To determine cell death, there is a need for low cost, reliable and short term cytotoxicity and cell viability assays. A broad spectrum of cytotoxicity assays such as dye exclusion, colourimetric assay, fluorometric assay and luminometric assays are currently used for cytocompatibility evaluation. The selection



of the assay depends on the type of material, application, test compounds, specificity and sensitivity.

*In vitro* cytocompatibility assays has been of increasing interest over recent years. Because these tests are rapid, inexpensive and do not require animals for testing. Besides, they are useful for a large number of samples. Also, the use of human cells for assay has more relevant than *in vivo* animal studies. However, these studies have few disadvantages because they are not technically advanced enough to replace animal tests.

The *in vitro* cytocompatibility of the nanocomposite hydrogels was evaluated by MTT assay. It is a colourimetric assay used to evaluate cytotoxicity and cell viability. The test is based on the reduction of yellow-coloured water-soluble tetrazolium dye MTT 3-(4,5-dimethylthiazol-2-yl)-2,5-diphenyltetrazolium bromide to its insoluble formazan. Mitochondrial lactate dehydrogenase produced by live cells reduces MTT to insoluble formazan crystals, which upon dissolution in the presence of DMSO, shows a purple-coloured solution whose intensity is proportional to the number of viable cells and it is to be measured spectrophotometrically at 570 nm. Since the developed scaffolds intended to be used for cartilage application, the L929 fibroblast and MG63 osteoblast cell lines were used for viability evaluation.

Fibroblast cells are the type of biological cells that produce glycosaminoglycans, collagens, elastin fibers and glycoproteins that are found in the extracellular matrix (ECM). They provide structural stability to the tissue and plays a critical role in wound healing. They are commonly found in the connective tissues of animals. Fibroblasts are the ideal cell model for studying various biological events and disease stages such as cell growth and differentiation, dermal disease, wound healing, cancer, drug toxicology. The osteoblasts are the specialized mesenchymal cells that synthesize bone matrix and participated in bone mineralization and regulate calcium and phosphate in the developing bone. These are work in harmony with the osteoclasts (bone dissolving cells) throughout life. Osteoblasts are usually cubic, round or cylindrical with 20-50  $\mu\text{m}$  in diameter. They are usually found on the surface of the bone with hairy protrusions on its surface that helps to connect the adjacent cells and penetrate the surrounding bone-like tissue.

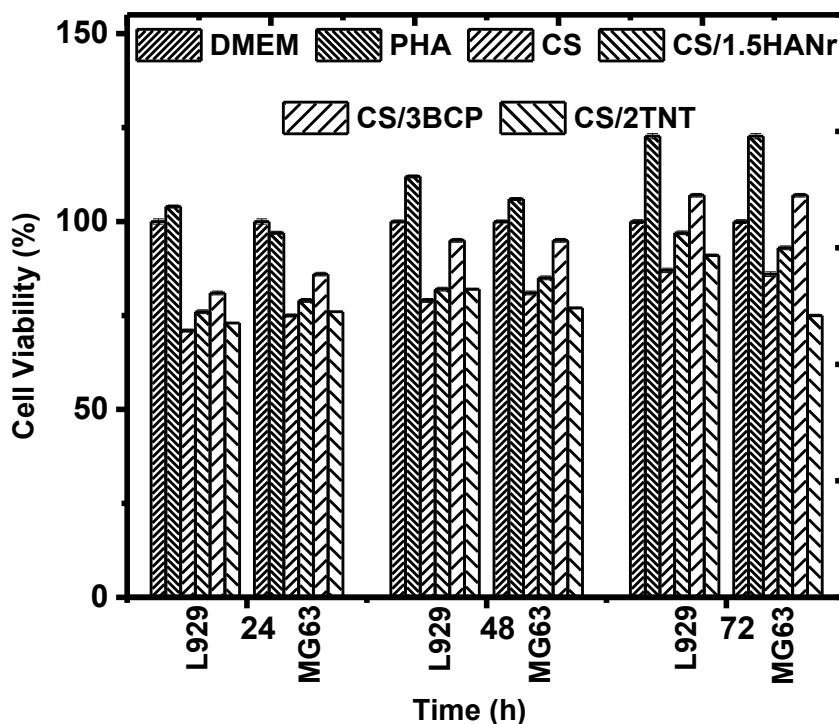


**Fig. 4.11** L929 and MG63 cell viability of on CS, CS/1.5HANr, CS/3BCP and CS/2TNT composite hydrogel after 72 h of incubation

The *in vitro* cytotoxicity of the composite hydrogel towards L929 and MG63 cell lines was evaluated using MTT assay. The mammalian cell viability on CS, CS/1.5HANr, CS/3BCP and CS/2TNT was reported and is compared with the DMEM (control) and Phytohaemagglutinin, PHA (standard) treated samples after 24, 48 and 72 h of incubation are as shown (Fig. 4.11).

It was observed that the cell viability increased with increasing time for both L929 and MG63 cells. The PHA treated sample shows the highest cell viability (122 % and 119.7 % for L929 and MG63 respectively) and the viability of L929 cells on CS/1.5 HANr, CS/3BCP and CS/2TNT composite substrate was  $97 \pm 0.21\%$ ,  $108 \pm 0.42\%$  and  $86 \pm 0.41\%$  respectively. Similarly, MG63 cells show  $93 \pm 0.42\%$ ,  $107 \pm 0.11\%$  and  $75 \pm 0.35\%$  after 72 h of incubation. All the composite hydrogels show better cell proliferation than pristine CS ( $90 \pm 0.63\%$  towards L929 and  $92.31 \pm 0.22\%$  towards MG63 cells). The introduction of biphasic calcium phosphate in the composite hydrogel induces cell viability. It could be due to the release of  $\text{Ca}^{2+}$  and  $\text{PO}_4^{3-}$  bioactive ions which anchor chitosan hydrogel might afford a tissue-like environment for cell adhesion and proliferation.

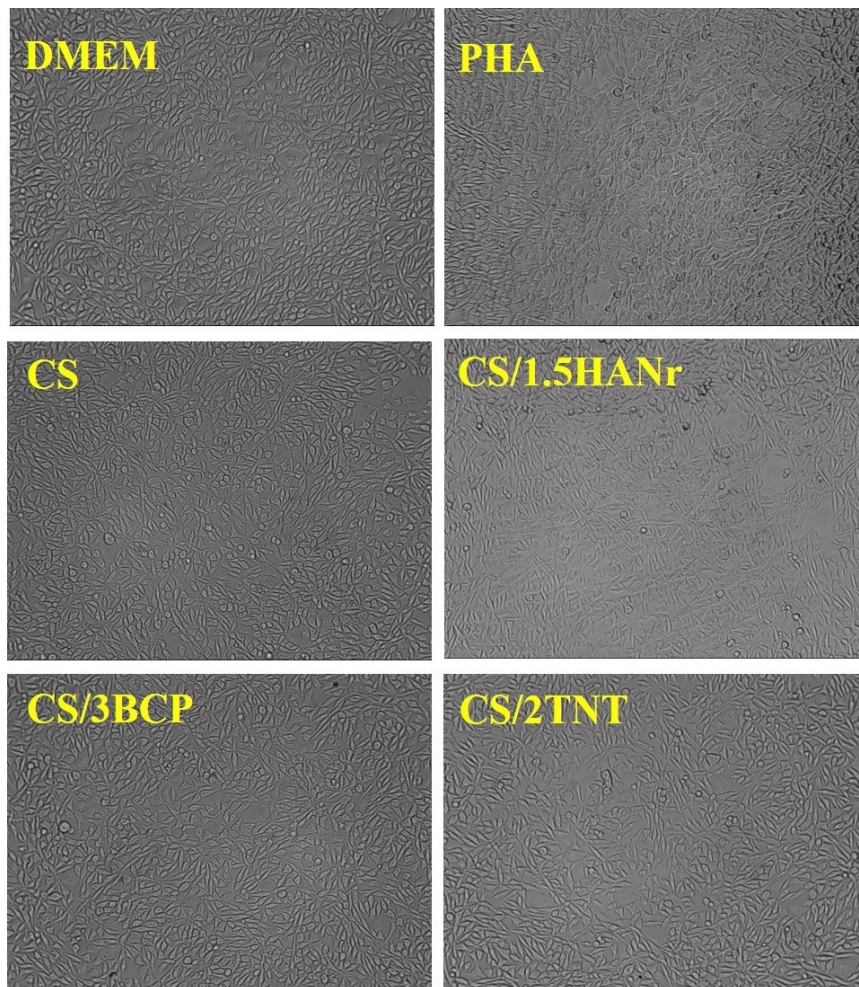


**Fig. 4.12** Inverted microscope images of L929 cell viability towards DMEM, PHA,CS, CS/1.5HANr, CS/3BCP and CS/2TNT after 72 h of incubation.

As per ISO standards for biocompatibility evaluation, composite hydrogel did not show any cytotoxicity for both L929 MG63 cells since its relative viability was more than 70% (Picone et al. 2019). Further, the inverted microscopic images provide a preliminary understanding of the cellular response to hydrogels (Fig.4.12 and 4.13). It was found that L929 mouse fibroblast cells exhibited a fusiform morphology and most of the cells spread and proliferate well on the culture plate. Similarly, MG63 human osteoblasts exhibit cubic structure and they proliferate well on all the composites showed no apparent cytotoxicity within the incubation of 72 h and are the potential biomaterials with excellent antibacterial activities without significant cytotoxicity towards fibroblast and osteoblast-like cells.

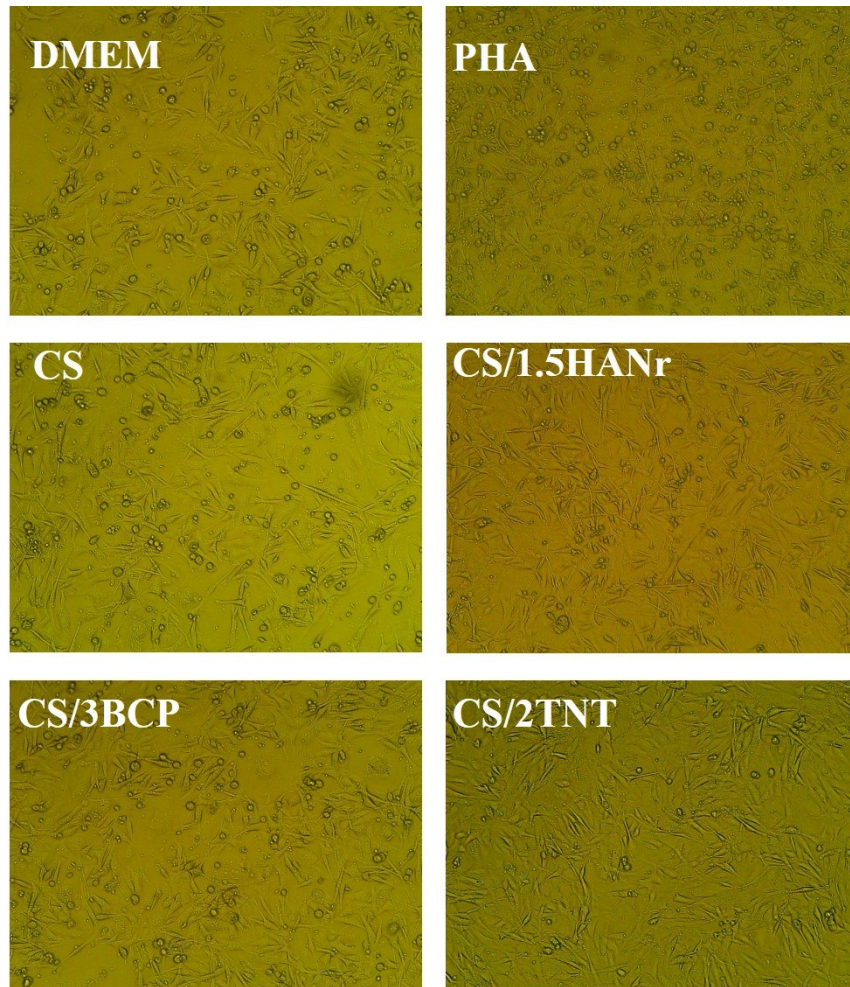


**Fig. 4.13** Inverted microscope images of MG63 cell viability towards DMEM, PHA,CS, CS/1.5HANr, CS/3BCP and CS/2TNT after 72 h of incubation.



## CHAPTER 5

### **EFFECT OF BIOCERAMICS ON POLYVINYL ALCOHOL HYDROGEL FOR CARTILAGE TISSUE IMPLANTS**

---

This chapter describes the influence of bioceramics HANr, BCP and TNT on the physical, mechanical and biological properties of polyvinyl alcohol (PVA) hydrogel for cartilage tissue replacement application. PVA hydrogels made of synthetic polymer have desirable physical and mechanical properties needed for tissue engineering applications. However, the bio-inertness hinders the application *in vivo*. This issue can be overcome by adding suitable bioceramic reinforcement. The tailor-made PVA nanocomposite hydrogels were developed through the physical freeze-thaw method without adding the toxic surfactants, followed by annealing treatment. The composite scaffolds were characterized by Scanning Electron Microscope (SEM) and Fourier Transform Infrared Spectroscopy (ATR-FTIR) for morphology analysis and structural modification evaluation. The physical, mechanical, rheological and biological properties were analyzed. The bioceramic reinforced PVA composite hydrogels show favourable material properties for cartilage tissue replacement application.

#### **5.1 Materials used for composites**

Hot water-soluble polyvinyl alcohol (molecular weight 60,000-125,000 Da) was procured from Himedia Ltd. Mumbai, India. All other chemicals and reagents were used as received.

#### **5.2 Development of PVA/HANr, PVA/BCP and PVA/TNT composite hydrogel**

For processing hydrogel, 15 g of PVA was dissolved in 70 mL demineralized water at 70 °C until a clear solution was formed. Meanwhile, the sonicated suspension of bioceramic reinforcements (HANr, BCP and TNT) was prepared and is mixed with the previously prepared PVA gel. The stirring was continued for another 12 h at the same temperature. Finally, the gel was transferred into a polystyrene petri dish and cooled to room temperature. For physical crosslinking (polymerization), the gels were subjected to 5 cycles of freeze-thaw process, consisting of freezing at -21 °C for 8 h followed by thawing at room temperature for 3 h. In the end, samples were annealed at 120 °C for 1 h and stored for further characterization.

### 5.3 Characterization of PVA and its composite hydrogel

#### 5.3.1 Physical characterisation

To study the hydrogel morphology, pore size and porosity, SEM (JSM-6380LA, JOEL, Japan) micrographs were obtained. The average pore size was determined by the JAVA based image processing program ImageJ by scaffold imaging. The structural modification of PVA composite hydrogel in comparison with neat PVA hydrogel was identified by Attenuated Total Reflectance Fourier Transform Infrared (ATR-FTIR) Spectroscopy from the Bruker alpha instrument at an operating wavelength range of 4000-500  $\text{cm}^{-1}$ .

For swelling studies, hydrogels (cylindrical samples were considered) were lyophilized and their initial weight was measured ( $W_i$ ). Then the samples were incubated in distilled water at 37 °C until no change in mass was observed ( $W_f$ ). The swelling ratio was calculated as the ratio of weight to initial weight. Similarly, for the water retention ability study, fully swollen hydrogels were wrapped with the filter paper, centrifuged at 600 rpm for 5 min. The surface of the sample was cleaned and weight was measured ( $W'_f$ ). the water retention ability was calculated as;

$$E_R = \frac{(W'_f - W_i)}{W_i} \times 100 \dots\dots\dots (5.1)$$

The surface wettability or adsorption potency of the hydrogel scaffold was measured by assessing the angle formed between a drop of fluid (Phosphate Buffer Saline, PBS at 7.2 pH) and the hydrogel surface at the three-phase boundary where liquid, gas and solid intersect as shown in Fig. 4.1.

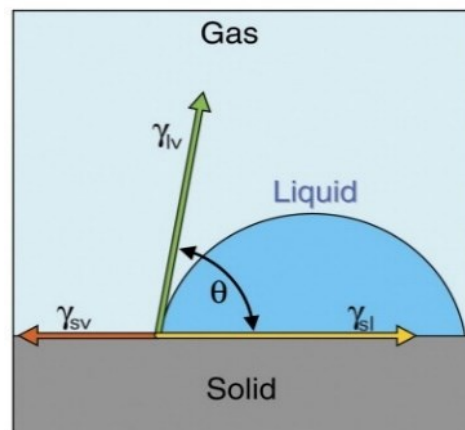


**Fig. 5.1** Wetting of solid surface according to young's equation  $\gamma_{sv} - \gamma_{sl} = \gamma_{lv} \cos \theta$ .

The hydrogel films of 0.5 mm thick were cast on the glass substrate and the contact angle was determined using the Drop shape analyzer (Kruss, Germany). For each sample, five readings were taken at different spots and their average was recorded. The porosity of the hydrogel was determined by the liquid displacement method. For porosity measurement, the fully crosslinked cylindrical samples (10 mm diameter and 10 mm height) were immersed in 100 mL ethanol until no change in mass was observed. Then the samples were removed from the medium and measure the final weight ( $W_2$ ). Finally, samples were lyophilized and measured the dry weight ( $W_1$ ). The porosity was calculated as;

$$\text{Porosity} = \frac{(W_2 - W_1 - W_3)}{(W_2 - W_3)} \times 100 \dots\dots\dots(5.2)$$

Where  $W_3$  is the weight of the ethanol after removal of the hydrogel sample.

### 5.3.2 Mechanical test

For determining the elasticity, maximum tensile stress and tensile strain dumbbell-shaped fully swollen hydrogel samples were prepared as per ASTM -D638 (gauge length 60 mm, width 8 mm and thickness 3 mm). The sample was held between the grippers of the Universal Testing Machine (Mecmesin MultiTest 10-i, London) and the experiments were performed with a crosshead speed of 10 mm/min (Bhowmick and Koul 2016). The unconfined compression and cyclic loading-unloading compression tests were performed in the universal testing machine (Mecmesin MultiTest 10-i micro UTM, London) with a 1000 N load cell. The cylindrical samples of 10 mm diameter and 7 mm height were used with a crosshead speed of 5 mm/min for unconfined compression tests and 20 mm/min cyclic loading-unloading compression tests. Before the test, a preload of 0.01 N was applied to confirm the clear contact between the compression plates and the hydrogel. The force and deformation data were used and the Stress vs Strain graph was plotted. The Elastic modulus (E), Stress-at-break ( $\sigma_{\max}$ ) and Strain-at-break ( $\epsilon_{\max}$ ) were determined from the curves.

### 5.3.3 Rheological Test

For rheological characterization, hydrogel discs (25 mm diameter and 2 mm thick) were used. The test was performed at 37 °C in an MCR 302 Anton Paar Rheometer parallel plate setup. An oscillatory frequency sweep test was carried out in



the frequency range of 0.1-100 Hz with a fixed strain of 1%. The components of complex modulus such as storage modulus (G') and loss modulus (G'') were investigated.

#### 5.3.4 Measurement of coefficient of friction

A friction test was performed on the High-Frequency Reciprocating Rig (Ducom, India). The cylindrical hydrogels (6 mm diameter, 12 mm height) were held on the sample holder with cyanoacrylate glue. The gel was reciprocating against the flat silica disc. The testing parameter is summarized in Table 4.2 are within the boundary regime of hard tissue (Parkes et al. 2015). The coefficient of friction was measured throughout the test and a curve of friction coefficient vs time was plotted.

#### 5.3.5 Degradation studies

*In vitro* biodegradability of the scaffold was evaluated as explained elsewhere (Venkatesan and Kim 2014). In brief, samples were kept in centrifuge tubes consisting of 0.1 M phosphate buffer saline (pH 7.2) with lysozyme enzyme (0.5 mg/mL). Then, the centrifuges were kept in an oscillating incubator at 37.0±0.5 °C. After 30 days of the experiment, samples were removed and wiped with absorbent paper and weight was measured. The weight loss of the hydrogel sample was calculated as;

$$W_L = \frac{(W_i - W_f)}{W_i} \times 100 \dots\dots\dots(5.3)$$

Where  $W_i$  and  $W_f$  are the weight of the hydrogel before and after soaking respectively.

#### 5.3.6 Growth inhibition test

The antimicrobial activity of the nanocomposite hydrogels was evaluated according to the growth inhibition assay using the modified method explained elsewhere (Wei et al. 2016). In brief, 150 µL of nutrient broth and 50 µL of diluted bacterial or fungal culture were taken in a 96 well culture plate. The initial absorbance at 600 nm was measured in a Thermo scientific Multiscan® plate reader and considered as initial bacterial/fungal concentration. Then, 10 mg of triplicate hydrogel samples were added to the respective well and incubated overnight at 37 °C. The inoculum was then monitored for changes in the absorbance at 600 nm (OD<sub>600</sub>). The well without any sample was considered as a control. The percentage growth inhibition was calculated.

### 5.3.7 Measurement of cytotoxicity

The cytocompatibility of the hydrogel was assessed by determining the viability of the L929/MG63 cells in response to the conditioned media using MTT assay. Briefly, hydrogel discs (10 mm diameter, 2 mm thick) were sterilized in 70% ethanol followed by washing in a sterile PBS. L929/MG63 cells were seeded on the hydrogel surface (50,000 cells/well) in a 24-well plate with DMEM supplemented with 10% FBS and incubated at 37 °C for 72 h in 5% CO<sub>2</sub>. Then, the media was replaced with MTT to a final concentration of 5 mg/mL and incubated for another 3 h. Finally, 100 µL of DMSO was added with gentle stirring in a gyratory shaker. The medium without any treatment was considered as control (100%) and cell activator Phytohaemagglutinin (PHA) treated hydrogel was considered as standard (Le et al. 2018) (Jaiswal 2010). The optical density (OD) of the media was measured at 570 nm to determine the cell viability, according to the equation:

$$\text{Cell viability (\%)} = \frac{\text{OD}_{\text{test}} - \text{OD}_{\text{blank}}}{\text{OD}_{\text{control}} - \text{OD}_{\text{blank}}} \dots\dots(5.4)$$

Where  $\text{OD}_{\text{test}}$ ,  $\text{OD}_{\text{control}}$  and  $\text{OD}_{\text{blank}}$  are the optical densities of cells incubated with hydrogel, DMEM with cells and DMEM without cells respectively.

## 5.6 Statistics

All quantitative results were obtained from triplicate samples and data were shown as a mean  $\pm$  standard deviation. Statistical significance is calculated using the one-way ANOVA test. A value of  $p < 0.05$  was considered statistically significant.

## 5.7 Results and Discussion

### 5.7.1 Morphology and IR analysis

The images of the PVA and its composite hydrogels are as shown in Fig. 5.2. It can be seen that polyvinyl alcohol hydrogel is transparent, whereas the addition of reinforcement turns the gel opaque and white.

The internal morphology of the cross-sectional view of the lyophilized hydrogels is as shown in Fig. 5.3. All the samples show a porous structure with interconnected porosity similar to human articular cartilage.

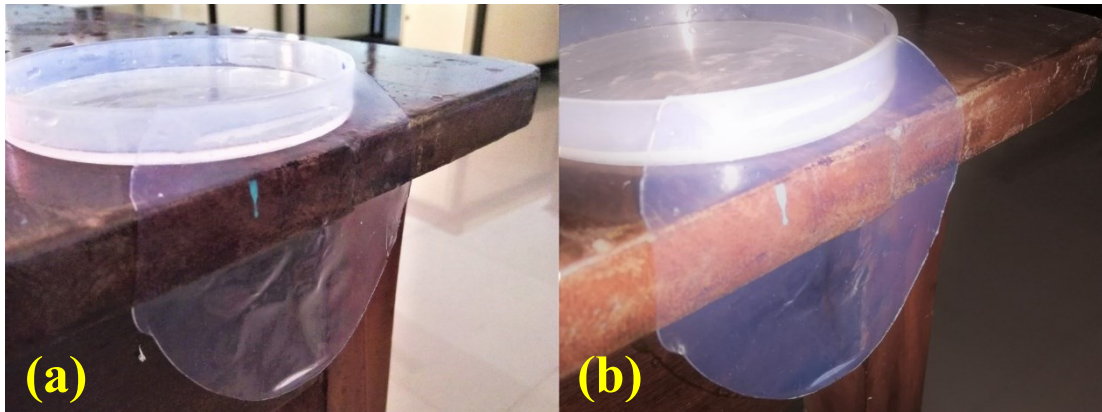


**Fig. 5.2** Macroscopic images of (a) PVA and (b) PVA composite hydrogel

The microarchitecture of the scaffold such as pore size and interconnectivity is a crucial factor for mammalian tissues since they do not have blood vessels and nervous systems. The pore profile is significant to facilitate the cell penetration, migration, nutrient diffusion and removal of metabolic wastes in the biological environment.

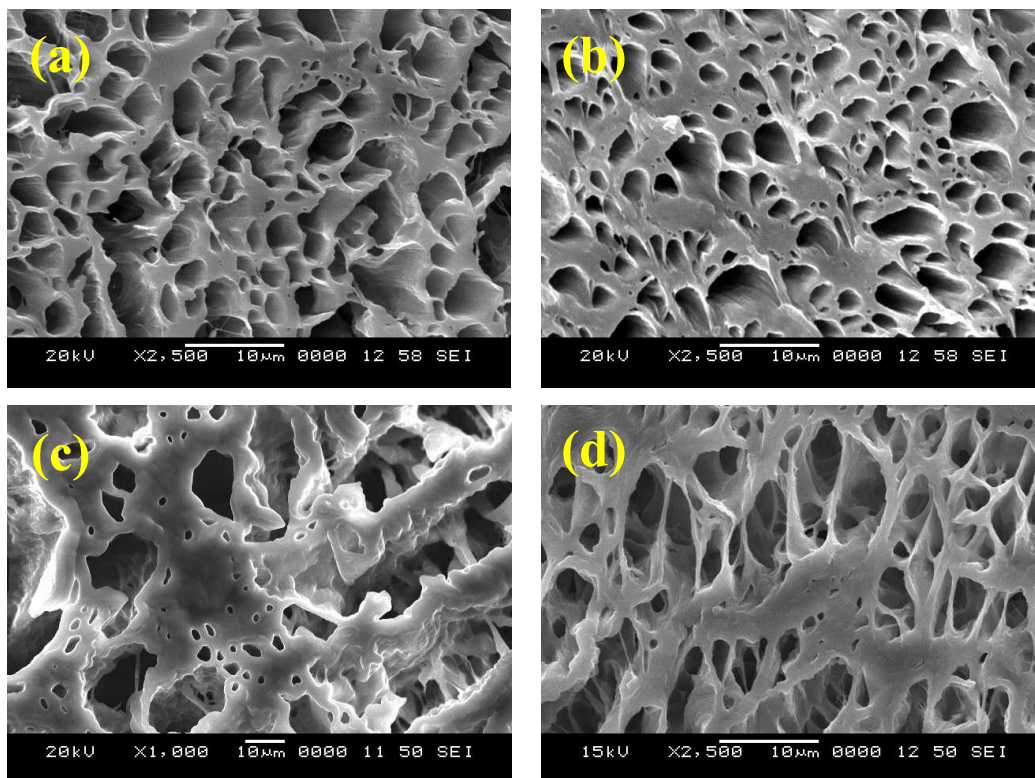


**Fig. 5.3** Scanning electron microscope images of (a) PVA (b) PVA/2HANr (c) PVA/2.5BCP and (d) PVA/2TNT composite hydrogel

Previous studies have reported that decreasing pore size and porosity impair the infiltration of cells and may result in an uneven cell distribution in the scaffold. On the

contrary, this pore size and porosity inversely affect mechanical strength. Certainly, the polymer network structure, pore shape, volume and interconnectivity can be controlled according to the application by varying freeze-thaw cycles.

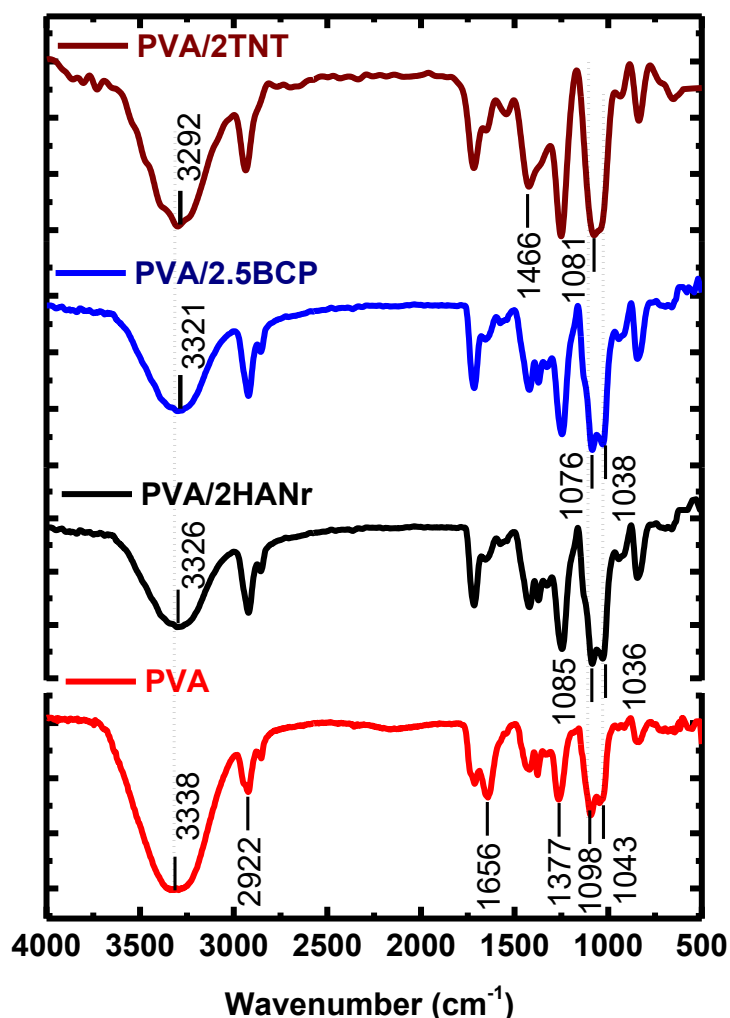


**Fig. 5.4** FTIR of PVA, PVA/2HANr, PVA/2.5BCP and PVA/2TNT composite hydrogel

The structural modification in the PVA hydrogel due to the bioceramic reinforcement was identified by the FTIR spectrum (Fig. 5.4). The characteristic peaks of PVA located at 3338 cm<sup>-1</sup>, 2922 cm<sup>-1</sup>, 1377 cm<sup>-1</sup> and 1098 cm<sup>-1</sup> in the spectrum of PVA and the large band existed in the range 3600-3200 cm<sup>-1</sup> is related to OH stretching vibration whereas absorption at 1098 cm<sup>-1</sup> corresponding to the crystalline region of PVA. A band at 1656 cm<sup>-1</sup> is due to C=C stretching, and the absorbance band in the range of 1397-1431 cm<sup>-1</sup> corresponds to CH<sub>2</sub> bond. In the case of PVA/HANr and

PVA/BCP composites, a slight shift in the IR absorption spectrum towards lower wavenumber in comparison to neat PVA hydrogel. Similarly, in PVA/TNT composites, the hydroxyl and C-O-C bands are shifted to 3292  $\text{cm}^{-1}$  and 1081  $\text{cm}^{-1}$  respectively. The shift of adsorption bands suggests the formation of hydrogen bonding between matrix and reinforcement which has been reported in earlier work (Peng et al. 2016).

### 5.7.2 Swelling and contact angle measurements

The majority of the water in the connective tissue is held between the myofibrils, cell membranes, muscle cells and muscle bundles. Furthermore, tissues consist of a few compartments, i.e. space within the microfibrils and space between the muscle bundles. Water holding and retention from these compartments involve slightly different mechanisms. Water is a dipolar molecule that is attracted to charged species like proteins. In fact, some of the water molecules are more closely *bound* to protein molecules. This *bound water* has reduced mobility and they do not easily move towards the compartments. More than 90% of the water present in the tissue is in the form of bound water. The remaining water is in the form of entrapped water in which the water molecules are adsorbed to the cell surface by weak Van der Waals or hydrogen bonds (Offer et al. 1989). Therefore, swelling strength and water retention study are the prime requirements for connective tissue scaffold materials.

**Table 5.1** Physical properties of PVA and its composite hydrogel

Sample	Swelling Ratio, SR, (%)	Water retention (%)	Average pore size ( $\mu\text{m}$ )	Porosity (%)	Contact angle ( $^{\circ}$ )
PVA	415 $\pm$ 5.22	411 $\pm$ 1.12	7.4 $\pm$ 0.33	81.73 $\pm$ 1.73	65.5 $\pm$ 0.32
PVA/2HANr	341 $\pm$ 6.85	339 $\pm$ 0.98	5.7 $\pm$ 0.10	76.21 $\pm$ 0.65	61.9 $\pm$ 0.21
PVA/2.5BCP	371 $\pm$ 6.23	370 $\pm$ 0.85	9.2 $\pm$ 0.34	83.12 $\pm$ 1.02	61.6 $\pm$ 0.23
PVA/2TNT	336 $\pm$ 8.58	334 $\pm$ 1.15	5.7 $\pm$ 0.25	85.26 $\pm$ 0.65	62.8 $\pm$ 0.66

Therefore, the swelling strength and water retention potency of the neat PVA and PVA composite hydrogels are studied. It is mainly related to the amorphous region and free hydroxyl groups in the polymer network. The swelling ability and retention potency of all the hydrogels are summarized in Table 5.1. As expected, the neat PVA hydrogels show the highest swelling of 415 $\pm$ 5.22 and 411 $\pm$ 1.12. It was noticed that both

the value decreases with increasing concentration of reinforcement (values not shown). It could be due to the reinforcement develops additional hydrogen bonds as confirmed by the FTIR spectrum, which arrests the free movement of the polymer chain. On the other hand, the introduction of bio-ceramic reinforcement increases the crystalline region and decreases the free hydroxyl group that causes swelling.

Surface wettability or adsorption potency is another essential parameter for cartilage scaffold which reflects the absorption of essential nutrients and promotes osteoblast growth. The contact angle values of PVA and its composite hydrogels are listed in Table 5.1. The hydrophilicity of PVA hydrogel has the highest value and is decreases with increasing reinforcement. Previous studies showed that the optimum contact angle for osteoblast growth and dedifferentiation of cells was estimated in the range of 50° and 70° (Agrawal et al., 2017). In this study, the contact angle of all the hydrogels are lies within this range and thus supports cell proliferation.

### *5.7.3 Mechanical characterization*

The mechanical property assessment for biomaterials is crucial to avoid stress mismatch at the scaffold/tissue interface. Therefore, tensile tests were performed as per ASTM -D638 and the maximum strength, elastic modulus of all the nanocomposite hydrogels are summarised in Table 5.2. The tensile strength of the neat PVA hydrogel is  $0.52 \pm 0.12$  MPa with deformation of 270 %. With the introduction of reinforcement, the strength increases and is reached to a maximum value of  $5.1 \pm 0.1$  MPa,  $5.7 \pm 0.8$  MPa and  $6.25 \pm 0.4$  for PVA/2.5HANr, PVA/2BCP and PVA/1.5TNT respectively. Further, the elastic modulus of the neat PVA hydrogel is 0.21 MPa and for composites this value increased to 3.1 MPa, 3.8 MPa and 3.9 MPa for PVA/2.5HANr, PVA/2BCP and PVA/1.5TNT respectively. Similarly, compression cyclic compression and fatigue test were performed for PVA and its composite hydrogels. As expected, hydrogels made of a synthetic polymer such as PVA shows higher mechanical properties than natural polymers as discussed in Chapter 4. When PVA hydrogel is loaded, the PVA amorphous phase in the network absorbs the load and gets reoriented. During this, a small load is enough for substantial deformation. Once the reorientation is accomplished, the 3D crystallite polymer phase hinders the free movement of the polymer chain and therefore it needs more load for the next deformation which was

observed in the compression stress-strain curve of PVA and its composite hydrogels as shown in Fig. 5.5 (a, c and e).

**Table 5.2.** Tensile mechanical properties of PVA nanocomposite hydrogel

<b>Composition</b>	<b>Tensile strength, <math>\sigma</math> (MPa)</b>	<b>Elongation at break, <math>\varepsilon</math> (%)</b>	<b>Tensile Modulus, E (MPa)</b>
PVA	0.52±0.12	270	0.21±0.05
PVA/2.5HANr	5.1±0.12	305	3.1±0.02
PVA/2BCP	5.7±0.8	352	3.8±0.12
PVA/1.5TNT	6.25±0.4	430	3.9±0.11

The compression strength of the neat PVA hydrogel is 4.2±0.6 MPa. The introduction of bio-ceramic reinforcement increases the strength to 13.9±0.1 MPa (PVA/2HANr), 14.2±0.4 MPa (PVA/2.5BCP) and 12.6±0.5 MPa (PVA/2TNT). This value is more than three times higher than the compression strength of the neat PVA hydrogel. In all three nanocomposites, as the reinforcement concentration increases, the compression strength increases confirms that the bioceramic develops additional hydrogen bonds that resist the free expansion of the three-dimensional network. On the other hand, as the bioceramic reinforcement concentration increases above a certain value the compression strength decreases due to agglomeration.

**Table 5.3** Compressive mechanical properties of PVA nanocomposite hydrogel

<b>Composition</b>	<b>Compression strength, <math>\sigma</math> (MPa)</b>	<b>Compressive Strain, <math>\varepsilon</math> (%)</b>	<b>Compression Modulus, E (MPa)</b>
PVA	4.2±0.6	61	1.26±0.6
PVA/2HANr	13.9±0.1	67	2.50±0.1
PVA/2.5BCP	14.2±0.4	72	2.55±0.2
PVA/2TNT	12.6±0.5	72.6	2.91±0.1

It is important to note that if the tissue engineering material is too tough, then there will be a lack of adherence at the interface of cartilage and hydrogel. The maximum pressure that the knee cartilage can bear is in the range of 1-6 MPa for moderate daily activities whereas, under the extreme condition it could reach 12 MPa. Similarly, the compression modulus of healthy articular cartilage which varies between 0.1 MPa to 2 MPa. In all the above nanocomposite hydrogels the value of compression

strength and modulus are higher, and it was concluded that these hydrogels are mechanically suitable for cartilage scaffold application.

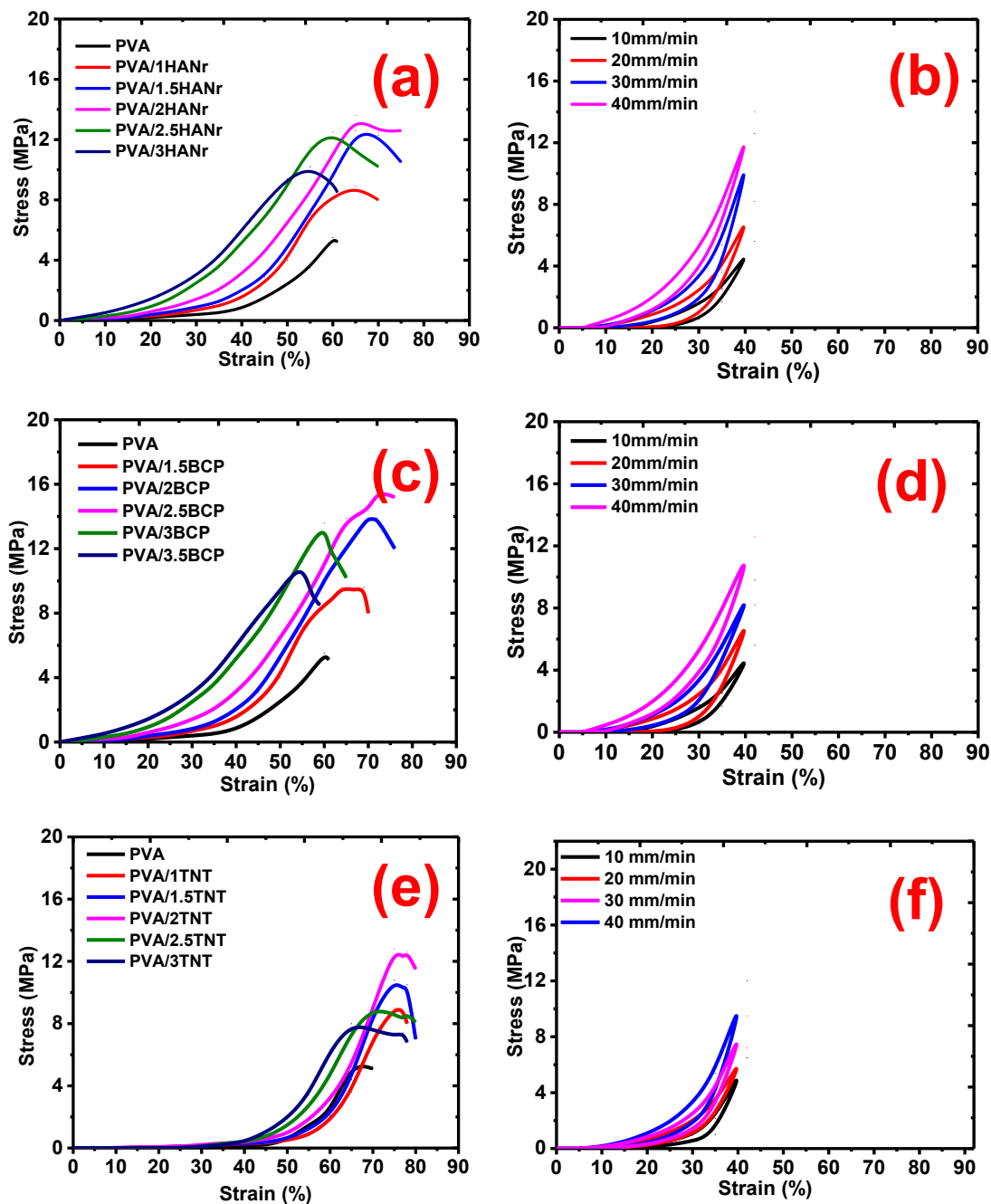


**Fig. 5.5** Unconfined compression and cyclic loading-unloading compression test (a-b) PVA/HANr, (c-d) PVA/BCP and (e-f) PVA/TNT composite hydrogels

To study the shear thickening behaviour of the composite hydrogels, a single cycle loading-unloading compression test was performed by varying the strain rate ranging from 10-40 mm/sec. The composite hydrogel exhibit the highest compression strength was considered for this test. That means, in nanohydroxyapatite reinforced



PVA hydrogel, the PVA/1.5HANr combination exhibit the highest compression strength of 12.4 MPa. Therefore, hydrogel made of this combination was considered for the cyclic loading-unloading compression test. In all the composite gels, the compression strength increases with the strain rate indicate the shear thickening effect.

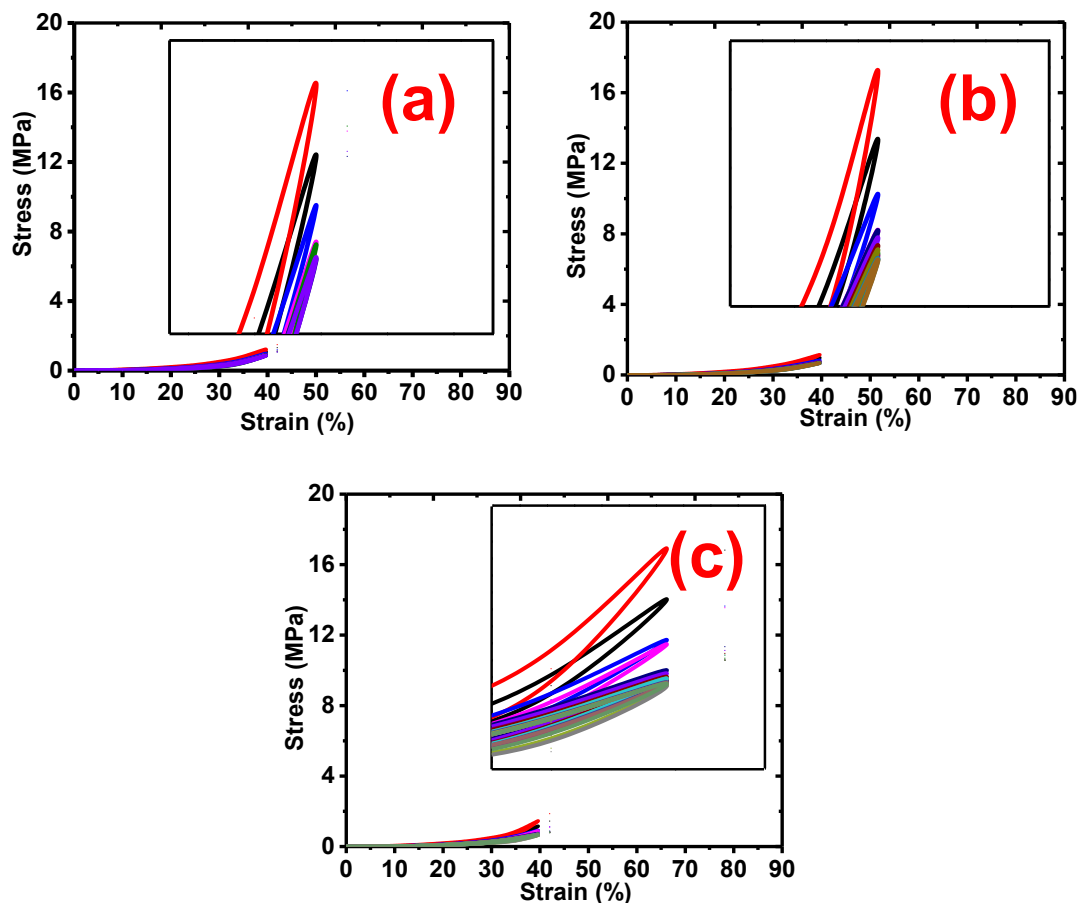


**Fig. 5.6** The cyclic loading-unloading compression test of (100 cycles) (a) PVA/2HANr, (b) PVA/2.5BCP and (c) PVA/2TNT composite hydrogels.

Further, to study the fatigue strength of the hydrogel, a hundred cycles of loading-unloading compression tests were performed at a rate of 10 mm/min with a constant strain of 40 %. As far as one can analyze the cyclic curves presented in Fig. 5.6, in the first four-five cycles, the compression strength decreases slightly due to the damage of a few chemical bonds that makes larger hysteresis loops. As the cycle is continued, some of the hydrogen bonds were re-established, which were able to bear load in the succeeding cycles. This confirms the composite hydrogel is a better self-recoverable and fatigue resistance property.

#### 5.7.4 Rheological behaviour of PVA and its composite hydrogel

All the mammalian tissues including cartilage show nonlinear viscoelastic characteristics. Therefore the connecting tissue scaffold material should meet the rheological characteristics. i.e., its elastic modulus must be independent of angular frequency and the storage modulus should be greater than the loss modulus at all frequencies. The viscoelasticity of the PVA and its composite hydrogel was assessed by measuring the components of complex modulus such as storage and loss modulus. The storage modulus ( $G'$ ) measures the elastic characteristics of the hydrogel, it is also a measure of the deformation of energy stored while shearing and is used as a driving force for the reformation of the structure when the shear load is released. Similarly, the loss modulus ( $G''$ ) represents the viscous behavior (structural change) and is a measure of energy dissipation during deformation.

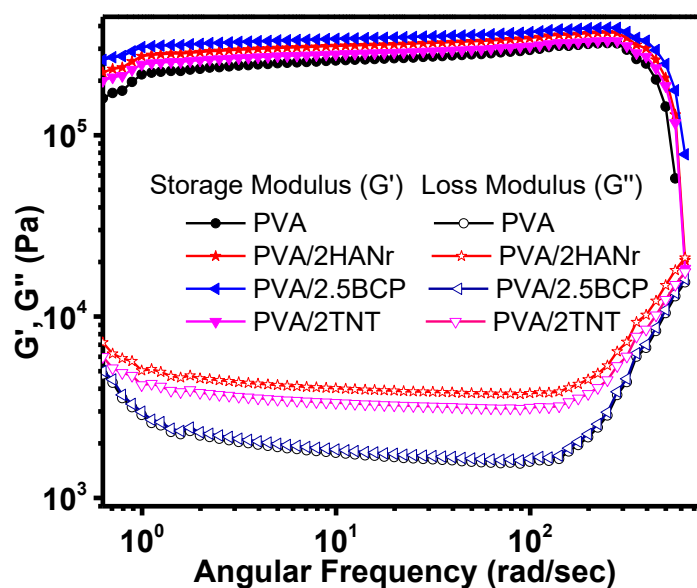


**Fig. 5.7** The variation of storage and loss modulus of PVA and its composite hydrogel

The correlation between storage and loss modulus of PVA and its composite hydrogels are depicted in Fig. 5.7. For all the hydrogels, the storage modulus ( $G'$ ) is always higher than the loss modulus ( $G''$ ) indicating that composites are elastic rather than have a fluid-like state. The elastic modulus of all the composite hydrogels is higher than the neat PVA hydrogel demonstrates that there is good interaction between matrix

and reinforcement. On the other hand, the fluid in the nanopores interlocks the polymer network and provides mechanical stiffness thereby resist the shear deformation.

### 5.7.5 Friction test

The friction coefficient of articular cartilage is extremely low with a value recorded in the range of 0.001-0.003. This low coefficient of friction owing to hyaluronan secretion by fibroblast-like cells of the synovial membrane, lubricin secreted by the surface chondrocytes lubricates the joint surfaces. According to Parkes et al., the equilibrium friction coefficient of cartilage against a stationary silica disc with PBS lubricant was 0.24. Based on this, the friction coefficient of hydrogels was measured. The hydrogel samples show higher initial and equilibrium friction than the cartilage sample. This is because for cartilage a boundary lubricant is expected to be present, which develops a layer between the surfaces.

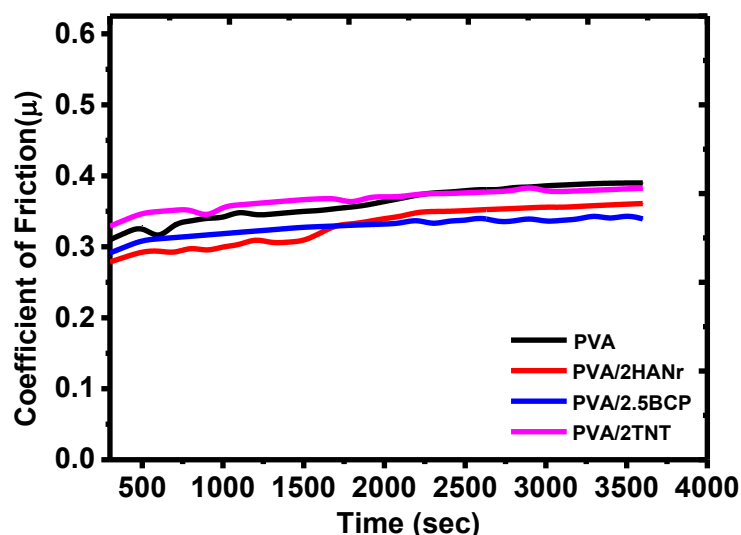


**Fig. 5.8** Friction coefficient of PVA and its composite hydrogel as a function of time

The friction traces of PVA and its composites are as shown in Fig 5.8. Initially, the friction was less and it was increased with increasing time. This is because, in the beginning, the fluid minimizes the direct contiguity by developing a dense fluid film between the rubbing surfaces. Over the course of time, the film thickness recedes as far as the friction coefficient was reached equilibrium. PVA/2HANr and PVA/2.5BCP composites show lower initial and equilibrium friction coefficient compared to neat PVA hydrogel. This is due to nanorod on the surface provide a rolling effect which will minimize the friction and the surface wear. The degradation study results confirm that

the PVA and composite hydrogels show less than 1% degradation even after 28 days confirms a slower degradation rate and they are suitable for a cartilage replacement application.

#### 5.7.6 Measurement of antimicrobial properties

The evaluation of the antimicrobial activity of biomaterial is crucial to avoid post-surgical infection and biofilm formation. The antibiogram of PVA and its composite hydrogel are as shown in Fig 5.9a. As expected, composite hydrogels show superior antimicrobial activity than pristine PVA. The bioceramic reinforcement was more for gram-negative *Escherichia coli* than gram-positive bacteria and fungi. This is due to the variation in the cell wall structure of gram-positive and gram-negative bacteria as explained in the previous chapter. However, for *Candida albicans*, when they are exposed to biocompatible nanohydroxyapatite and  $\beta$ -tricalcium phosphate, the calcium and phosphate ions produces reactive oxygen species that damage the biofilm thereby reduces the fungal activity.

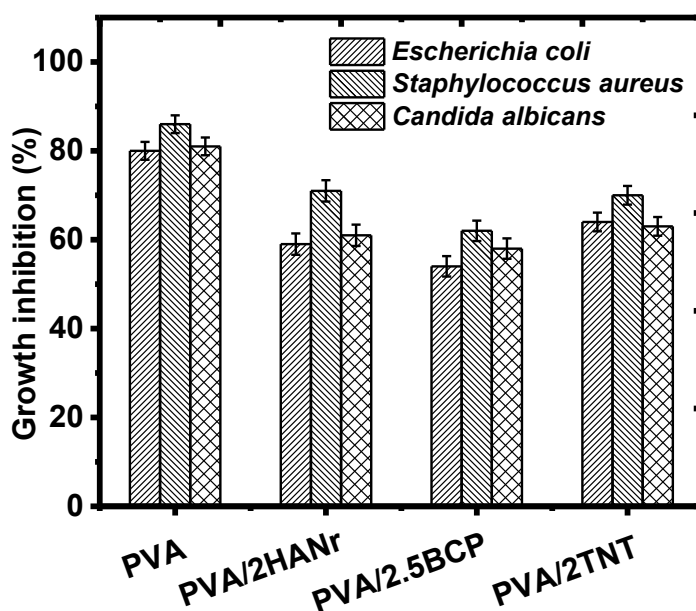


**Fig. 5.9** Antibiogram of PVA and its composite hydrogel against *Escherichia coli*, *Staphylococcus aureus* and *Candida albicans* after 24 h of incubation

The antimicrobial activity of titanium nanotubes has been explained in many ways. It was reported that the introduction of titanium nanoparticulates could damage the outer cell membranes of the prokaryotic yeast causes cell death. Others have reported that the oxides of titanium depolarize the membrane, release the intracellular

glucose and trehalose, a decrease plasma membrane fluorescence with increasing concentrations of the nanotube. Venkatesan *et al.* observed the titanium nanoparticle treated *C.albicans* biofilm through a transmission electron microscope. The presence of pits in the cell wall and pores in the plasma membrane demonstrates that the titanium nanoparticles destruct the fungal membrane integrity and inhibit the normal budding process (Venkatesan et al. 2014).

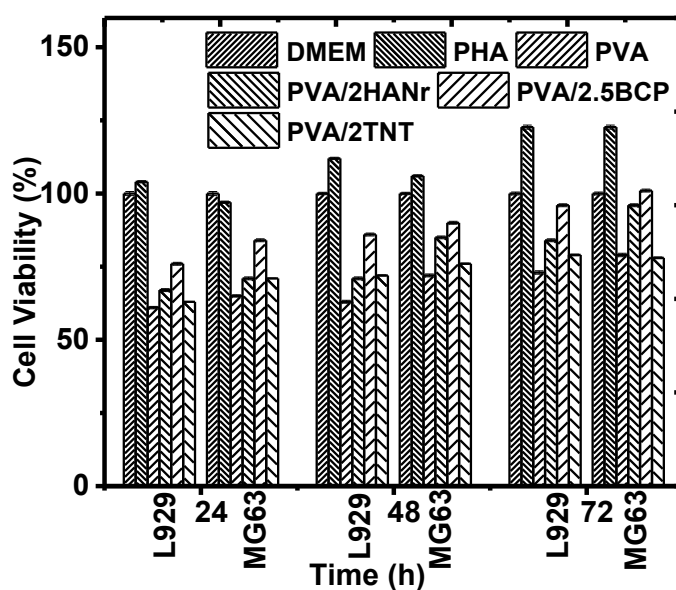


**Fig. 5.10** L929 and MG63 cell viability of on PVA, PVA/2HANr, PVA/2.5BCP and PVA/2TNT composite hydrogel after 24, 48 and 72 h of incubation.

### 5.7.7 Measurement of cytotoxicity

The cytocompatibility of the composite hydrogel towards L929 mouse fibroblast and MG63 human osteoblast-like cells was evaluated by using an MTT assay. The cell viability of cells on PVA, PVA/2HANr, PVA/2.5BCP and PVA/2TNT composite hydrogel was estimated after 24, 48 and 72 h of incubation. These viability reports were compared with the DMEM (control) and Phytohaemagglutinin, PHA (viability under ideal condition). As expected, the bioceramic reinforcement nanohydroxyapatite and tricalcium phosphate enhance the cell viability in comparison with pure PVA hydrogel and the introduction of titanium dioxide nanotube did not shows a noticeable improvement in cell viability. This is because the release of  $\text{Ca}^{2+}$  and  $\text{PO}_4^{3-}$  bioactive ions which anchor chitosan hydrogel might afford a tissue-like environment for cell adhesion and proliferation. In the case of TNT reinforcement, the reactive oxygen species generation controls the cell viability. Fig. 5.10 shows the

percentage cell viability of L929 and MG63 cells after 24, 48 and 72 h. It was found that the viability in all the samples increases with increasing time confirms hydrogels did not produce any toxic element. As per ISO standards for biocompatibility evaluation, composite hydrogel did not show any cytotoxicity for both L929 and MG63 cells since its relative viability was more than 70%.

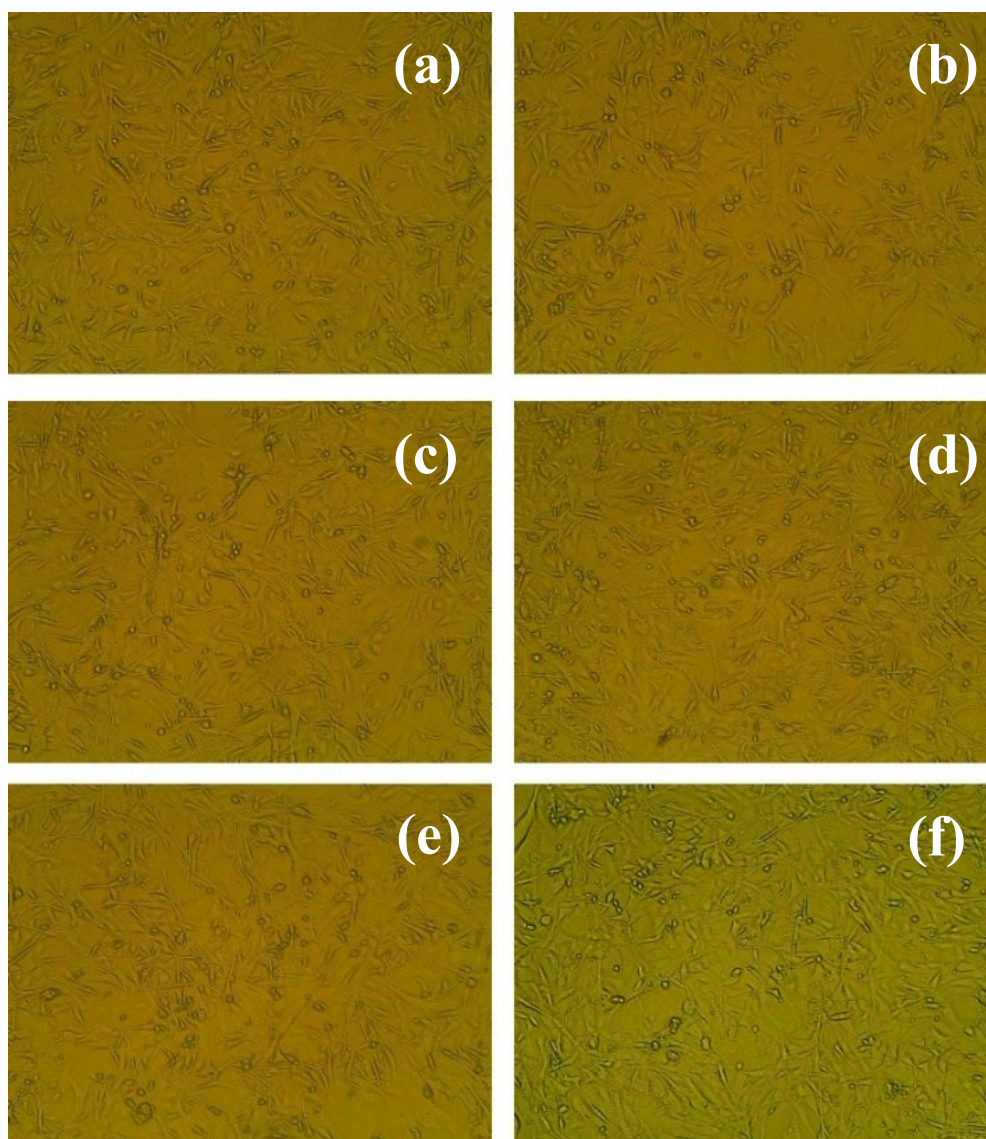


**Fig. 5.11** Inverted microscope images of MG63 cell viability towards DMEM, PHA,PVA, PVA/2HANr, PVA/2.5BCP and PVA/2TNT after 72 h of incubation.

The inverted microscopic images provide a preliminary understanding of the cellular response to hydrogels. These images confirm that both L929 and MG63 cells can adhere and proliferate well on the hydrogel scaffold and their proliferation rate increases with the culture time.

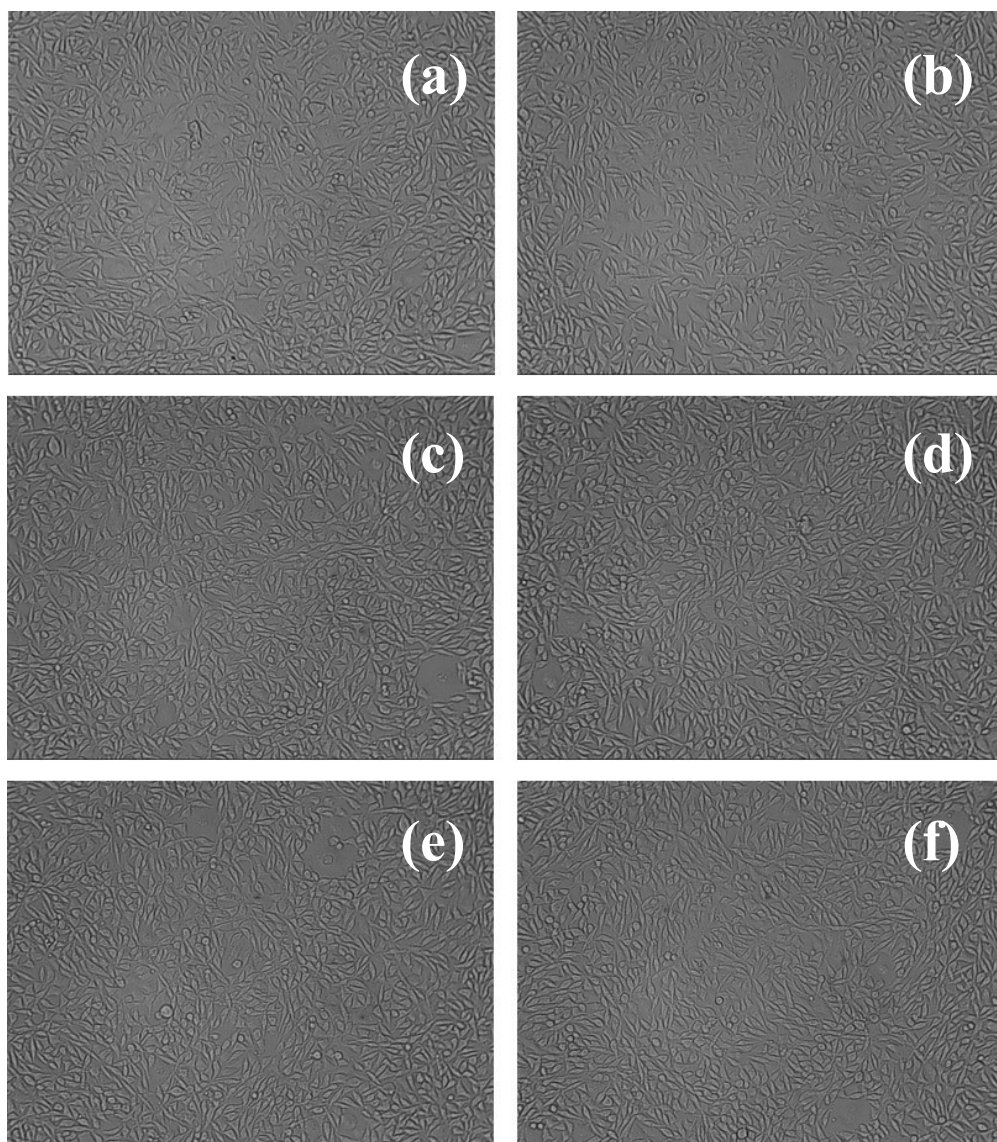


**Fig. 5.12** Inverted microscope images of L929 cell viability towards DMEM, PHA, PVA, PVA/2HANr, PVA/2.5BCP and PVA/2TNT after 72 h of incubation.

## CHAPTER 6

### DEVELOPMENT OF HYDROXYAPATITE SCAFFOLDS FOR BONE TISSUE ENGINEERING

---

This chapter briefly describes the method of developing the nanohydroxyapatite scaffolds for bone tissue engineering. The nanohydroxyapatite was synthesized using a biowaste cuttlefish bone through a mechanochemical method without using any toxic surfactants as explained in the materials and methods of chapter 3. The porous scaffolds were prepared by powder metallurgy process using sodium bicarbonate as a pore-forming agent. The samples were characterized by scanning electron microscopic images to analyze the pore structure and morphology. The compressive mechanical strength was measured in a universal testing machine and *in vitro* biodegradability after 7, 14 and 28 days were evaluated by measuring the weight loss. The antimicrobial potency of the scaffold against *Escherichia coli*, *Staphylococcus aureus* bacteria's and *Candida albicans* fungi was evaluated and compatibility towards MG 63 osteoblast-like and L929 fibroblast cells growth on the scaffold was evaluated.

The treatment of bone defects remains a challenge in current clinical practice. Present clinical procedures such as autograft, allograft and xenograft are limited its application due to donor deficiency and risk of immune rejection. There is no doubt about the increasing demand for artificial bone implant material. Human bone mainly consists of 10-20% water, 5-15% collagen fibers, proteins and inorganic salts and the remaining 60-70% minerals such as hydroxyapatite. Therefore, hydroxyapatite is considered as the matrix material for ceramic composite scaffolds for bone tissue engineering. For hydroxyapatite synthesis, several technics such as hydrothermal, sol-gel, polymer assisted, electrodeposition technics are used for bulk production. However, the use of chemicals during synthesis hinders its cytocompatibility *in vivo*. The use of natural resources such as animals (porcine bones) and fishbone has been extensively used since it is simple, inexpensive and produces a large quantity of hydroxyapatite. On the other hand, the use of these bio-wastes helps in reducing disposal problems.



The development of reliable, fast and cost-effective hydroxyapatite productive technics are thus of great significance in the biomedical community. In the present work cuttlefish bones are used for nanohydroxyapatite synthesis. It contains 90-95% calcium carbonate crystals stabilized by a protein matrix. An orthophosphoric acid was used to maintain the Ca/P stoichiometric molar ratio of 1.667. The hydroxyapatite particulates was pelletized and scaffolds were developed for physical and mechanical characterisation.

### 6.1 Scaffold preparation

For scaffold preparation, the required quantity of the nanohydroxyapatite was estimated to prepare a cylindrical sample (10 mm diameter and 20 mm height). The porous nanohydroxyapatite scaffold was prepared by powder metallurgy process. In brief, nHAp particulates was mixed with various percentages (20, 40, 50 and 60%) of sodium bicarbonate as a pore-forming agent. The mixture was pressed using powder compaction die under 70 MPa. The samples were named as nHAp20 to nHAp60 (nHAp20 refers to scaffold having 20% pore-forming agent). Before compaction, zinc stearate was applied to the die wall and punch surface as a lubricant, which eliminates the friction during the ejection of the sample from the die. Then the samples were heated to 200 °C to remove the pore-forming agent. Finally, scaffolds were sintered in a vacuum at 0.001 Pa at 800 °C for 2 h. The preparation process flow chart is as shown in Fig. 6.1.

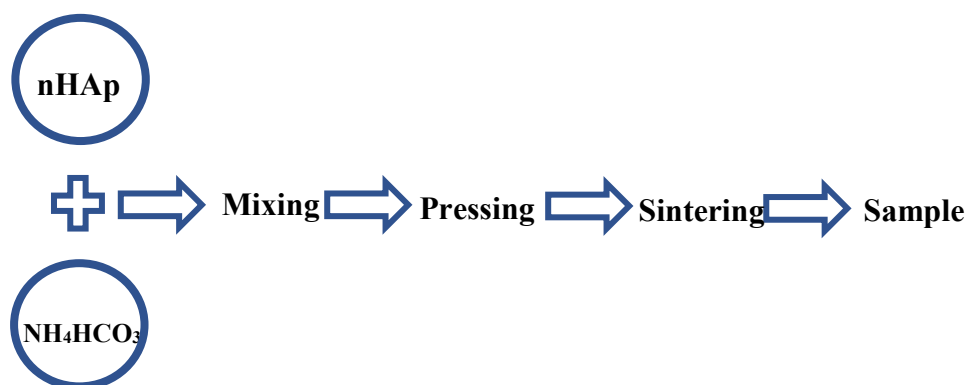


**Fig. 6.1** Flow chart for the preparation of hydroxyapatite scaffolds.

## 6.2 Nanohydroxyapatite scaffold characterization

### 6.2.1 Morphological characterization

The surface morphology and porous structure of the scaffold were evaluated by scanning electron microscope images, SEM (JSM-6380LA, JOEL, Japan). The crystallinity and phase composition of the porous scaffold was determined by an X-ray diffractometer (Rigaku, MiniFlex 600) in the range 20-80 ° at a rate of 2°/min. The chemical composition of the NHAp was determined by Fourier transform infrared spectroscopy (Bruker alpha) at an operating wavelength of 4000-500 cm<sup>-1</sup> with a resolution of 8 cm<sup>-1</sup>.

### 6.2.2 Physical and Mechanical characterization

The porosity of the hydroxyapatite scaffold was determined by the liquid displacement method as explained elsewhere (Y et al. 2019). The cylindrical samples (10 mm diameter and 20 mm height) were immersed in ethanol until no change in mass was observed. Then the samples were then removed from the medium and the final weight was measured (W<sub>2</sub>). Finally, samples were lyophilized and measured the dry weight (W<sub>1</sub>). The porosity was calculated as;

$$\text{Porosity} = \frac{(W_2 - W_1 - W_3)}{(W_2 - W_3)} \times 100 \dots\dots\dots (6.1)$$

Where W<sub>3</sub> is the weight of the deionized water after removal of the sample.

The adsorption potency of the nanohydroxyapatite scaffold was estimated by measuring the contact angle between the water droplet and the scaffold surface. A drop of water is set along the scaffold surface and once it reaches the equilibrium, the angle formed by the sample surface and the tangent to the drop profile on the drop edge was measured. The compressive mechanical strength of the cylindrical hydroxyapatite scaffold (10 mm diameter and 20 mm length) was measured using the universal testing machine (Mecmesin MultiTest 10-i, London) as per ASTM C 1424 – 99 with a loading rate of 0.5 mm/min. an elastic modulus was computed by measuring compressive stress and strain within the elastic limit.

### 6.2.3 Degradation studies

The *in vitro* degradation of the scaffold was measured by dipping the hydroxyapatite scaffold in 0.1 M phosphate buffer saline with lysozyme enzyme (0.5 mg/mL). Air trapped in the pores was removed by venting with the aid of a vacuum oven. The PBS solution was replaced with a new solution every week. Before the test, the initial weight of the scaffold was measured ( $W_i$ ). At regular intervals, the samples were removed, dried under vacuum at 37 °C and weight was measured ( $W_f$ ). The experiment was carried out for 11 months as per ASTM F 1635-04a. The weight loss ( $W_L$ ) of the hydrogel sample was calculated as;

$$W_L = \frac{(W_i - W_f)}{W_i} \times 100 \dots\dots\dots (6.2)$$

Where  $W_i$  and  $W_f$  are the weight of the hydrogel before and after soaking respectively.

#### 6.2.4 Microbial study

The microbes used in this study including standard strains of *E. Coli ATCC 25922*, *S. aureus ATCC 25923* and *C. albicans CCRC21538*. Nutrient agar and Nutrient Broth were procured from Sisco Research Laboratories, India and HiMedia Laboratories, India respectively. All the strains were incubated at 37 °C for 12 h.

#### 6.2.5 Growth inhibition test

The antimicrobial activity was evaluated according to the growth inhibition assay using the modified method explained elsewhere. In brief, 300 µL of nutrient broth and 50 µL of diluted bacterial or fungal culture were added to the 24 well plates and the initial absorbance was recorded at 600 nm in a Thermo scientific Multiscan® plate reader and considered an initial bacterial/fungal concentration. Then, triplicate nanohydroxyapatite pellets (10 mm diameter and 5 mm thick) were added to the respective well and incubated overnight at 37 °C. The inoculum was then monitored for changes in the absorbance at 600 nm ( $OD_{600}$ ). The well without any sample was considered as a control. The percentage growth compared to the control was calculated for each sample.

#### 6.2.6 Measurement of cytotoxicity

Cytotoxicity tests evaluate the biocompatibility of the material with potential for medical application. The cytocompatibility of the nanohydroxyapatite scaffold was assessed by determining the viability of the MG 63 osteoblast-like cells and L929 mouse fibroblast cells in response to the conditioned media using MTT assay. Briefly,

pellet samples (10 mm diameter, 5 mm thick) were sterilized in 70% ethanol followed by washing in a sterile PBS. Cells were seeded on the sample surface (20,000 cells/well) in a 24-well plate with DMEM supplemented with 10% FBS and incubated at 37 °C for 72 h in 5% CO<sub>2</sub>. Then, the media was replaced with 750 μL of 5 mg/mL MTT (4060 Himedia) in the PBS buffer and incubate for another 3 h. Finally, 100 μL of DMSO was added with gentle stirring in a gyratory shaker. The optical density (OD) of the media was measured at 570 nm to determine the cell viability, according to the equation:

$$\text{Cell viability (\%)} = \frac{\text{OD}_{\text{test}} - \text{OD}_{\text{blank}}}{\text{OD}_{\text{control}} - \text{OD}_{\text{blank}}} \dots\dots\dots (6.3)$$

Where, OD<sub>test</sub>, OD<sub>control</sub> and OD<sub>blank</sub> are the optical densities of cells incubated with hydrogel, DMEM, and DMEM without cells respectively.

### 6.3 Results and Discussion

The macroscopic images of the nanohydroxyapatite scaffolds are as shown in Fig. 6.2. All the scaffolds show porous structures with interconnected porosity which is needed for bone tissue engineering. The pore size and interconnectivity greatly influence the osteoconductivity of the bone scaffold. The combination of macro and micro pores is essential since micropores are essential to diffuse nutrients and removal of excretions, while macropores help in the growth and proliferation of the osteoblasts.

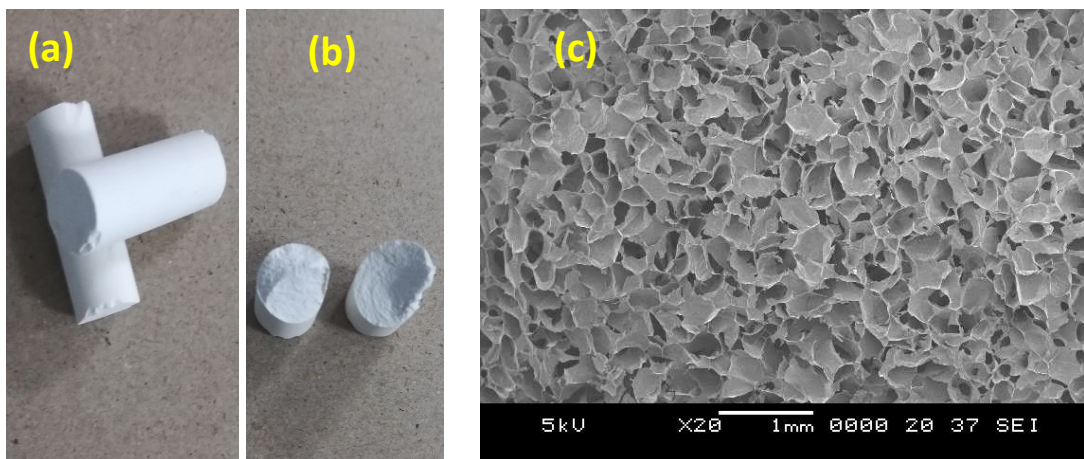


**Fig. 6.2** (a) Developed nHAp scaffolds (b) Fractured scaffold surface due to compression and (c) SEM image of the scaffolds shows the macroporous surface

In this research, the pore size and distribution in all the scaffold is uniform and pore size and porosity increases with the increasing content of pore-forming agent. When the  $\text{NH}_4\text{HCO}_3$  dosage was 20%, the porosity was  $12.1\pm 0.2\%$  and the pores are mainly closed pores which were unfavourable for nutrient transfer. As the dosage was increased to 50%, the porosity value reaches  $52.3\pm 0.9\%$  and the compression strength, average pore size was  $17\pm 0.5$  MPa and  $315\pm 2$   $\mu\text{m}$  respectively. As the concentration of the pore-forming agent rises further to 60%, the strength was declined to  $2.8\pm 0.3$  MPa which was much lower than the compressive strength of the human spongy bone (8-10 MPa) (Fan 2019). As the mass fraction of the ammonium bicarbonate increases, the porosity of the nHAp scaffold increases and demonstrates that the  $\text{NH}_4\text{HCO}_3$  directly controls the porosity. The mechanism of pore formation in the scaffolds is due to the decomposition of the ammonium bicarbonate when heated and leave behind the space (pores). At the low content of the pore-forming agent, the micropores were formed and mostly are closed pores. As the  $\text{NH}_4\text{HCO}_3$  dosage raises, the pore number increases and pore size increases when it intersects. In addition to the formation of pores during the sintering of nHAp, pores also can be formed by the gas volatilization due to the decomposition of the ammonium bicarbonate gas.

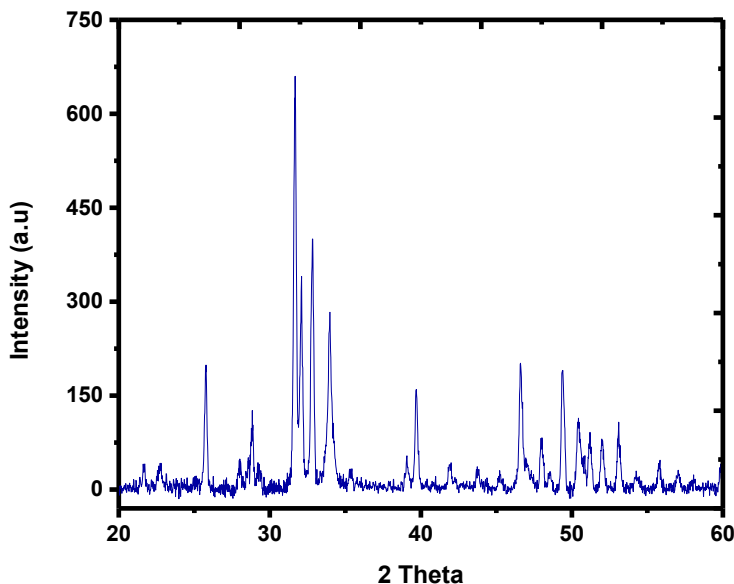


**Fig. 6.3** X-ray Diffractogram of nHAp scaffold

The crystallographic pattern of the nHAp scaffold is identical with the synthesized nanohydroxyapatite with a small trace of tricalcium phosphate confirmed from a sharp and intense peak ( $2\theta=25.8^\circ$ ). It could be due to the decomposition of

hydroxyapatite at higher sintering temperatures. Moreover, the developed tricalcium phosphate is beneficial for bone tissue engineering since it supports osteocytes formation thereby assist the new bone tissue formation. Similarly, the FTIR spectrum of the nHAp scaffold is similar to the FTIR spectrum of nanohydroxyapatite confirms that there is no trace of  $\text{NH}_4\text{HCO}_3$  and zinc stearate after sintering.

The surface adsorption mechanism is one of the prime requirements for scaffold materials that enable cell attachment. Earlier literature works have been reported that the maximal cell adhesion for osteoblast-like bone cells is for moderate hydrophilicity rather than higher or lower hydrophilicity. The optimum contact angle for better cell adhesion and proliferation of MG 63 osteoblast like-cells was estimated to be in the range of  $55^\circ$  to  $70^\circ$ . The developed hydroxyapatite scaffold shows the contact angle in the above range signifies these scaffolds support cell adhesion, proliferation and dedifferentiation *in vivo*.

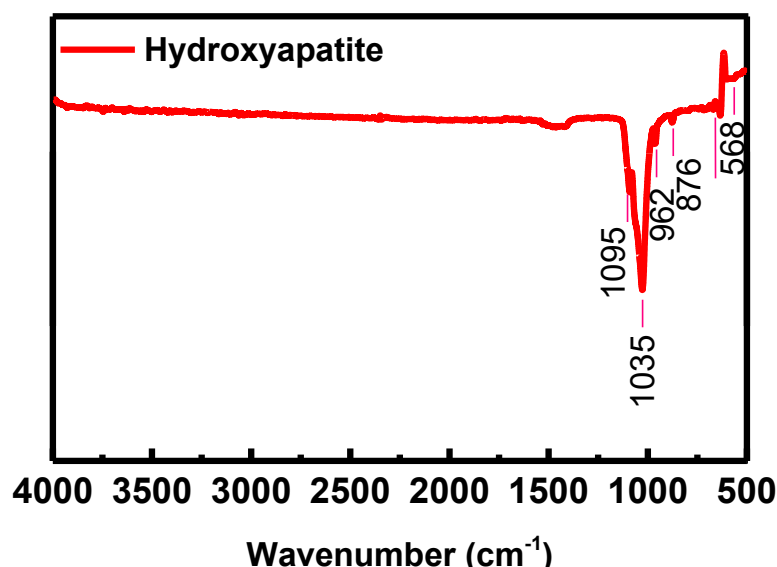


**Fig. 6.4** FTIR spectrum of nHAp scaffold

The mechanical stiffness of the scaffold materials is crucial to avoid the stress mismatch at the tissue scaffold interface. During walking or running, bones continuously undergoing compression rather than tension or shear. Therefore, the compression test was performed on the nHAp scaffold with a loading rate of 0.5 mm/min. As expected, the compression strength and modulus were decreases with increasing porosity. The composite scaffold having 50% of  $\text{NH}_4\text{HCO}_3$  shows an optimum compression strength of  $17.0 \pm 0.5$  MPa and compression modulus of  $111 \pm 2$

with an average porosity of  $52.3 \pm 1.2$  %. These values are very close to the compression strength of human spongy bones which is in the range of 5-11 MPa (Fan et al., 2019).

The degradation study of biomaterials reveals the stability of the scaffold *in vivo*. If the degradation rate is too high, then it deteriorates before the completion of the healing process. On the other hand, if the degradation rate is too low, then osteoclasts are unable to break down the bone tissue resulting in fails to transfer calcium from bone tissue to the blood. All mammalian body needs continuous bone remodelling. In the bone remodelling mechanism, the bone continuously maintains bone strength and ion homeostasis by replacing the discrete part of the old bone with newly synthesized bundles of the proteinaceous matrix.

**Table 6.1** Physico-mechanical properties of nHAp scaffolds

<b>Sample</b>	<b>Average porosity (%)</b>	<b>Contact angle (°)</b>	<b>Compression strength (MPa)</b>	<b>Compression Modulus (MPa)</b>
nHAp20	$12.1 \pm 1.5$	$42.5 \pm 1.2$	$63.3 \pm 2.2$	$870 \pm 2$
nHAp40	$29.3 \pm 1.2$	$49.2 \pm 1.4$	$39.2 \pm 1.3$	$480 \pm 3$
nHAp50	$52.3 \pm 0.9$	$51.2 \pm 1.8$	$17.0 \pm 0.5$	$111 \pm 2$
nHAp60	$75.2 \pm 1.3$	$73.2 \pm 1.2$	$2.8 \pm 0.3$	$9 \pm 0.8$

The degradation rate of nanohydroxyapatite scaffolds was affected by various factors such as molecular weight, degradation time, pH, temperature and catalytic ions or molecules. Fig. 6.5 shows the molecular weight loss as a function of time. The degradation mechanism happened in three stages; low degradation for 1<sup>st</sup>- 4<sup>th</sup> weeks, fast degradation from 4<sup>th</sup> - 6<sup>th</sup> week and medium degradation from 6<sup>th</sup> -11<sup>th</sup> week. The slow degradation, in the beginning, could be due to the surface erosion mechanism of catalytic molecules. In the surface erosion mechanism, the enzymes in the buffer solution try to erode the surface while the core part of the material is unchanged. As time proceeds, the enzymes penetrate deep into the material and initiates bulk erosion. During this, the degree of crystallinity controls the degradation rate. Once the amorphous phase degrades completely, the rate stabilizes which was observed from the 6<sup>th</sup> -11<sup>th</sup> week.

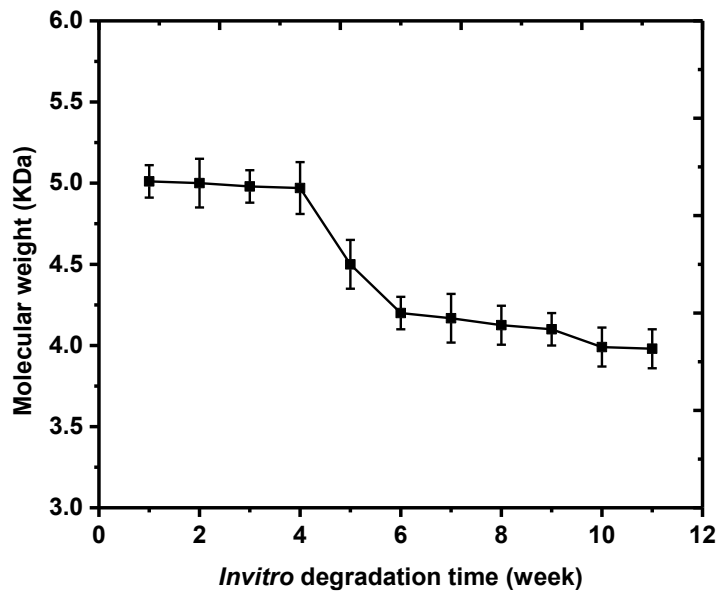


**Fig. 6.5** Molecular weight change (KDa) with in vitro degradation time of nHAp scaffold for 11-week observation at 37 °C.

### 6.3.1 Biological characterization

The antimicrobial efficacy evaluation of bone scaffolds is crucial to resist post-surgical infection and biofilm formation. The antimicrobial activity of the nHAp50 scaffold at 37 °C was evaluated against bacterial strains *Escherichia coli*, *Staphylococcus aureus* and *Candida albicans* fungi.

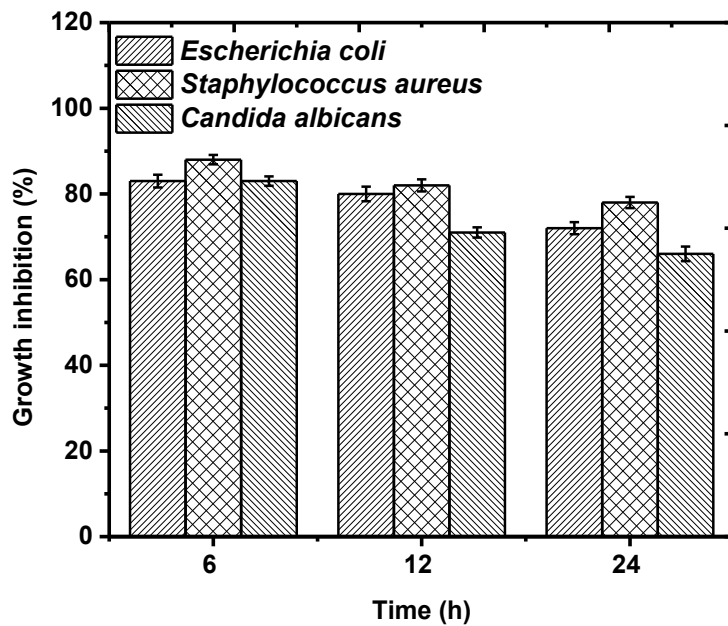


**Fig. 6.6** Growth inhibition of gram-negative *Escherichia coli*, gram-positive *Staphylococcus aureus* and *Candida albicans* fungi after 6, 12 and 24 h of incubation



As expected, nHAp was more effective for *Escherichia coli* than *Staphylococcus aureus* since 8% more inhibition was found after 24 h of incubation. This could be explained by the difference in the cellular cladding of gram-negative (*Escherichia coli*) and gram-positive (*Staphylococcus aureus*) bacteria. Typically, gram-negative microbes have a thin cell wall structure consisting of peptidoglycans and lipopolysaccharide (Rajakumar et al. 2012). Whereas, gram-positive bacteria's like *Staphylococcus aureus* has a thick layer of lipoteichoic acid which resist cytoplasmic leakage. On the other hand, the  $\text{Ca}^{2+}$  ions of hydroxyapatite destabilize the cell membranes by reactive oxygen species (ROS) generation. The antifungal activity is distinct; the ions  $\text{PO}_4^{3-}$  ions of HANr can break down the outer membranes by oxidizing phospholipids cause cytoplasmic leakage leading to the death of the pathogen.

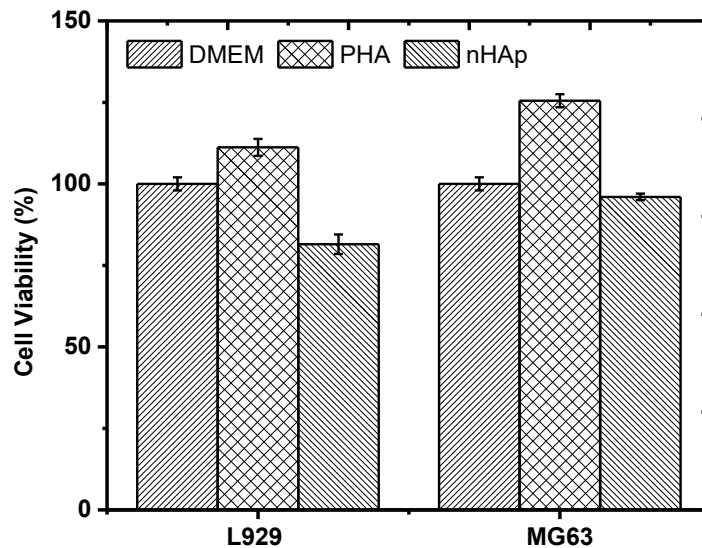


**Fig. 6.7** L929 fibroblast and MG 63 osteoblast-like cell viability on nHAp scaffold after 72 h of incubation

The cell viability of the nHAp scaffolds towards L929 mouse fibroblasts and MG 63 osteoblast-like cells was evaluated by MTT assay. The viability of these cells on DMEM, PHA and nHAp scaffolds are as shown in Fig. 6.7. As expected, cell stimulator PHA-treated scaffolds show the highest cell viability of 111 and 125% for L929 and MG63 cells respectively. The nHAp scaffolds show better proliferation (81.5 and 96 %) after 72 h of incubation. In composite hydrogel, the release of calcium and phosphate ions of hydroxyapatite increases the local concentration of  $\text{Ca}^{2+}$  and  $\text{PO}_4^{3-}$  ions, thus stimulates the bone mineral formation on the counter surface of calcium phosphate. Besides, it helps to adsorb the extracellular matrix proteins, thus enhances

cell proliferation. As per ISO standards for biocompatibility evaluation, composite hydrogel not showing any toxicity towards incubated cells since its relative viability was more than 70%. The inverted microscope images of both the cells after 72 h of culture are as shown in Fig. 6.8. It can be seen from the images that scaffolds assist the cell attachment and proliferation and the results are consistent with the MTT assay. From this, it was confirmed that the scaffolds have favorable antimicrobial activity with excellent cell viability after 72 h of incubation.

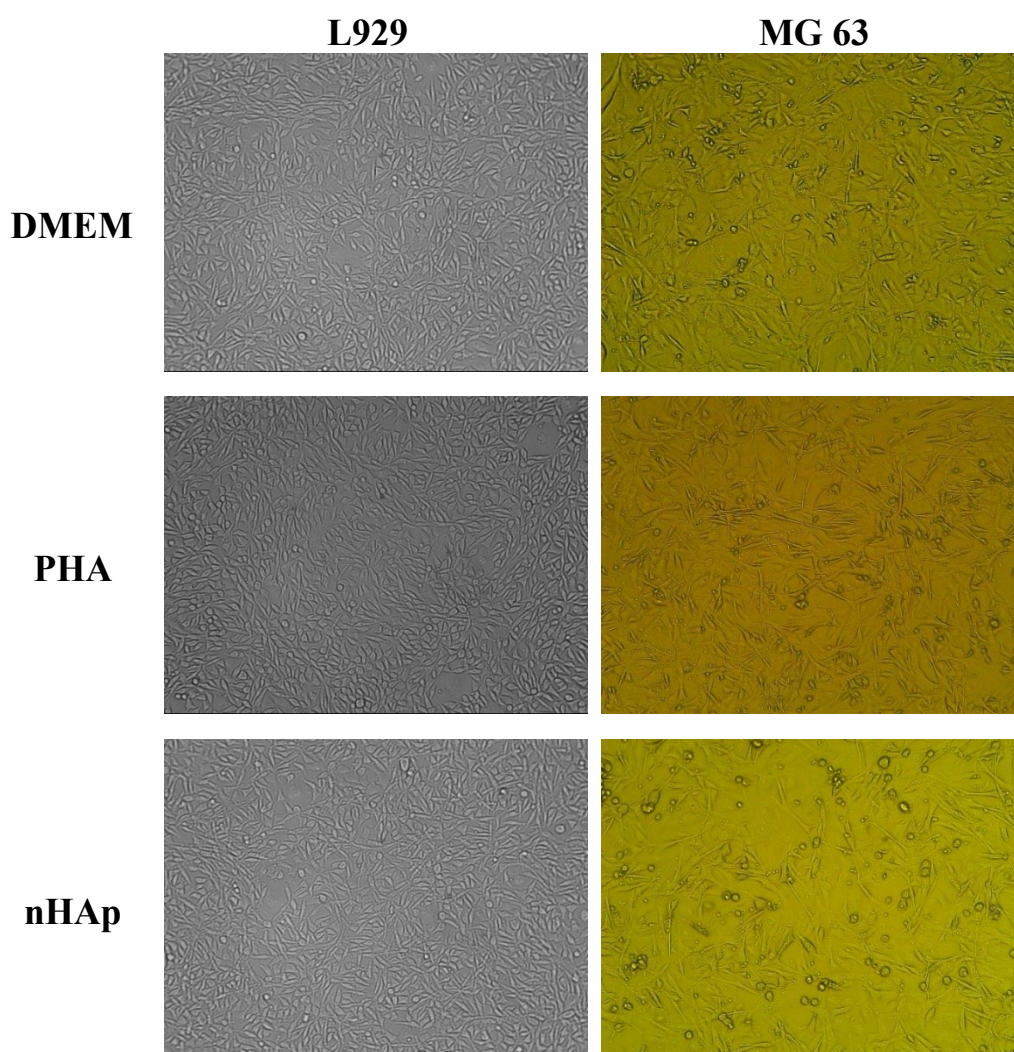


**Fig. 6.8** Inverted microscope images of L929 (left) and MG 63 (right) cell viability on DMEM, PHA and nHAp after 72 h of incubation



## CHAPTER 7

### CONCLUSION AND SCOPE FOR THE FUTURE WORK

---

#### 7.1 Contribution to the research work

The treatment of articular cartilage damage is a major task in the medical science of orthopedics. The developed nanocomposite robust hydrogel possess the ability to form multifunctional cartilage grafts since they possess polymeric swelling ability upon immersion in an aqueous phase similar to human tissue. Polymeric hydrogels are capable of physiological swelling and greasing, and they possess the mechanical behavior required for use as articular cartilage substitutes. The chondrogenic phenotype of these materials may be enhanced by embedding living cells. Artificial hydrogels fabricated from biologically derived and synthesized polymeric materials are also used as tissue-engineering scaffolds; with their controlled degradation profiles, the release of stimulatory growth factors can be achieved. In order to make use of these hydrogels, cartilage implants were formulated in the laboratory to demonstrate the bionic mechanical behaviors of physiological cartilage. This research discusses the development concerning the use of polymeric hydrogels for substituting injured cartilage tissue and assisting tissue growth.

#### 7.2 Conclusions

In the present work bioceramic, nanoparticles were synthesized and then reinforced with natural and synthetic polymers for the development of composite hydrogels for cartilage tissue implants.

Based on the above observations it can be concluded that,

- The Nanohydroxyapatite and Bi-phasic calcium phosphate were synthesised from bio-waste cuttlefish bone successfully. These bioceramics show one-dimensional nanorod morphology. Also, Titanium dioxide nanotubes were developed from titanium dioxide nanoparticles, and the morphology was confirmed with Transmission Electron Microscope (TEM)
- The chitosan and polyvinyl alcohol composite hydrogel were developed by reinforcing the prepared bioceramics through the freeze-thaw technique without

adding any toxic surfactants. The physical, mechanical, rheological and biological properties required for the cartilage applications are evaluated.

The composite hydrogel are having porous morphology with interconnected porosity which is essentially significant for cartilage implants to transfer nutrients and metabolic wastes in the biological environment. The introduction of bioceramic reinforcement reduces the porosity without collapsing the organized porous network and thus increases the mechanical strength. The swelling and water holding potency of the hydrogels related to the amorphous region and free hydroxyl groups in the polymer network. The increased swelling reduces the mechanical strength and it can be controlled by optimizing the reinforcements. Thus, it develops additional hydrogen bonds which restrict the free expansion of the polymer chain. This was confirmed by the shifting of the absorption spectrum towards lower wavenumber in the FTIR analysis. The biocompatibility of the hydrogel is primarily influenced by surface characteristics particularly surface topography, surface energy and wettability. The developed hydrogel surfaces show neither hydrophilic nor hydrophobic thus supports cell adhesive serum protein such as fibronectin and fibrinogen adhesion on the surface.

The compression curves of the hydrogels correspond to the behaviour of non-linear and viscoelastic solid similar to human articular cartilage. The maximum compression modulus value of the CS and PVA composite hydrogel is more than those of healthy cartilage, which varies between 0.1 to 2 MPa. The storage modulus of all the hydrogels are much higher than the loss modulus, demonstrates they are elastic dominant rather than fluid-like structure.

The antimicrobial activity of composite hydrogel was satisfactory, the reinforcements are effective for both gram-negative and gram-positive bacteria's and fungal commensal organisms. The ions of nanoparticulates which interact with the proteins of the cell membrane, penetrates through it and damages the DNA by producing ROS, causes the death of microorganisms. Thus it reduces the biofilm formation on the implant material. Besides, the cell viability towards the L929 fibroblasts and the MG63 osteoblast cells demonstrates that these hydrogels are non-toxic and supports cell adhesion, proliferation and differentiation based on

more than 75% cell viability after 72 h of culture. Collectively, this study proves that these composite hydrogels are substitute materials for next-generation cartilage tissue implants.

### **7.3 Scope for the future work**

We predict that future research on hydrogels will move towards lower cost and more specificity. The advanced *in vitro* biological studies such as chondrocyte viability, alkaline phosphate activity, gene expression and RTPCR, *in vivo* animal studies be the significant obstacle to research. Since its application is in the diarthroidal joint, advanced bio-tribological reseearch remains the focus of the future research. To achieve this, we can discover more bioactive hydrogel materials. Alternatively focus on the work of structural modification of polymers, after all, structural limitations remains one of the main challenges of future of research. Many factors affect the production of hydrogels – the production conditions will vary greatly on the crosslinking materials. Besides, optimization of the production process in terms of polymer stability, processability, and solubility may also be a significant problem to research. We hope to bring together experts from different fields (chemistry, physics, materials, biomedical engineering, pharmacy, etc) to solve the problem as mentioned above through cross disciplinary dialogue.



## REFERENCES

- Agrawal, G., Negi, Y. S., Pradhan, S., Dash, M., and Samal, S. K. (2017). Wettability and contact angle of polymeric biomaterials. *Characterization of Polymeric Biomaterials*, 4(1), 1357–1381.
- Amirthalingam, N., Deivarajan, T., and Paramasivam, M. (2019). “Mechanochemical synthesis of hydroxyapatite using dolomite.” *Materials Letters*, 254, 379–382.
- Bendtsen, S. T., Quinnell, S. P., and Wei, M. (2017). “Development of a novel alginate-polyvinyl alcohol-hydroxyapatite hydrogel for 3D bioprinting bone tissue-engineered scaffolds.” *Journal of Biomedical Materials Research - Part A*, 105(5), 1457–1468.
- Bensalah, H., Bekheet, M. F., Alami Younssi, S., Ouammou, M., and Gurlo, A. (2018). “Hydrothermal synthesis of nanocrystalline hydroxyapatite from phosphogypsum waste.” *Journal of Environmental Chemical Engineering*, 6(1), 1347–1352.
- Bhowmick, S., and Koul, V. (2016). “Assessment of PVA/silver nanocomposite hydrogel patch as antimicrobial dressing scaffold: Synthesis, characterization and biological evaluation.” *Materials Science & Engineering C*, 59, 109–119.
- Briant, P., Beville, S., and Andriacchi, T. (2015). “Cartilage Strain Distributions are Different under the Same Load in the Central and Peripheral Tibial Plateau Regions.” *Journal of Biomechanical Engineering*, 137, 1–7.
- Buwalda, S. J., Boere, K. W. M., Dijkstra, P. J., Feijen, J., Vermonden, T., and Hennink, W. E. (2014). “Hydrogels in a historical perspective: From simple networks to smart materials.” *Journal of Controlled Release*, 190, 254–273.
- Chen, J., Liu, J., Deng, H., Yao, S., and Wang, Y. (2019). “Regulatory synthesis and characterization of hydroxyapatite nanocrystals by a microwave-assisted hydrothermal method.” *Ceramics International*, 132, 1–9.
- Chen, K., Zhang, D., Yang, X., Cui, X., Zhang, X., and Wang, Q. (2016). “Research on torsional friction behaviour and fluid load support of PVA / HA composite hydrogel.” *Journal of the Mechanical Behavior of Biomedical Materials*, 62, 182–194.
- Deb, P., Barua, E., Lala, S. Das, and Deoghare, A. B. (2019). “Synthesis of



hydroxyapatite from Labeo rohita fish scale for biomedical application.” *Materials Today: Proceedings*, 15, 277–283.

Delmar, K., and Bianco-Peled, H. (2015). “The dramatic effect of small pH changes on the properties of chitosan hydrogels crosslinked with genipin.” *Carbohydrate Polymers*, 127, 28–37.

Doulabi, A. H., Mequanint, K., and Mohammadi, H. (2014). “Blends and nanocomposite biomaterials for articular cartilage tissue engineering.” *Materials*, 7(7), 5327–5355.

Efron, N., and Maldonado-Codina, C. (2011). Development of contact lenses from a biomaterial point of view - materials, manufacture, and clinical application. *Comprehensive Biomaterials*, 85, 686-714.

Fan, X. (2019). “Preparation and performance of hydroxyapatite/Ti porous biocomposite scaffolds.” *Ceramics International*, 45(13), 16466–16469.

Farzinfar, E., and Paydayesh, A. (2019). “Investigation of polyvinyl alcohol nanocomposite hydrogels containing chitosan nanoparticles as a wound dressing.” *International Journal of Polymeric Materials and Polymeric Biomaterials*, 68(11), 628–638.

Ferro, A. C., and Guedes, M. (2019). “Mechanochemical synthesis of hydroxyapatite using cuttlefish bone and chicken eggshell as calcium precursors.” *Materials Science and Engineering C*, 97, 124–140.

Frame, J. W. (1987). “Hydroxyapatite as a biomaterial for alveolar ridge augmentation.” *International Journal of Oral and Maxillofacial Surgery*, 16(6), 642–655.

Ge, X., Ren, C., Lu, X., Li, Z., Chen, G., Wang, K., Ren, F., Wang, Q., Wang, M., An, X., and Qian, B. (2019). “Surfactant-free electrochemical synthesis of fluoridated hydroxyapatite nanorods for biomedical applications.” *Ceramics International*, 45(14), 17336–17343.

Geng, H. (2018). “A one-step approach to make cellulose-based hydrogels of various

- transparency and swelling degrees.” *Carbohydrate Polymers*, 186, 208–216.
- Gofman, I. V., and Buyanov, A. L. (2017). “Unusual effect evidenced at the investigations of the mechanical behaviour of composite hydrogels under cyclic compression.” *Journal of the Mechanical Behavior of Biomedical Materials*, 71, 238–243.
- Gonzalez, J. S., and Alvarez, V. A. (2014). “Mechanical properties of polyvinylalcohol/hydroxyapatite cryogel as potential artificial cartilage.” *Journal of the Mechanical Behavior of Biomedical Materials*, 34, 47–56.
- Han, M. E., Kang, B. J., Kim, S. H., Kim, H. D., and Hwang, N. S. (2017). “Gelatin-based extracellular matrix cryogels for cartilage tissue engineering.” *Journal of Industrial and Engineering Chemistry*, 45, 421–429.
- Hench, L. L., Splinter, R. J., Allen, W. C., and Greenlee, T. K. (1971). “Bonding mechanisms at the interface of ceramic prosthetic materials.” *Journal of Biomedical Materials Research*, 5(6), 117–141.
- Hildebrand, H. F. (2013). “Biomaterials - a history of 7000 years.” *BioNanoMaterials*, 14(3–4), 119–133.
- Homayouni, A., Ehsani, M. R., Azizi, A., Yarmand, M. S., and Razavi, S. H. (2007). “Effect of lecithin and calcium chloride solution on the microencapsulation process yield of calcium alginate beads.” *Iranian Polymer Journal*, 16(9), 597–606.
- Huebsch, N., and Mooney, D. J. (2009). “Inspiration and application in the evolution of biomaterials.” *Nature*, 462(7272), 426–432.
- Hussin, M. H., Husin, N. A., Bello, I., Othman, N., Bakar, M. A., and Mohamad Haafiz, M. K. (2018). “Isolation of microcrystalline cellulose (MCC) from oil palm frond as a potential natural filler for PVA-LiClO<sub>4</sub> polymer electrolyte.” *International Journal of Electrochemical Science*, 13(4), 3356–3371.
- Ibrahim, D. M., Kakarougas, A., and Allam, N. K. (2017). “Recent advances on electrospun scaffolds as matrices for tissue-engineered heart valves.” *Materials Today Chemistry*, 5, 11–23.

Jaiswal, M. (2010). "Polycaprolactone diacrylate crosslinked biodegradable semi-interpenetrating networks of polyacrylamide and gelatin for controlled drug delivery." *Biomed. Mater.* 5, 1-13.

Jung, A., Makkar, P., Amirian, J., and Lee, B. (2018). "A novel hybrid multichannel biphasic calcium phosphate granule-based composite scaffold for cartilage tissue regeneration." *Journal of Biomaterials Applications*, 32(6), 775–787.

Kanimozhi, K., Khaleel Basha, S., Sugantha Kumari, V., Kaviyarasu, K., and Maaza, M. (2018). "In vitro cytocompatibility of chitosan/PVA/methylcellulose – Nanocellulose nanocomposites scaffolds using L929 fibroblast cells." *Applied Surface Science*, 449, 574–583.

Kihlström Burenstam Linder, L., Birgersson, U., Lundgren, K., Illies, C., and Engstrand, T. (2019). "Patient-Specific Titanium-Reinforced Calcium Phosphate Implant for the Repair and Healing of Complex Cranial Defects." *World Neurosurgery*, 122, 399–407.

Kim, S. (2018). "Competitive Biological Activities of Chitosan and Its Derivatives: Antimicrobial, Antioxidant, Anticancer, and Anti-Inflammatory Activities." *International Journal of Polymer Science*, 125, 1-13.

Koizumi, H., Takeuchi, Y., Imai, H., Kawai, T., and Yoneyama, T. (2019). "Application of titanium and titanium alloys to fixed dental prostheses." *Journal of Prosthodontic Research*, 63(3), 266–270.

Kommareddy, S., Shenoy, D. B., and Amiji, M. M. (2007). "Gelatin Nanoparticles and Their Biofunctionalization." *Nanotechnologies for the Life Sciences*, 15, 330-352.

Kumar, R., Isloor, A. M., Ismail, A. F., Rashid, S. A., and Ahmed, A. Al. (2013). "Permeation, Antifouling and desalination performance of TiO<sub>2</sub> nanotube incorporated PSf/CS blend membranes." *Desalination*, 316, 76–84.

Le, P., Lee, Y., Thanh, T., Thi, H., Min, K., and Dong, K. (2018). "Catechol-rich gelatin hydrogels in situ hybridizations with silver nanoparticle for enhanced antibacterial activity." *Materials Science & Engineering C*, 92, 52–60.

- Lee, K., Weir, M. D., Lippens, E., Mehta, M., Wang, P., Duda, G. N., Kim, W. S., Mooney, D. J., and Xu, H. H. K. (2014). "Bone regeneration via novel macroporous CPC scaffolds in critical-sized cranial defects in rats." *Dental Materials*, 30(7), 199–207.
- Li, J., Qin, L., Yang, K., Ma, Z., Wang, Y., Cheng, L., and Zhao, D. (2019). "Materials evolution of bone plates for internal fixation of bone fractures, a review." *Journal of Materials Science & Technology*. 16, 1-17.
- Lin, Y., Huang, S., Zou, R., Gao, X., Ruan, J., Weir, M. D., Reynolds, M. A., Qin, W., Chang, X., Fu, H., and Xu, H. H. K. (2019). "Calcium phosphate cement scaffold with stem cell co-culture and prevascularization for dental and craniofacial bone tissue engineering." *Dental Materials*, 35(7), 1031–1041.
- Liu, L., Wu, Y., Xu, C., Yu, S., Wu, X., and Dai, H. (2018). "Synthesis, Characterization of Nano- $\beta$ -Tricalcium Phosphate and the Inhibition on Hepatocellular Carcinoma Cells." *Materials Science & Engineering C*, 59, 51–62.
- Liu, M., Zeng, X., Ma, C., Yi, H., Ali, Z., Mou, X., Li, S., Deng, Y., and He, N. (2017). "Injectable hydrogels for cartilage and bone tissue engineering." *Bone Research*, 5, 17014.
- Liu, Y., Cai, Z., Sheng, L., Ma, M., and Xu, Q. (2019). "Influence of nano-silica on inner structure and performance of chitosan-based films." *Carbohydrate Polymers*, 212, 421–429.
- Ma, D., Wang, Y., and Dai, W. (2018). "Silk fibroin-based biomaterials for musculoskeletal tissue engineering." *Materials Science and Engineering C*, 89(23), 456–469.
- Mahmood, T. A., Groot, K. De, Blitterswijk, C. A. Van, and Barre, F. (2008). "Advanced biomaterials for skeletal tissue regeneration: Instructive and smart functions." *Materials Science and Engineering R*, 59, 38–71.
- Matsiko, A., Levingstone, T. J., and O'Brien, F. J. (2013). "Advanced strategies for articular cartilage defect repair." *Materials*, 6(2), 637–668.

McMahon, S., Bertollo, N., Cearbhaill, E. D. O., Salber, J., Pierucci, L., Duffy, P., Dürig, T., Bi, V., and Wang, W. (2018). “Bio-resorbable polymer stents: a review of material progress and prospects.” *Progress in Polymer Science*, 83, 79–96.

Ming, J., Hao, J., Chun, S., Hua, C., Chin, C., Chiang, K., Chen, C., Shao, K., Wen, S., and Shyan, J. (2016). “Cell proliferation on PVA / sodium alginate and PVA / poly (  $\gamma$ -glutamic acid ) electrospun fibre.” *Materials Science & Engineering C*, 66, 170–177.

Nasker, P., Mukherjee, M., Kant, S., Tripathy, S., Sinha, A., and Das, M. (2018). “Fluorine substituted nano-hydroxyapatite: Synthesis, bioactivity and antibacterial response study.” *Ceramics International*, 44(17), 22008–22013.

Offer, G., Knight, P., Jeacocke, R., Almond, R., Cousins, T., Elsey, J., Parsons, N., Sharp, A., Starr, R., and Purslow, P. (1989). “The structural basis of the water-holding, appearance and toughness of meat and meat products.” *Food Microstructure*, 8,(1), 151–170.

Oliveira, W. F., Silva, G. M. M., Cabral, P. E., Fontes, A., Oliveira, M. D. L., Andrade, C. A. S., Silva, M. V., Coelho, L. C. B. B., Machado, G., and Correia, M. T. S. (2018). “Titanium dioxide nanotubes functionalized with Cratylia Molli's seed lectin, Cramoll ,enhanced osteoblast-like cells adhesion and proliferation.” *Materials Science & Engineering C*, 90(May), 664–672.

Pal, A., Paul, S., Choudhury, A. R., Balla, V. K., Das, M., and Sinha, A. (2017a). “Synthesis of hydroxyapatite from Lates calcarifer fishbone for biomedical applications.” *Materials Letters*, 203, 89–92.

Pal, A., Paul, S., Roy, A., Krishna, V., Das, M., and Sinha, A. (2017b). “Synthesis of hydroxyapatite from Lates calcarifer fishbone for biomedical applications.” *Materials Letters*, 203, 89–92.

Pallela, R., Venkatesan, J., Janapala, V. R., and Kim, S. K. (2012). “Biophysicochemical evaluation of chitosan-hydroxyapatite-marine sponge collagen composite for bone tissue engineering.” *Journal of Biomedical Materials Research - Part A*, 100 A(2), 486–495.

Parkes, M., Myant, C., Dini, D., and Cann, P. (2015). “Tribology-optimised silk protein

- hydrogels for articular cartilage repair.” *Tribology International*, 89, 9–18.
- Peng, X., He, C., Liu, J., and Wang, H. (2016). “Biomimetic jellyfish-like PVA/graphene oxide nanocomposite hydrogels with anisotropic and pH-responsive mechanical properties.” *Journal of Materials Science*, 51(12), 5901–5911.
- Periasamy, K., and Mohankumar, G. (2015). “Sea coral-derived cuttlebone reinforced epoxy composites: Characterization and tensile properties evaluation with mathematical models.” *Journal of Composite Materials*, 50(6), 807–823.
- Picone, P., Sabatino, M. A., Ajovalasit, A., Giacomazza, D., Dispenza, C., and Carlo, M. Di. (2019). “Biocompatibility, hemocompatibility and antimicrobial properties of xyloglucan-based hydrogel film for wound healing application.” *International Journal of Biological Macromolecules*, 121, 784–795.
- Prasadh, S., and Wong, R. C. W. (2018). “Unraveling the mechanical strength of biomaterials used as a bone scaffold in oral and maxillofacial defects.” *Oral Science International*, 15(2), 48–55.
- Rajakumar, G., Rahuman, A. A., Roopan, S. M., Khanna, V. G., Elango, G., Kamaraj, C., Zahir, A. A., and Velayutham, K. (2012). “Fungus-mediated biosynthesis and characterization of TiO<sub>2</sub> nanoparticles and their activity against pathogenic bacteria.” *Spectrochimica Acta - Part A: Molecular and Biomolecular Spectroscopy*, 91, 23–29.
- Riaz, M., Zia, R., Ijaz, A., Hussain, T., Mohsin, M., and Malik, A. (2018). “Synthesis of monophasic Ag-doped hydroxyapatite and evaluation of the antibacterial activity.” *Materials Science & Engineering C*, 90, 308–313.
- Roorda, W. E., H. E., Boer, A. G. de, and Junginger, H. E. (1986). “Synthetic hydrogels as drug delivery systems.” *Pharmaceutisch Weekblad Scientific Edition*, 8(3), 165–189.
- Sabu, U., Logesh, G., Rashad, M., Joy, A., and Balasubramanian, M. (2019). “Microwave-assisted synthesis of biomorphic hydroxyapatite.” *Ceramics International*, 45(6), 6718–6722.
- Sannino, A., Demitri, C., and Madaghiele, M. (2009). “Biodegradable cellulose-based hydrogels: Design and applications.” *Materials*, 2(2), 353–373.

Sridhar, B. V., Brock, J. L., Silver, J. S., Leight, J. L., Randolph, M. A., and Anseth, K. S. (2015). "Development of a cellularly degradable PEG hydrogel to promote articular cartilage extracellular matrix deposition." *Advanced Healthcare Materials*, 4(5), 702–713.

Timofejeva, A., D'Este, M., and Loca, D. (2017). "Calcium phosphate/polyvinyl alcohol composite hydrogels: A review on the freeze-thawing synthesis approach and applications in regenerative medicine." *European Polymer Journal*, 95, 547–565.

Tone, S., Hasegawa, M., Pezzotti, G., Puppulin, L., and Sudo, A. (2017). "Effect of e-beam sterilization on the in vivo performance of conventional UHMWPE tibial plates for total knee arthroplasty." *Acta Biomaterialia*, 55, 455–465.

Tyliszczak, B., Drabczyk, A., Kudłacik-Kramarczyk, S., Bialik-Was, K., Kijkowska, R., and Sobczak-Kupiec, A. (2017). "Preparation and cytotoxicity of chitosan-based hydrogels modified with silver nanoparticles." *Colloids and Surfaces B: Biointerfaces*, 160, 325–330.

Unterhofer, C., Wipplinger, C., Verius, M., Recheis, W., Thomé, C., and Ortler, M. (2017). "Reconstruction of large cranial defects with poly-methyl-methacrylate (PMMA) using a rapid prototyping model and a new technique for intraoperative implant modelling." *Neurologia i Neurochirurgia Polska*, 51(3), 214–220.

Vaandrager, J. M., Mullem, P. J. van, and Wijn, J. R. de. (1983). "Porous acrylic cement for the correction of craniofacial deformities and repair of defects, animal experimentation and two years of clinical application." *Biomaterials*, 4(2), 128–130.

Venkatesan, J., Jayakumar, R., Mohandas, A., Bhatnagar, I., and Kim, S. K. (2014). "Antimicrobial activity of chitosan-carbon nanotube hydrogels." *Materials*, 7(5), 3946–3955.

Venkatesan, J., and Kim, S.-K. (2014). "nano-hydroxyapatite composite biomaterials for bone tissue engineering--a review." *Journal of biomedical nanotechnology*, 10(10), 3124–40.

Venkatesan, J., Rekha, P. D., Anil, S., Bhatnagar, I., Sudha, P. N., Dechsakulwatana, C., Kim, S. K., and Shim, M. S. (2018). "Hydroxyapatite from Cuttlefish Bone:

Isolation, Characterizations, and Applications.” *Biotechnology and Bioprocess Engineering*, 23(4), 383–393.

Wang, J., Gong, X., Hai, J., and Li, T. (2018). “Synthesis of silver–hydroxyapatite composite with improved antibacterial properties.” *Vacuum*, 152, 132–137.

Wang, J., Zhang, F., Tsang, W. P., Wan, C., and Wu, C. (2017). “Fabrication of injectable high strength hydrogel based on 4-arm star PEG for cartilage tissue engineering.” *Biomaterials*, 120, 11–21.

Wei, Y., Chen, K., and Wu, L. (2016). “In situ synthesis of high swell ratio polyacrylic acid/silver nanocomposite hydrogels and their antimicrobial properties.” *Journal of Inorganic Biochemistry*, 164, 17–25.

Xia, X., Chen, J., Shen, J., Huang, D., Duan, P., and Zou, G. (2018). “Synthesis of hollow structural hydroxyapatite with different morphologies using calcium carbonate as a hard template.” *Advanced Powder Technology*, 29(7), 1562–1570.

Y, S. K. B., Isloor, A. M., Anil, S., and Venkatesan, J. (2019). “Calcium phosphate bioceramics with polyvinyl alcohol hydrogels for biomedical applications.” *Mater. Res. Express*, 6, 1-14.

Zaman, M., Siddique, W., Waheed, S., Sarfraz, R. M., Mahmood, A., Qureshi, J., Iqbal, J., Chughtai, F. R. S., Rahman, M. S. U., and Khalid, U. (2015). “Hydrogels, their applications and polymers used for hydrogels: A review.” *International Journal of Biology, Pharmacy and Allied Sciences (IJBPAS)*, 4(12), 6581–6603.



**NATIONAL INSTITUTE OF TECHNOLOGY KARNATAKA, SURATHKAL**

**List of Publications based on Ph.D. /M Tech (Research) Work**

SI No	Title of the paper	Authors (in the same order. Underline the Research scholar's name)	Name of the journal /conference /symposium, vol. no. pages	Month and year of publication	Category *
1	Calcium phosphate bio-ceramics with polyvinyl alcohol hydrogels for biomedical applications	<u>Santosh Kumar B.Y.</u> , Arun. M. Isloor, Sukumaran Anil, Jayachandran Venkatesan and G. C. Mohan Kumar	<i>Mater. Res. Express</i> IOP Publishing <a href="https://doi.org/10.1088/2053-1591/ab549f">https://doi.org/10.1088/2053-1591/ab549f</a>	Dec 2019	1
2	Nanohydroxyapatite Reinforced Chitosan Composite Hydrogel with Tunable Mechanical and Biological Properties for Cartilage Regeneration	<u>B. Y. Santosh Kumar.</u> , Arun M. Isloor, G. C. Mohan Kumar, Inamuddin & Abdullah M. Asiri	<i>Scientific Reports (Nature)</i> , <a href="https://doi.org/10.1038/s41598-019-52042-7">https://doi.org/10.1038/s41598-019-52042-7</a>	Dec 2019	1
3	Structure and Rheology of Chitosan-Nanohydroxyapatite Composite Hydrogel for Soft Tissue Regeneration	<u>B. Y. Santosh Kumar,</u> Arun M. Isloor., Kamalbabu Perisamy and G. C. Mohan Kumar	<i>American institute of physics (AIP)</i> <a href="https://doi.org/10.1063/5.0003867">https://doi.org/10.1063/5.0003867</a>	Feb 2020	3
4	Viscoelastic behavior of HAp reinforced polyvinyl alcohol composite hydrogel for tissue engineered articular cartilages	<u>B. Y. Santosh Kumar,</u> Arun M. Isloor. and G. C. Mohan Kumar	<i>American institute of physics (AIP)</i> <a href="https://doi.org/10.1063/1.5085633">https://doi.org/10.1063/1.5085633</a>	Mar 2019	3
5	Compressive and swelling behavior of cuttlebone derived hydroxyapatite loaded PVA hydrogel implants for articular cartilage	<u>B. Y. Santosh Kumar,</u> Arun M. Isloor. and G. C. Mohan Kumar	<i>American institute of physics (AIP)</i> <a href="https://doi.org/10.1063/1.5029655">https://doi.org/10.1063/1.5029655</a>	Apr 2018	3

\* Category: 1: Journal paper, full paper reviewed

2: Journal paper, Abstract reviewed

3: Conference/Symposium paper, full paper reviewed

4: Conference/Symposium paper, abstract reviewed

5: others (including papers in Workshops, NITK Research Bulletins, Short notes etc.)

### BIO-DATA

1. Name : Santosh Kumar B. Y.
2. Father Name : Yogendra Gowda B.P.
3. Date of Birth : 18<sup>th</sup> May 1990
4. Nationality : Indian
5. Marital Status : Single
6. Address for Communication : C/o Prof. G. C. Mohan Kumar  
Polymer Composites Laboratory  
Department of Mechanical Engineering  
National Institute of Technology Karnataka  
N.I.T.K. Surathkal, Mangaluru-575 025  
Karnataka, India
7. Permanent Address : Bilugona (V), Tenkabailu, Tenginakoppa (P)  
Thirthahalli (T), Shimogga (D)-577414  
Karnataka, India
8. Mobile Number : +91 95387-39424  
+91 94492-32366
9. E-mail Id : *santosh.ait666@gmail.com*

<b>Qualification</b>	<b>University/Board</b>	<b>Year of Passing</b>
Doctor of Philosophy, Ph.D	National Institute of Technology Karnataka, NITK	2021
Mater of Technology, M.Tech	Visvesvaraya Technological University Belagavi	2014
Bachelor of Engineering, B.E	Visvesvaraya Technological University Belagavi	2011